

POLITECNICO DI TORINO

Master's Degree in Electronic Engineering



**Politecnico
di Torino**

Master's Degree Thesis

**Sub-Terahertz Emission
in Quantum Dot Semiconductor Lasers:
a Delayed Differential Equation Approach**

Supervisors

Prof. Paolo BARDELLA

Prof. Roberto OSELLAME

Candidate

Emanuele GROPPA

October 2022

Abstract

Optical devices based on Quantum Dot (QD) structures have gained growing attention in recent years due to their expected superior properties with respect to their bulk counterparts, thus increasing the need for efficient modeling tools to analyze and predict their performances. Mode locked QD lasers are a common example of devices relying on zero-dimensional confinement with a large number of applications, ranging from the biomedical world to communication systems, with pulse repetition frequencies reaching tens or even hundreds of gigahertz. They can also be employed in the realization of compact RF signal sources generating ultra-short optical pulses at high repetition rates, providing appealing features in terms of size, power consumption and bandwidth from a sub-terahertz transmission system perspective. This represents a key research topic in Telecommunications, given the growing interest in high frequency bandwidth and 5G or 6G systems.

In this Thesis, a numerical analysis of quantum dot based edge emitting and ring lasers sources for RF applications is carried out with an efficient and reliable Multi-Section Delayed Differential Equation (MS-DDE) model. Passive and harmonic mode locking techniques can be used to generate high-quality ultra-short pulses with high repetition rates from different types of lasers, and such model allows to perform simulations of edge-emitting and ring devices by partitioning the total cavity length into slices, where a set of rate equations are solved through a DDE approach. An existing version of the MATLAB program implementing the MS-DDE model has been rewritten in order to improve its computational efficiency, with simulation times reduced of almost one order of magnitude. Most efforts have then been aimed at the identification of a working set of parameters allowing to achieve a stable harmonic mode locking regime in the sub-terahertz range, subsequently characterizing the final devices with some key performance indicators extracted from the simulations. This fulfills the initial goal of providing a practical tool for the feasibility assessment of QD based laser sources working in passive or harmonic mode locking regimes: the model can be exploited in the early stages of a design process for these types of devices, providing accurate results with a reduced time overhead when compared to other approaches that makes it suitable for extensive parametric simulations as a function of external bias and/or structural parameters.

Table of Contents

1	Introduction	1
1.1	Theoretical background	1
1.1.1	Reduced dimensionality structures in semiconductor lasers	1
1.1.2	Mode locking in semiconductor lasers	3
1.2	Aim of this Thesis	5
1.2.1	Optical generation of sub-THz signals	5
1.2.2	Simulation and DDE model	7
1.2.3	Thesis organization	8
2	Quantum Dot Lasers	9
2.1	Quantum Dot basic features	9
2.1.1	Fabrication process	9
2.1.2	Electronic structure	11
2.1.3	Broadening contributions	17
2.2	QD dynamic analysis	19
2.2.1	Density matrix formalism	19
2.2.2	Population and polarization dynamics	24
2.2.3	Rate equations under current injection	28
2.2.4	Rate equations under reverse bias voltage	35
2.2.5	Concluding remarks	37
3	Mode Locking in QD Lasers	39
3.1	General principle	39
3.1.1	ML in a Fabry-Pérot cavity	39
3.1.2	Types of mode locking	42
3.2	ML with saturable absorbers	45
3.2.1	Device configurations	46
3.2.2	Pulse amplification and shaping	47
3.2.3	SA parameters	49
3.3	ML in QD lasers	51
3.3.1	Typical characteristics	51

3.3.2	State of the art analysis	53
3.4	Light propagation in QD waveguides	66
3.4.1	Traveling wave equations	66
3.4.2	Waveguide theory and density matrix dynamics	69
3.4.3	Quantum Dot susceptibility	71
3.4.4	Spontaneous emission noise	75
3.5	MS-DDE model	76
3.5.1	Modeling mode-locked QD lasers	76
3.5.2	Multi-Section Delayed Differential Equation model description	77
3.5.3	Effects included in the model	83
4	Simulation Results	88
4.1	Unidirectional ring lasers	88
4.1.1	MS-DDE modeling of ring structures	89
4.1.2	Design and simulation of an 8-section device	90
4.1.3	Comparison with alternative structures	97
4.1.4	8-section at higher repetition rate	107
4.2	Fabry-Pérot lasers	109
4.2.1	MS-DDE modeling of edge-emitting structures	109
4.2.2	20 GHz, tapered gain section	111
4.2.3	Five-section devices	112
5	Conclusions	118
5.1	Final considerations	118
5.1.1	Main outcomes	118
5.1.2	Next steps	119
A	MATLAB Codes	120
A.1	8-section ring laser (75 GHz)	120
A.2	8-section edge-emitting laser (64 GHz)	122
	Acronyms	124
	Bibliography	126

Chapter 1

Introduction

1.1 Theoretical background

In this section, the main features on which this Thesis is centered upon are briefly outlined in order to provide a preliminary overall framework. Further details are then introduced in the following, with a more thorough analysis that allows a full description of the proposed model.

1.1.1 Reduced dimensionality structures in semiconductor lasers

The basic principle of a semiconductor laser¹, also referred to as *laser diode*, is to exploit carrier injection in a p-n junction for light generation and amplification. This idea dates back to the 1950s, while the first working prototypes (based on GaAs) have been realized in the following decade [2]. In general, three elements are required to create a laser:

- an electrical or optical **pump**, to achieve carrier inversion in the device;
- an **active material** providing the required amplification (a semiconductor in the case of laser diodes);
- a **cavity** in which the power is trapped, thus creating a resonance, while a small portion of it is extracted and fed externally.

Laser diodes show several advantages that make them more attractive with respect to other types of sources. One of the main reasons behind this success

¹Acronym for Light Amplification by Stimulated Emission of Radiation, proposed by Gordon Gould in 1959 [1].

is clearly the comparatively **low cost**, since they can be produced exploiting well-assessed semiconductor industry processes on a rather large scale. Moreover, the **net size** of these devices is in the range of square millimeters, orders of magnitude lower than solid-state or fiber-based counterparts, thus enabling a higher degree of **integration** and the possibility to implement several functions with a small footprint. Finally, laser diodes can provide better performances in terms of **reliability** and useful lifetime (hundreds of years), as well as a higher **efficiency** (around 50%) with respect to alternative solutions.

The realization of laser diodes has been relying on bulk material only, i.e. *homostructures*, until the 1980s. However, the presence of large losses with this choice represents a bottleneck for the device efficiency, also reducing the possible optimizations that can be introduced. In order to overcome these limitations, *double heterostructures* (DHS) have been introduced in semiconductor lasers thanks to the technological advancements at the end of the XX century [3]. If the heterostructure is properly designed, it allows for both **carrier and photon confinement**:

- the central portion of the device, called *active layer*, is characterized by a smaller bandgap with respect to the surrounding material, causing electrons and holes confinement thanks to the conduction band minimum E_C and valence band maximum E_V discontinuities;
- the refractive index n of the active layer is larger than that of the external regions, hence it acts as the core of a conventional waveguide providing photon confinement due to this discontinuity.

Figure 1.1 shows the basic principle of a DHS, with carriers and photon confinement along the growth direction denoted as x . Such confinement can be achieved in more than one dimension, thus leading to different types of **reduced dimensionality structures** according to the number of confined directions. Starting from the 3D bulk material, if a single dimension is confined a 2D structure is obtained, referred to as **Quantum Well** (QW). 1D structures are characterized by two confined directions (**Quantum Wires**), whereas in the case of **Quantum Dots** (QD) the material is said to be 0D due to the fact that all the three dimensions are confined. Most laser structures that are currently employed, including the ones presented in this Thesis, rely on *separate confinement heterostructures* (SCH). This represents an upgrade with respect to the DHS, since carriers are localized in the thin active layer embedded in a wider optical confinement layer.

Overall, the performances of laser diodes based on reduced dimensionality structures significantly improve with respect to their bulk counterpart. This becomes rather evident when considering the decrease of the *threshold current*, i.e. the bias current required to achieve the lasing condition. Clearly, this represents an advantage in terms of energy efficiency, since the power consumption is strongly

reduced. However, other peculiar properties of such structures can be exploited in optoelectronic applications, as presented in the following.

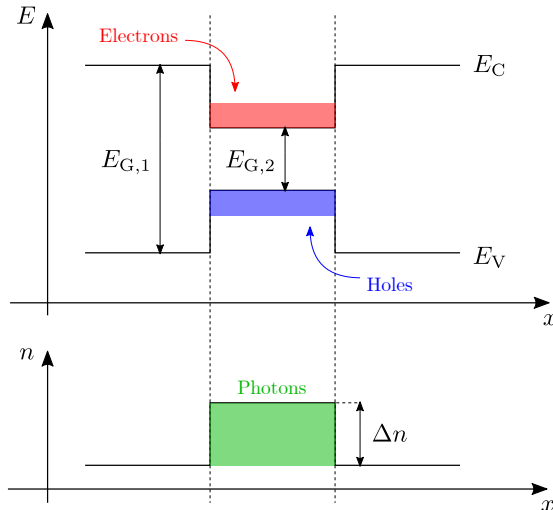


Figure 1.1: Energy (top) and refractive index (bottom) in the material growth direction of a double heterostructure.

1.1.2 Mode locking in semiconductor lasers

Mode locking (ML) is a technique that is currently employed to enable the generation of micrometer- and millimeter-wave signals in several types of lasers, chosen according to the final application. When compared to conventional solid-state lasers used for femtosecond optical pulses generation, monolithic ML semiconductor lasers offer significant improvements in terms of size, efficiency and cost.

Since a train of pulses (ideally Dirac's delta functions) in the time domain corresponds to a similar function in the frequency domain, the laser must be **multimode**: several longitudinal modes are therefore resonating in the cavity, separated in frequency by the *free spectral range* (FSR) of the device. In general, two conditions must be ensured in order to achieve mode locking.

1. The phase difference between adjacent modes must be constant in time, otherwise the output power would be almost constant and without the required pulses. The term *mode locking* actually refers to this feature, inducing the laser source to produce a train of ultra-short pulses that are phase-coherent with each other² rather than a constant wavelength output beam.

²Gain switching is another technique that allows the generation of narrow pulses, but the phase coherence is not maintained with such approach.

2. The amplitude of the cavity modes should be as constant in time as possible, so as to obtain a stable output signal.

Different types of ML are possible, with specific features and requirements that should be taken into account when designing ultra-fast pulse sources based on this technique.

- **Active:** the coupling between adjacent modes is achieved by modulating the current injection in the laser. Usually, the external signal drives an electro-optic modulator placed inside the cavity, thus causing a modulation in the net modal gain experienced by the field within the cavity. This clearly requires an external sinusoidal signal at the characteristic cavity round trip frequency.
- **Passive:** the phase locking is obtained exploiting the nonlinear absorption in a specific section, called *saturable absorber* (SA), which is biased with a constant negative voltage in monolithic semiconductor lasers. In this way, the pulses circulating inside the cavity are reshaped at each round trip when crossing the aforementioned section, due to the strong absorption that is saturated (i.e. reduced, or *bleached*) in correspondence of the central part of the pulse only.
- **Harmonic:** if the SA section is placed at the center of an edge-emitting laser cavity, the absorption can be saturated for both propagating and counter-propagating pulses, traveling in opposite directions and colliding in the absorber (colliding pulse ML). In this case, the repetition rate is twice the round trip frequency of the device. Higher repetition frequencies can be obtained by inserting in the cavity more than one SA section, also in the case of ring structures as presented in the following.
- **Hybrid:** this represents an intermediate approach, in which both negatively biased SA section and modulating input current at the fundamental repetition rate are present.

Once the longitudinal modes have been successfully locked, the required output RF signal is generated upon optical-to-electrical conversion. This can be done either by means of a high-speed photodetector or, more conveniently, directly extracting the electrical signal from the saturable absorber section of the monolithic device.

The growing interest in ML lasers based on Quantum Dot materials is due to their expected superior properties with respect to bulk 3D or 2D counterparts. However, the limited frequency tunability of such devices may pose some restrictions to their applicability. More details on mode locking in semiconductor lasers are presented in the following of this document, with a specific focus on the advantages obtained thanks to the insertion of QDs in traditional edge-emitting or ring structures.

1.2 Aim of this Thesis

Being able to achieve femtosecond optical pulses has enabled several improvements in a wide range of applications, from communication systems to sensing and real-time monitoring devices. The main purpose of this Thesis is the generation of high-frequency pulses for Telecommunications. However, the devices presented in the following may also be employed in different fields by simply tuning some of their parameters, making them suitable for other application-specific constraints.

Moreover, simulation represents a crucial step in any design activity, since it allows to evaluate and predict the performance of a device before proceeding with the actual production and characterization. This clearly reduces the expenses and the risks of such process, and the model efficiency directly affects the time required for this phase.

1.2.1 Optical generation of sub-THz signals

The realization of compact on-chip RF signal sources is a key research topic in Telecommunications, given the growing interest in high frequency bandwidth and beyond 5G applications [4]. In particular, carrier frequencies in wireless communication systems have been pushed towards higher values, with data rates that are becoming comparable with those of optical fiber-based communications. Figure 1.2 shows the historical and expected evolution of mobile systems data rate, with a steeper trend for wireless communications that are eventually expected to match wired ones at the end of this decade [5].

From this perspective, the **sub-terahertz and terahertz range** (between 90 GHz and 300 GHz) is rather attractive, since it provides a set of advantages when compared with other wireless communication links [6].

- With respect to microwave communications, THz ones intrinsically provide a sufficiently wide bandwidth for the transmission of ultra-broadband data, hence achieving an increased capacity. Moreover, THz communications are less affected by free-space diffraction phenomena, thus resulting in more directional waves.
- When compared to higher frequency bands (e.g. Infra-Red), lower atmospheric losses under poor weather conditions are ensured by THz networks. In addition to this, scintillation effects due to time-varying fluctuations in the refractive index of the atmospheric path are also reduced, allowing the realization of longer links [7].
- THz communications can also be implemented as “secure links” with protections against channel jamming attacks [8], and they represent a viable solution for first- and last-mile applications [9].

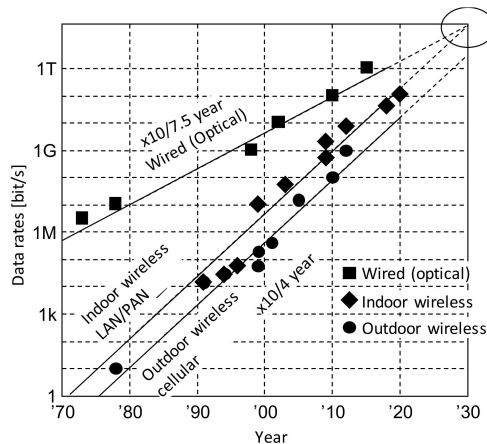


Figure 1.2: Data rate evolution in wired and wireless communication systems [5].

The generation of high-quality short pulses with high repetition rates is of paramount importance for a wide range of applications. However, developing electronic devices (e.g. mixers, amplifiers, antennae) able to work at sub-THz or even THz frequencies with reasonable costs and energy efficiency is one of the key obstacles to this innovation process. In this scenario, the optical approach represents the most immediate and straightforward solution, as well as the most convenient one. Several devices working at tens of gigahertz can already be found on the market, with low-losses and low-dispersion features that make them more attractive than conventional electronic ones [10].

Commercial systems for broadband THz generation are usually based on femtosecond pulse sources [11] and photoconductive switches [12]. However, due to their drawbacks in terms of cost, power consumption and large footprint, recently most research efforts have been shifted towards other solutions. In particular, heterodyning two optical sources with different wavelengths by means of a photomixer seems to be a more effective approach: it allows the user to obtain an output signal whose frequency is equal to the difference between the input signals frequencies, consistently with conventional RF mixers [13]. Figure 1.3 shows an example of long-range, high capacity wireless communication link at THz frequencies, with a Photonic transmitter based on optical heterodyning for the carrier generation and a more traditional electronic receiver on the other side.

Mode locking (ML) and gain switching are two techniques that can be exploited for ultra-short pulse generation [14–16], with several possible configurations that have to be properly chosen taking into account the application-specific requirements. The introduction of Quantum Dot materials to enhance their properties has been thoroughly investigated in recent years, due to the expected superior properties with respect to higher dimensionality solutions.

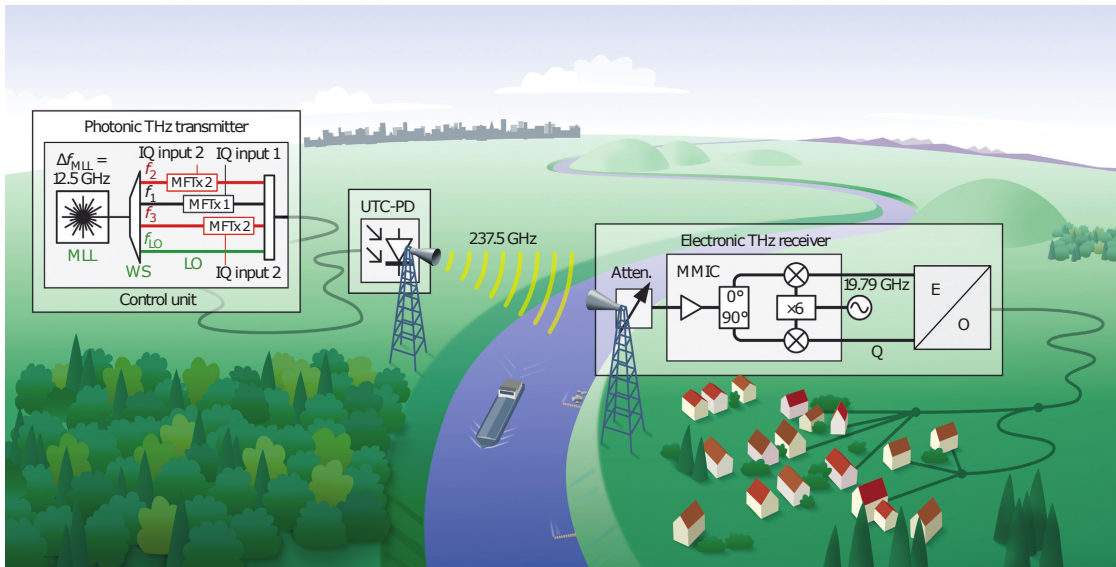


Figure 1.3: Application scenario for a wireless communication link working at THz frequencies [17].

1.2.2 Simulation and DDE model

Having a reliable numerical model for ML lasers represents a crucial element in the spread of such technology, which is not commonly available on the market yet. In particular, the parametric simulation of monolithic semiconductor lasers employed at this purpose can be considered of paramount importance not only for a deeper comprehension of the underlying physical mechanisms, but also for their practical exploitation.

In the following, a set of dynamic phenomena taking place during the pulse propagation inside the laser cavity is presented. Clearly, the time scales associated to each of these effects are rather heterogeneous, with an overall range that goes from few picoseconds (or even fractions of picoseconds) up to tens of nanoseconds. This introduces an important trade-off between **accuracy**, necessary to properly describe the semiconductor nonlinear effects on a short time scale, and **computational efficiency**, required for design and optimization when simulating long time intervals.

A first possible approach for the numerical simulation of ML lasers is the *Time-Domain Traveling-Wave* model, based on the solution of the traveling wave equations inside the cavity via a finite difference scheme [18]. With this choice, an accurate description of both the optical response of the material and the spatio-temporal evolution of the field within the cavity can be obtained. It is rather straightforward that the main drawback of such model is related to its high computational cost, becoming critical in the case of long simulated intervals.

On the other hand, a simplified description of the field dynamics in the device can be introduced in order to reduce the simulation times. In this sense, an alternative approach based on the solution of simple Delayed Differential Equations (DDE) results in reduced computational costs at the price of a lower accuracy level [19].

1.2.3 Thesis organization

In the following, monolithic lasers based on QD materials and exploited in passive or harmonic ML regime for pulse generation are considered. At first, the theoretical background required to model QD-based lasers is presented in Chapter 2, where a physical-level analysis is carried out to derive the set of rate equations at the basis of the simulations. Then, mode locking is analyzed more in depth in Chapter 3, with a specific focus on the peculiarities introduced by QD materials. A thorough state of the art analysis is presented in the same chapter, including recent achievements in terms of standalone devices, modeling techniques, and complete Telecommunications applications. In addition to this, the Multi-Section Delayed Differential Equations model is fully described. Finally, Chapter 4 includes the main results that have been obtained during this research activity, with a comparison between different types of structures in an application-oriented analysis, whereas some concluding remarks and possible future steps are reported in Chapter 5.

Chapter 2

Quantum Dot Lasers

2.1 Quantum Dot basic features

The main optical properties of Quantum Dot materials that can be exploited in lasers are presented in the following, starting from the description of energy band structure and interband transition mechanisms at the basis of their macroscopic properties. In order to understand some discrepancies with respect to the ideal case, few hints on the fabrication process are also provided, since a set of physical parameters related to this first phase can play a major role in the final behavior of the device.

2.1.1 Fabrication process

In order to achieve carrier confinement, the semiconductor material size in the confined direction should be lower than (or at most comparable to) the **de Broglie wavelength** λ_B of the considered particle. This quantity is obtained as

$$\lambda_B = \frac{h}{p} = \frac{h}{mv}, \quad (2.1)$$

where $h = 4.1357 \times 10^{-15} \text{ eV s}$ is the Planck constant, and p is the particle momentum defined as the product of its mass m and velocity v . In the case of III-V compound semiconductors, this wavelength is in the order of few tens of nanometers.

In Quantum Dots, all the three dimensions are confined, meaning that the semiconductor material has to be manufactured at the nanoscale. The realization of such structures has been enabled by relatively recent technological advancement, in particular concerning epitaxial growth techniques. III-V QDs fabrication mainly relies on **Molecular Beam Epitaxy** (MBE). This technique, which is currently

employed in deeply-scaled transistor technology too, consists of a controlled evaporation onto a target crystalline material, usually referred to as the substrate, performed in tightly constrained environmental conditions. In particular, the deposition occurs *layer by layer*: this allows an outstanding control of the process (in the nanometer or even angstrom range), clearly paid in terms of extremely low throughput and high cost.

Conventional epitaxial techniques are performed between lattice-matched materials, meaning that the lattice constant of the deposited material is equal to that of the substrate, or with a small lattice mismatch between the two components. Under specified growth conditions, though, two highly mismatched materials can be employed to achieve nanometric islands of semiconductor in a self-assembly procedure known as the **Stranski-Krastanov process** [20, 21]. As an example, InAs can be grown on a GaAs substrate with this technique, and the relative lattice mismatch between the two materials is around 7%. InAs tends to match to GaAs forming a strained layer that is referred to as **wetting layer** (WL); when the amount of deposited material exceeds a threshold value, strain relaxation leads to the formation of islands without creating dislocations. Typically, pyramidal structures are obtained with the following features [22]:

- in-plane diameter in the range (15 ÷ 30) nm;
- height equal to (3 ÷ 5) nm;
- QD surface density in the order of $(10^{10} \div 10^{11}) \text{ cm}^{-2}$.

Notice that these and other parameters strongly depend on the process conditions, such as temperature, pressure, reactant concentration and deposition rate. For instance, the diameter of InAs/InGaAs QDs increases when the growth rate is lower, or the temperature inside the reaction chamber is higher [23]. This has a direct effect on the emission wavelength of the QD, which is higher (i.e. the output frequency is lower) in the presence of larger dots.

In addition to this, the presence of a capping layer in which QD structures are embedded is commonly employed to further tune the output frequency of the device. In particular, Dots-in-a-Well (DWELL) structures present an external Quantum Well layer whose physical properties (e.g. composition, thickness) may introduce a shift in the final emission wavelength.

Figure 2.1 shows a schematic representation of a device with stacked QD layers in its active region. This stacking is introduced to increase the coupling of the active medium with the electromagnetic field, with spacing and thicknesses that can be tuned according to the specifics. The active region is then surrounded by a cladding, with wider energy gap and lower refractive index to guarantee both carrier and photon confinement. Finally, a p-doped substrate and a n-doped

contact are present, forming the conventional p-i-n junction for carrier injection in semiconductor lasers.

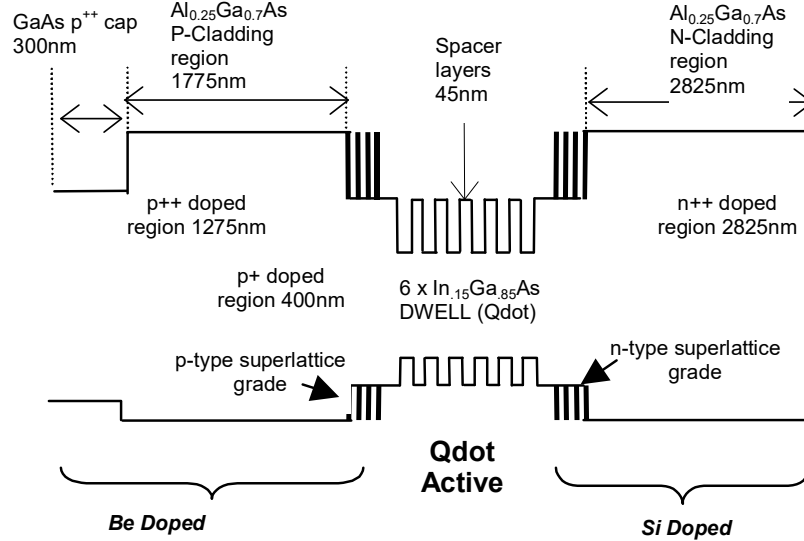


Figure 2.1: Example of heterostructure containing stacked QD layers [24].

The presence of **process variations** has to be considered carefully in the mathematical model, due to the direct effect that the aforementioned parameters have on the main properties of a QD-based device. In order to model the presence of shifts in the emission wavelength, the concept of *inhomogeneous broadening* that will be presented in the following is introduced.

2.1.2 Electronic structure

Electrons and holes in a Quantum Dot are confined in all the three dimensions, meaning that such a structure can be ideally represented as a cubic box in which carriers are trapped. From a practical point of view, this condition is achieved in the case of a semiconductor material with nanometric size along each direction in the 3D space, as mentioned previously. Carriers in a QD can occupy a discrete set of energy levels¹ due to the peculiar energy-momentum relations in the confined directions. As a consequence, the **density of states** (DOS) is not continuous as in bulk material, but **quantized**: in the ideal case, the dot energy levels are represented by Dirac's delta functions.

¹A similar behavior is experienced by electrons in an atom, hence QDs are also referred to as *artificial atoms*.

Figure 2.2 shows the first two allowed energy levels for electrons, located above the conduction band minimum E_C , namely the *ground state* (GS) E_{GS} and the first *excited state* (ES) E_{ES1} . The subscript e0 in the graph highlights that the considered case is ideal. A dual condition can be found below the valence band maximum E_V for holes: depending on whether a perfect symmetry with respect to the bandgap is assumed or not, the *excitonic* or *non-excitonic* approach is followed.

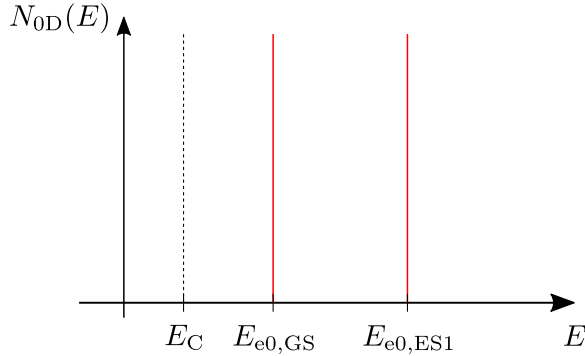


Figure 2.2: Ideal density of states for electrons confined in a Quantum Dot.

From a laser diode application perspective, some of the advantages provided by QD-based devices can already be grasped from these considerations.

- In principle, the emitted radiation should be *monochromatic*, i.e. single-frequency. This can be explained by recalling the well-known relation between photon energy and frequency

$$E_{\text{ph}} = h\nu = h \frac{c}{\lambda}, \quad (2.2)$$

where E_{ph} is the photon energy, while ν and λ are its frequency and wavelength, respectively, related by an inverse proportionality with the speed of light in vacuum $c = 2.99792458 \times 10^8$ m/s. Intuitively, a single wavelength (or frequency) corresponds to a unique energy value, hence the radiation is monochromatic if a unique level of the ideal DOS is considered.

- The number of carriers required to fill the available states is lower with respect to bulk devices, so the inversion of population condition is achieved at lower bias values, thus implying a reduced threshold current I_{th} for the device. This clearly contributes to an overall efficiency enhancement.
- The temperature sensitivity of I_{th} is lower in reduced dimensionality structures with respect to bulk counterparts, and in particular it should ideally be null when Quantum Dots are employed.

Simplified computation of the QD energy levels

Self-assembled Quantum Dots as the ones described in the previous sections are said to be *mesoscopic structures*, i.e. their size is significantly larger than the semiconductor material unit cell. In these conditions, the *effective mass approximation* can be adopted, assuming a parabolic band dispersion in the k -space to compute the eigenstates of single particles inside the QD.

Electron and hole **wavefunctions** can be written as [25]

$$\Psi_\lambda(\mathbf{k}, \mathbf{r}) = \phi_\lambda(\mathbf{r}) u_\lambda(\mathbf{k} \approx 0, \mathbf{r}), \quad \lambda = e, h. \quad (2.3)$$

- $\Psi(\mathbf{k}, \mathbf{r})$ is the particle wavefunction, expressed as a function of the wave vector \mathbf{k} and the position \mathbf{r} inside the material.
- λ is the band index, highlighting whether electrons in conduction band (CB) or holes in valence band (VB) are considered.
- $\phi(\mathbf{r})$ represents a set of *slowly-varying* envelope functions, usually consisting of quantized standing waves in the case of reduced dimensionality structures. Notice that the main assumption at the basis of the effective mass approximation is that these envelope functions do not vary much in the unit cell, characterized by sub-nanometric dimensions.
- $u(\mathbf{k} \approx 0, \mathbf{r})$ are the Bloch functions evaluated close to the considered band edge in the k space ($\mathbf{k} \approx 0$), periodic in space as the Bravais lattice.

Assuming a parabolic band dispersion, the envelope functions satisfy the effective mass equation

$$\left(-\frac{\hbar^2}{2m_\lambda^*} \nabla^2 + V_\lambda(\mathbf{r}) \right) \phi_\lambda(\mathbf{r}) = E_\lambda \phi_\lambda(\mathbf{r}), \quad (2.4)$$

where $\hbar = h/2\pi$ is the normalized Planck constant, m^* is the particle effective mass (allowing to describe it as if it were in free space), while ∇^2 is the Laplacian operator, defined as

$$\nabla^2(x, y, z) = \frac{\partial^2}{\partial x^2} + \frac{\partial^2}{\partial y^2} + \frac{\partial^2}{\partial z^2}. \quad (2.5)$$

Moreover, $V(\mathbf{r})$ is the 3D *confinement potential* for carriers in the Quantum Dot, and E represents the **eigenvalues** of this differential problem.

Determining the confinement potential in a QD is not trivial, especially when considering variations due to shape, size and strain distributions in a self-assembled structure, hence a rigorous approach would require complex numerical methods for the description of wavefunctions and energy levels. However, an analytical solution can be derived by introducing some approximations. As an example, in the case of QDs with base radius significantly larger than their height, a weak

confinement with 2D harmonic potential can be assumed in the (y, z) in-plane dimension, whereas carriers are strongly confined in the growth direction x with an infinitely high potential well [26].

It is convenient to introduce a cylindrical coordinates system, replacing the Cartesian one:

$$(x, y, z) \longrightarrow (x, r, \theta), \quad (2.6)$$

where x remains the vertical direction, r represents the radial coordinate in the former (y, z) plane, and θ is the azimuthal angle with respect to the original y axis (Figure 2.3). In this new reference system, the Laplacian operator becomes

$$\nabla^2(x, r, \theta) = \frac{\partial^2}{\partial x^2} + \frac{\partial^2}{\partial r^2} + \frac{1}{r} \frac{\partial}{\partial r} + \frac{1}{r^2} \frac{\partial^2}{\partial \theta^2}, \quad (2.7)$$

while the 3D confinement potential can be rewritten according to the aforementioned approximation as

$$V_\lambda(x, r, \theta) = V_{x,\lambda}(x) + \frac{1}{2} m_\lambda^* \omega_\lambda^2 r^2. \quad (2.8)$$

The term ω is the characteristic frequency modeling the strength of the parabolic in-plane potential, while $V_x(x)$ is the infinite potential well profile along the growth direction, defined as

$$V_x(x) = \begin{cases} 0 & x < |h_w/2| \\ \infty & x \geq |h_w/2| \end{cases}, \quad (2.9)$$

where h_w is the well width, assumed to be centered in $x = 0$. The envelope functions expression can then be factorized into transverse and in-plane components:

$$\phi_\lambda(x, r, \theta) = \xi_\lambda(x) \varphi_\lambda(r, \theta). \quad (2.10)$$

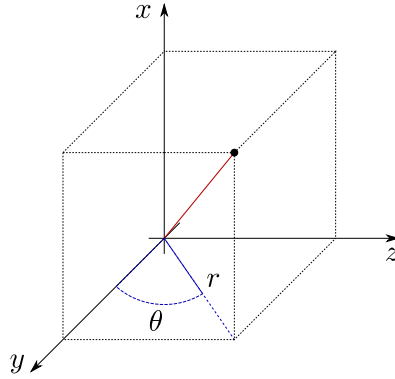


Figure 2.3: Cartesian and cylindrical coordinate systems.

Equation 2.4 can therefore be rewritten as a set of two independent equations for the transverse and in-plane wavefunctions, solved separately in the following.

- **Transverse direction.** The effective mass equation simplifies as

$$\left(-\frac{\hbar^2}{2m_\lambda^*} \frac{d^2}{dx^2} + V_{x,\lambda}(x)\right) \xi_\lambda(x) = E_{\lambda,n} \xi_\lambda(x), \quad (2.11)$$

corresponding to the 1D Schrödinger equation describing the “particle in a box” model. In the case of an infinitely high symmetric well, centered in $x = 0$ and whose width is equal to h_w , and introducing the *principal quantum number* n , the solution of this equation is simply given by

$$\xi_\lambda(x) = \sqrt{\frac{2}{h_w}} \sin\left(n \frac{\pi}{h_w} x\right), \quad (2.12)$$

with eigenvalues

$$E_{\lambda,n} = n^2 \frac{\hbar^2 \pi^2}{2m_\lambda^* h_w^2}, \quad n = 1, 2, \dots \quad (2.13)$$

Since the QD height has been assumed to be much smaller than the in-plane radius, only the fundamental transverse eigenstate (corresponding to $n = 1$) contributes effectively to the energy band structure of the dot, hence in the following higher order terms will be neglected.

- **In-plane direction.** The effective mass equation becomes

$$\left[-\frac{\hbar^2}{2m_\lambda^*} \left(\frac{\partial^2}{\partial r^2} + \frac{1}{r} \frac{\partial}{\partial r} + \frac{1}{r^2} \frac{\partial^2}{\partial \theta^2}\right) + \frac{1}{2} m_\lambda^* \omega_\lambda^2 r^2\right] \varphi_\lambda(r, \theta) = (E_\lambda - E_{\lambda,n}) \varphi_\lambda(r, \theta). \quad (2.14)$$

The solution for this equation is less immediate, given by the Fock-Darwin eigenstates, and it is not reported here for simplicity. However, the corresponding eigenvalues can be expressed in a simple form by introducing two additional integer numbers, namely the *angular momentum quantum number* $m = 0, \pm 1, \pm 2, \dots$ and the *radial quantum number* $p = 0, 1, 2, \dots$, obtaining

$$E_{\lambda,(n,p,m)} = E_{\lambda,n} + \hbar \omega_\lambda (p + |m| + 1). \quad (2.15)$$

In conclusion, considering the approximation due to strong quantization along the x axis, the eigenvalues of the complete system can be written as

$$E_{\lambda,(p,m)} = E_{\lambda,1} + \hbar \omega_\lambda (p + |m| + 1). \quad (2.16)$$

A schematic view of the obtained characteristic energy levels for electrons in CB is proposed in Figure 2.4 alongside the associated degeneracy:

- the electron ground state is characterized by quantum numbers ($p = 0, m = 0$), and it is two-fold degenerate due to spin degeneracy, not considered in the previous computations;

- the first excited state has quantum numbers $(p = 0, m = \pm 1)$, and it is therefore four-fold degenerate;
- the second excited state is instead characterized by the couples $(p = 0, m = \pm 2)$ and $(p = 1, m = 0)$, hence its degeneracy is equal to six.

$$\begin{array}{c}
 E \uparrow \\
 \vdots \\
 E_{e,ES2} = E_{e,1} + 3\hbar\omega_e \quad (0, +2) \quad (0, -2) \quad (1, 0) \\
 E_{e,ES1} = E_{e,1} + 2\hbar\omega_e \quad (0, +1) \quad (0, -1) \\
 E_{e,GS} = E_{e,1} + \hbar\omega_e \quad (0, 0)
 \end{array}$$

Figure 2.4: First three energy levels for confined electrons in the QD, with associated quantum numbers.

Clearly, this is a simplified picture that allows to describe the quantized energy levels in a QD structure as the ones reported in Figure 2.5, and it will be used in the next steps of this analysis. In more realistic scenarios, a uniform spacing between energy levels cannot be assumed, since they tend to become closer due to a weaker localization of the high-order eigenfunctions. Further increasing the energy, a transition to a continuum of the delocalized states belonging to the wetting layer occurs, up to the final 3D bulk states distribution of the SCH.

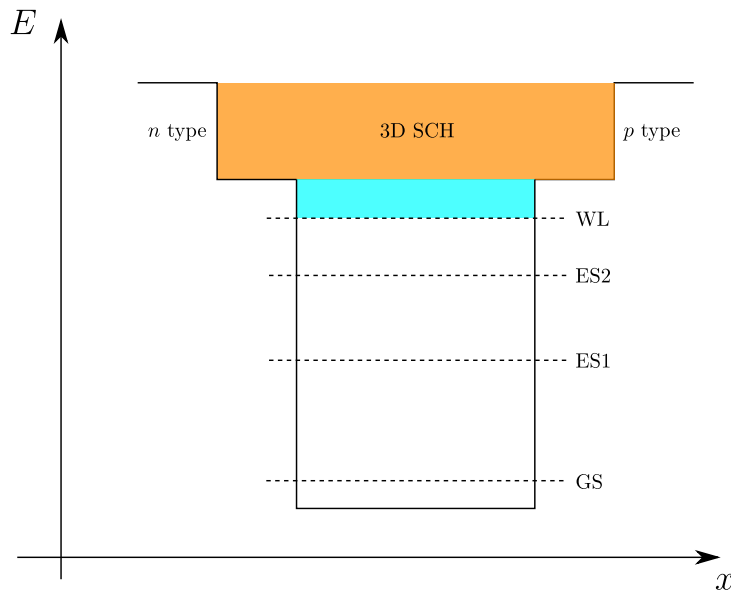


Figure 2.5: Energy levels of the whole structure.

Concerning the holes, their wavefunctions turn out to be much less confined, corresponding to a characteristic frequency $\omega_h \ll \omega_e$. The spacing between hole energy levels is therefore reduced. Moreover, light and heavy holes degeneracy should also be taken into account for a more realistic description of the QD behavior. Figure 2.6 reports two examples of energy band structures belonging to InAs/GaAs and InAs/In_{0.15}Ga_{0.85}As DWELL layers, which are in line with the proposed qualitative explanation.

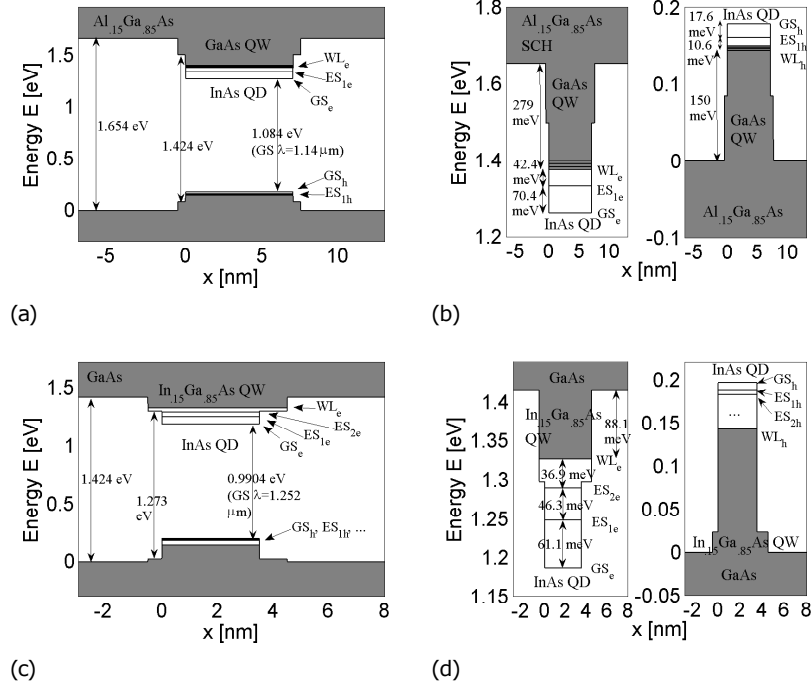


Figure 2.6: Schematics of the energy band structure for (a,b) InAs/GaAs and (c,d) InAs/In_{0.15}Ga_{0.85}As DWELL layers.

2.1.3 Broadening contributions

The fabrication of Quantum Dot structures is not ideal, with possible process variations leading to quite wide fluctuations in dimensions and shape. In practice, a Gaussian distribution describes the dot sizes obtained with the self-assembly process, but it results in a non-Gaussian distribution in the energy levels due to the strongly nonlinear dependence of the levels positions with respect to the dot size.

However, such size dependency can be assumed to be linear if the energy distribution is narrow enough, and the actual DOS is then characterized by Gaussian-like allowed states. As an example, the ground state level for an electron $E_{e,GS}$

differs from the ideal value $E_{e0,GS}$ by a quantity whose distribution function is [27]

$$D_e^{\text{inh}}(E_{e,GS}) = \frac{1}{\sqrt{\pi}\Delta E_{e,GS}^{\text{inh}}} \exp \left[- \left(\frac{E_{e,GS} - E_{e0,GS}}{\Delta E_{e,GS}^{\text{inh}}} \right)^2 \right], \quad (2.17)$$

where the electron level broadening term $\Delta E_{e,GS}^{\text{inh}}$, depending on the dot size, strain and shape, must be small for this approximation to hold, while the sample should be sufficiently large (i.e. containing a large number of dots). A similar relation holds for hole levels, hence in terms of electron-hole energy separation (e – h):

$$D_{(e-h)}^{\text{inh}}(E_{(e-h),GS}) = \frac{1}{\sqrt{\pi}\Delta E_{GS}^{\text{inh}}} \exp \left[- \left(\frac{E_{(e-h),GS} - E_{(e0-h0),GS}}{\Delta E_{GS}^{\text{inh}}} \right)^2 \right], \quad (2.18)$$

where the broadening term for transitions $\Delta E_{GS}^{\text{inh}}$ is due to both carrier types broadening contributions and equal to

$$\Delta E_{GS}^{\text{inh}} = \Delta E_{e,GS}^{\text{inh}} + \Delta E_{h,GS}^{\text{inh}}, \quad (2.19)$$

given that the two terms are narrow enough for the approximation to hold. Typical full width at half maximum (FWHM) values of this parameter for the ground state are in the range (30 ÷ 90) meV, strongly influencing the material gain.

This non-ideality, known as the **inhomogeneous broadening**, does not allow for monochromatic emission in real devices. However, it can actually be exploited in high-speed applications, such as the generation and amplification of ultra-short pulses, thanks to the advanced control in the QD growth parameters. Figure 2.7 reports an example of more realistic DOS for an electron confined in a QD considering inhomogeneous broadening: the two ideal Dirac's delta functions, centered in $E_{e0,GS}$ and $E_{e0,ES}$ respectively, are replaced by two Gaussian distributions whose queues overlap in the energy range between the two considered levels.

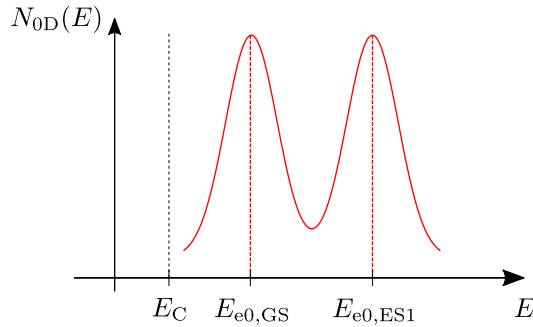


Figure 2.7: More realistic DOS for electrons in a QD.

Another effect that should be taken into account, more related to individual dots rather than their ensemble, is the **homogeneous broadening** of a radiative transition. This can be caused by the interaction of an exciton (electron-hole pair) in the dot with phonons and/or other carriers, either localized inside the QD or external to it. These events may break the quantum coherence of the electron-hole pair, leading to a Lorentzian line broadening shape in the form

$$D_{(e-h)}^{\text{hom}}(E_{\text{ph}}, E_{(e-h),\text{GS}}) = \frac{1}{\pi} \frac{\Delta E_{\text{GS}}^{\text{hom}}}{(E_{\text{ph}} - E_{(e-h),\text{GS}})^2 + (\Delta E_{\text{GS}}^{\text{hom}})^2}. \quad (2.20)$$

The term $E_{(e-h),\text{GS}}$ represents again the energy separation between electron and hole GS levels, whereas $E_{\text{ph}} = \hbar\omega$ is the photon energy. The homogeneous broadening width $\Delta E_{\text{GS}}^{\text{hom}}$ is usually more difficult to estimate experimentally than the inhomogeneous one, with typical values in the range (1 ÷ 10) meV (FWHM value, approximately 1 order of magnitude smaller with respect to the inhomogeneous width). The impact of this broadening mechanism is analyzed more in details in Section 3.5.

2.2 QD dynamic analysis

In order to model devices based on self-assembled QDs, the dynamic behavior of carriers within the confined states has to be analyzed. In particular, the time evolution of electrons and holes can be described by means of a system of *rate equations*, presented in this section. A theoretical justification of the equations describing how QD materials behave in the presence of an externally applied electromagnetic field relies on the density matrix approach, enabling the analysis of carriers and polarization evolution in these semiconductor media. Several phenomena are then introduced in the following, as well as possible approximations with respect to non-idealities that allow to achieve a more efficient computation.

2.2.1 Density matrix formalism

The optical response of a Quantum Dot to an incoming electromagnetic field can be described according to the **density matrix theory**, which allows to introduce phenomenological scattering rates describing population and polarization dynamics. This approach is typically employed in Quantum Mechanics problems in the presence of *mixed states*, providing a generalization with respect to the wavefunction approach (valid for *pure states* only) [28].

The computations presented in this Section have been carried out considering pure states only, in order to keep the notation as simple and readable as possible. However, the generalization to mixed states is immediate, as presented at the end of the discussion.

Optical dipole matrix element

The starting point of this approach is to consider a pure state, which can be described in terms of wavefunctions. In this case, the state vectors $|\lambda, \mathbf{k}\rangle$ are the eigenstates of the **unperturbed Hamiltonian** \mathbf{H}_0 , hence the stationary Schrödinger equation yields

$$\mathbf{H}_0 |\lambda, \mathbf{k}\rangle = E_{\lambda, \mathbf{k}} |\lambda, \mathbf{k}\rangle = \hbar\varepsilon_{\lambda, \mathbf{k}} |\lambda, \mathbf{k}\rangle, \quad (2.21)$$

where $E_{\lambda, \mathbf{k}} = \hbar\varepsilon_{\lambda, \mathbf{k}}$ are the associated eigenvalues. The subscript $\lambda = e, h$ is the band index identifying the type of carrier considered, while $\mathbf{k} = (p, m)$ represents the wave vector, which reduces to the in-plane quantum numbers couple within the approximation introduced to evaluate the eigenvalues. Notice that according to Dirac notation [29], the Schrödinger wavefunction $\Psi_\lambda(\mathbf{k}, \mathbf{r})$ for the state $|\lambda, \mathbf{k}\rangle$ is given by the scalar product

$$\Psi_\lambda(\mathbf{k}, \mathbf{r}) = \langle \mathbf{r} | \lambda, \mathbf{k} \rangle. \quad (2.22)$$

The state vectors obey the *completeness relation*

$$\sum_{\lambda, \mathbf{k}} |\lambda, \mathbf{k}\rangle \langle \lambda, \mathbf{k}| = 1 \quad (2.23)$$

and the *orthogonality relation*

$$\langle \lambda', \mathbf{k}' | \lambda, \mathbf{k} \rangle = \delta_{\lambda', \lambda} \delta_{\mathbf{k}', \mathbf{k}}, \quad (2.24)$$

where δ_{ij} is the Kronecker delta, defined as

$$\delta_{ij} = \begin{cases} 1 & i = j \\ 0 & i \neq j \end{cases}. \quad (2.25)$$

The unperturbed Hamiltonian can then be rewritten in its diagonal representation exploiting these two properties:

$$\mathbf{H}_0 = \sum_{\lambda', \mathbf{k}'} |\lambda', \mathbf{k}'\rangle \langle \lambda', \mathbf{k}'| \mathbf{H}_0 \sum_{\lambda, \mathbf{k}} |\lambda, \mathbf{k}\rangle \langle \lambda, \mathbf{k}| = \sum_{\lambda, \mathbf{k}} \hbar\varepsilon_{\lambda, \mathbf{k}} |\lambda, \mathbf{k}\rangle \langle \lambda, \mathbf{k}|. \quad (2.26)$$

The action of the Hamiltonian on an arbitrary wavefunction can be explained as follows: the “bra” vector $\langle \lambda, \mathbf{k}|$ projects out the part containing a state with quantum numbers λ, \mathbf{k} represented by the “ket” vector $|\lambda, \mathbf{k}\rangle$.

An externally applied time-varying electric field $\mathbf{E}(t)$ can interact with the trapped carriers in a QD structure, inducing a variation in the wavefunction. Such interaction can be described by means of the **interaction Hamiltonian** operator

$\mathbf{H}_I(t)$. Being $\mathbf{d}(\mathbf{r}) = q\mathbf{r}$ the *electric dipole moment*, this Hamiltonian can be expressed as

$$\mathbf{H}_I(t) = -\mathbf{d}(\mathbf{r}) \cdot \mathbf{E}(t) = - \left[\sum_{\lambda, \lambda', \mathbf{k}, \mathbf{k}'} \mathbf{d}_{\lambda', \lambda}(\mathbf{k}', \mathbf{k}) |\lambda', \mathbf{k}'\rangle \langle \lambda, \mathbf{k}| \right] \mathbf{E}(t). \quad (2.27)$$

The term $\mathbf{d}_{\lambda', \lambda}(\mathbf{k}', \mathbf{k})$ is the **dipole matrix element**, defined as

$$\mathbf{d}_{\lambda', \lambda}(\mathbf{k}', \mathbf{k}) = q \langle \lambda', \mathbf{k}' | \mathbf{r} | \lambda, \mathbf{k} \rangle. \quad (2.28)$$

Interband transitions and selection rules

The general relations derived before can be simplified by introducing a set of assumptions, presented in the following.

- Only interband transitions can occur, whereas intraband ones are neglected. In these conditions, the only non-null dipole matrix elements are

$$\mathbf{d}_{\lambda', \lambda}(\mathbf{k}', \mathbf{k}) \neq 0 \iff \lambda \neq \lambda', \quad (2.29)$$

and the expression to evaluate them can be written as [28]

$$\mathbf{d}_{\lambda', \lambda}(\mathbf{k}', \mathbf{k}) = q \frac{j}{m_0(\varepsilon_{\lambda, \mathbf{k}} - \varepsilon_{\lambda', \mathbf{k}'})} \langle \lambda', \mathbf{k}' | \mathbf{p} | \lambda, \mathbf{k} \rangle, \quad (2.30)$$

where $m_0 = 9.1 \times 10^{-31}$ kg is the electron rest mass and $\mathbf{p} = -j\hbar\nabla$ is the *momentum operator*.

- The left-hand side term in Equation 2.30 can be explicitated as

$$\langle \lambda', \mathbf{k}' | \mathbf{p} | \lambda, \mathbf{k} \rangle = \frac{1}{\Omega} \int_{\Omega} \Psi_{\lambda'}^*(\mathbf{k}', \mathbf{r}) \mathbf{p} \Psi_{\lambda}(\mathbf{k}, \mathbf{r}) dx dy dz, \quad (2.31)$$

exploiting the fact that the momentum operator is diagonal in the \mathbf{r} space. The integration is carried out over the lattice unit cell, identified as Ω .

- Consider again the QD wavefunctions, expressed as the product between envelope (ϕ_{λ}) and Bloch (u_{λ}) functions, presented in Equation 2.3. The former ones are said to be slowly-varying, hence they can be considered almost constant within a unit lattice cell, whereas Bloch functions have the same periodicity in space as the Bravais lattice. Consequently, the integral term in Equation 2.31 can be rewritten as

$$\begin{aligned} & \int_{\Omega} \Psi_{\lambda'}^*(\mathbf{k}', \mathbf{r}) \mathbf{p} \Psi_{\lambda}(\mathbf{k}, \mathbf{r}) dx dy dz = \\ & = -j\hbar \int_{\Omega} \phi_{\lambda'}^*(\mathbf{r}) \phi_{\lambda}(\mathbf{r}) dx dy dz \times \int_{\Omega} u_{\lambda'}^*(\mathbf{k}' \approx 0, \mathbf{r}) \nabla u_{\lambda}(\mathbf{k} \approx 0, \mathbf{r}) dx dy dz. \end{aligned} \quad (2.32)$$

The dipole matrix element relation then becomes

$$\begin{aligned} \mathbf{d}_{\lambda',\lambda}(\mathbf{k}', \mathbf{k}) &= q \frac{\hbar}{m_0(\varepsilon_{\lambda,\mathbf{k}} - \varepsilon_{\lambda',\mathbf{k}'})} \frac{1}{\Omega} \int_{\Omega} \phi_{\lambda'}^*(\mathbf{r}) \phi_{\lambda}(\mathbf{r}) dx dy dz \times \\ &\quad \times \int_{\Omega} u_{\lambda'}^*(\mathbf{k}' \approx 0, \mathbf{r}) \nabla u_{\lambda}(\mathbf{k} \approx 0, \mathbf{r}) dx dy dz. \end{aligned} \quad (2.33)$$

- Electron and hole envelope functions are characterized by the same spatial dependence, while their absolute value can be different according to the carrier confinement potential. This implies that an even or odd wavefunction in the radial direction has the same symmetry for both types of carriers: as an example, electrons and holes in the GS are characterized by in-plane quantum numbers $\mathbf{k} = (0,0)$, corresponding to an even symmetry in the x and y direction (s -type orbitals), whereas an odd symmetry (p -type) is obtained for the first ES with $\mathbf{k} = (0, \pm 1)$. Consider the first integral of Equation 2.33:
 - if the in-plane quantum numbers \mathbf{k} and \mathbf{k}' are the same, the product of the two envelope functions is even in the x and y directions, hence the integral can be significantly different from zero;
 - on the other hand, when $\mathbf{k} \neq \mathbf{k}'$ the product is an odd function along x and y , thus leading to a null 3D integral.

These considerations are known as **selection rules**, and they allow to state that the non-negligible dipole matrix elements are characterized by

$$\mathbf{d}_{\lambda',\lambda}(\mathbf{k}', \mathbf{k}) \neq 0 \iff \mathbf{k}' = \mathbf{k}. \quad (2.34)$$

Notice also that in these conditions the interaction Hamiltonian can be rewritten by performing the summation on the band indexes only (Equation 2.27), yielding

$$\begin{aligned} \mathbf{H}_I(t) &= -\mathbf{d}(\mathbf{r}) \cdot \mathbf{E}(t) = - \left[\sum_{\lambda,\lambda',\mathbf{k}} \mathbf{d}_{\lambda',\lambda}(\mathbf{k}, \mathbf{k}) |\lambda', \mathbf{k}\rangle \langle \lambda, \mathbf{k}| \right] \mathbf{E}(t) = \\ &= - \left[\sum_{\mathbf{k}} \left(\mathbf{d}_{\lambda',\lambda} |\lambda', \mathbf{k}\rangle \langle \lambda, \mathbf{k}| + \mathbf{d}_{\lambda,\lambda'}^* |\lambda, \mathbf{k}\rangle \langle \lambda', \mathbf{k}| \right) \right] \mathbf{E}(t) = \\ &= \sum_{\mathbf{k}} \mathbf{H}_{I,\mathbf{k}}(t), \end{aligned} \quad (2.35)$$

where the identity $\mathbf{d}_{\lambda',\lambda}^* = \mathbf{d}_{\lambda,\lambda'}$ has been used, and $\lambda' \neq \lambda$ according to previous considerations.

- In addition to this, the heavy hole-light hole band degeneracy is lifted in QD systems, whose hole wavefunctions are characterized by a predominant HH

behavior. While light hole Bloch functions are odd in all the space directions, HH ones are even along the growth direction x . Since electron Bloch functions are even in all the directions, and the derivative changes their symmetry to an odd one, the product inside the second integral term of Equation 2.33 is an odd function in the x direction only. Consequently, the x component of the dipole matrix element vanishes, i.e. $\mathbf{d}_{\lambda',\lambda}(\mathbf{k}, \mathbf{k}) \cdot \hat{x} = 0$, thus justifying the fact that QDs interact mainly with TE polarized fields [30, 31].

Density matrix and Liouville-Von Neumann equation

Considering the QD eigenstates $|\lambda, \mathbf{k}\rangle$ as a complete basis set, and recalling that $\mathbf{k}' = \mathbf{k}$ according to the selection rules, the single-state **density operator** for the corresponding pure state can be obtained as

$$\rho_{\mathbf{k}}(t) = \sum_{\lambda, \lambda'} \rho_{\lambda', \lambda}(\mathbf{k}, t) |\lambda', \mathbf{k}\rangle \langle \lambda, \mathbf{k}|, \quad (2.36)$$

expressing the relation between two carriers of type λ and λ' , characterized by the same in-plane quantum numbers $\mathbf{k} = (p, m)$. The complete density matrix is then obtained by simply performing a summation over all the considered states:

$$\rho(t) = \sum_{\mathbf{k}} \rho_{\mathbf{k}}(t). \quad (2.37)$$

The time evolution of the wavefunction is described by means of the time-dependent Schrödinger equation

$$j\hbar \frac{\partial}{\partial t} |\lambda, \mathbf{k}\rangle = \hat{\mathbf{H}} |\lambda, \mathbf{k}\rangle, \quad (2.38)$$

where $\hat{\mathbf{H}} = \mathbf{H}_0 + \mathbf{H}_I(t)$ is the Hamiltonian of the system. Notice that for the wavefunction complex conjugate this relation becomes

$$-j\hbar \frac{\partial}{\partial t} \langle \lambda, \mathbf{k}| = \langle \lambda, \mathbf{k}| \hat{\mathbf{H}}. \quad (2.39)$$

Thus, the time evolution of the density operator can be computed applying the derivative rules for composite functions as

$$\begin{aligned} \frac{\partial}{\partial t} \rho(t) &= \frac{\partial}{\partial t} (|\lambda, \mathbf{k}\rangle \langle \lambda, \mathbf{k}|) = \\ &= \frac{1}{j\hbar} \hat{\mathbf{H}} |\lambda, \mathbf{k}\rangle \langle \lambda, \mathbf{k}| + \frac{1}{-j\hbar} |\lambda, \mathbf{k}\rangle \langle \lambda, \mathbf{k}| \hat{\mathbf{H}} = \\ &= -\frac{j}{\hbar} \left(\hat{\mathbf{H}} |\lambda, \mathbf{k}\rangle \langle \lambda, \mathbf{k}| - |\lambda, \mathbf{k}\rangle \langle \lambda, \mathbf{k}| \hat{\mathbf{H}} \right) = \\ &= -\frac{j}{\hbar} [\hat{\mathbf{H}}, \rho(t)], \end{aligned} \quad (2.40)$$

where the double commutator property $[A, B] = AB - BA$ has been used.

Equation 2.40 can be rewritten by explicitating the Hamiltonian form for a material subject to an external electric field, and including also an additional phenomenological term describing relaxation effects due to incoherent scattering processes, for instance following electron-phonon or electron-electron interactions. In this way, the complete **Liouville-Von Neumann equation** [22, 28] is obtained:

$$\frac{\partial}{\partial t} \rho(t) = -\frac{j}{\hbar} [\mathbf{H}_0 + \mathbf{H}_I(t), \rho(t)] + \left(\frac{\partial}{\partial t} \rho(t) \right)_{\text{rel}}. \quad (2.41)$$

2.2.2 Population and polarization dynamics

The considerations carried out for the dipole matrix element should be taken into account in order to derive a set of kinetic equations for the density matrix, since they allow to identify its non-zero elements.

- The diagonal elements $\rho_{\lambda,\lambda}(\mathbf{k}, t)$ give the probability to find an electron or a hole in the state $|\lambda, \mathbf{k}\rangle$, i.e. they correspond to the population distribution in band λ . In the following, these occupation probabilities are identified as

$$\begin{cases} f_{e,\mathbf{k}}(t) = \rho_{e,e}(\mathbf{k}, t) & \lambda = e \\ f_{h,\mathbf{k}}(t) = 1 - \rho_{h,h}(\mathbf{k}, t) & \lambda = h \end{cases}. \quad (2.42)$$

- Also off-diagonal elements characterized by different band indexes but same quantum numbers, $\rho_{\lambda',\lambda}(\mathbf{k}, t)$, can be non-null. These are proportional to the microscopic interband polarization, and they will be referred to as

$$p_{\mathbf{k}}(t) = \rho_{e,h}(\mathbf{k}, t) = \rho_{h,e}^*(\mathbf{k}, t). \quad (2.43)$$

Moreover, the Hamiltonian operator is rewritten in its *interaction representation*, so the term $\mathbf{H}_{I,\mathbf{k}}(t)$ obtained in Equation 2.35 becomes

$$\begin{aligned} \mathbf{H}_{I,\mathbf{k}}^{\text{int}}(t) &= \exp\left(\frac{j}{\hbar} \mathbf{H}_0 t\right) \mathbf{H}_{I,\mathbf{k}}(t) \exp\left(-\frac{j}{\hbar} \mathbf{H}_0 t\right) = \\ &= -\left[e^{j(\varepsilon_{e,\mathbf{k}} - \varepsilon_{h,\mathbf{k}})t} \mathbf{d}_{e,h} |e, \mathbf{k}\rangle \langle h, \mathbf{k}| + e^{-j(\varepsilon_{e,\mathbf{k}} - \varepsilon_{h,\mathbf{k}})t} \mathbf{d}_{e,h}^* |h, \mathbf{k}\rangle \langle e, \mathbf{k}| \right] \mathbf{E}(t). \end{aligned} \quad (2.44)$$

Similarly, the density operator $\rho_{\mathbf{k}}(t)$ presented in Equation 2.36 is rewritten as

$$\begin{aligned} \rho_{\mathbf{k}}^{\text{int}}(t) &= \exp\left(\frac{j}{\hbar} \mathbf{H}_0 t\right) \rho_{\mathbf{k}}(t) \exp\left(-\frac{j}{\hbar} \mathbf{H}_0 t\right) = \\ &= \exp\left(\frac{j}{\hbar} \mathbf{H}_0 t\right) \left[\sum_{\lambda,\lambda'} \rho_{\lambda',\lambda}^{\text{int}}(\mathbf{k}, t) |\lambda', \mathbf{k}\rangle \langle \lambda, \mathbf{k}| \right] \exp\left(-\frac{j}{\hbar} \mathbf{H}_0 t\right). \end{aligned} \quad (2.45)$$

Coherent regime approximation

The two types of elements, diagonal and off-diagonal ones, are coupled to each other and therefore the kinetic equations describing their time evolution contain both. By neglecting at first incoherent scattering processes, the Liouville-Von Neumann equation in the interaction representation becomes

$$\begin{aligned}
 \frac{\partial}{\partial t} \rho_{\mathbf{k}}^{\text{int}}(t) &= -\frac{j}{\hbar} [\mathbf{H}_{\text{I},\mathbf{k}}(t), \rho_{\mathbf{k}}^{\text{int}}(t)] = -\frac{j}{\hbar} [\mathbf{H}_{\text{I},\mathbf{k}}(t) \rho_{\mathbf{k}}^{\text{int}}(t) - \rho_{\mathbf{k}}^{\text{int}}(t) \mathbf{H}_{\text{I},\mathbf{k}}(t)] = \\
 &= \frac{j}{\hbar} \mathbf{E}(t) \sum_{\lambda, \lambda'} \rho_{\lambda', \lambda}^{\text{int}}(\mathbf{k}, t) \times \\
 &\times \left[e^{j(\varepsilon_{e,\mathbf{k}} - \varepsilon_{h,\mathbf{k}})t} \mathbf{d}_{e,h} \left(|e, \mathbf{k}\rangle \langle h, \mathbf{k} | \lambda', \mathbf{k}\rangle \langle \lambda, \mathbf{k} | - | \lambda', \mathbf{k}\rangle \langle \lambda, \mathbf{k} | e, \mathbf{k}\rangle \langle h, \mathbf{k} | \right) + \right. \\
 &\left. + e^{-j(\varepsilon_{e,\mathbf{k}} - \varepsilon_{h,\mathbf{k}})t} \mathbf{d}_{e,h}^* \left(|h, \mathbf{k}\rangle \langle e, \mathbf{k} | \lambda', \mathbf{k}\rangle \langle \lambda, \mathbf{k} | - | \lambda', \mathbf{k}\rangle \langle \lambda, \mathbf{k} | h, \mathbf{k}\rangle \langle e, \mathbf{k} | \right) \right].
 \end{aligned} \tag{2.46}$$

This complex relation can be simplified by considering separately the diagonal and off-diagonal matrix elements.

- $\rho_{e,e}^{\text{int}}(\mathbf{k}, t)$ yields the variation of electron distribution in CB:

$$\frac{\partial}{\partial t} \rho_{e,e}^{\text{int}}(\mathbf{k}, t) = \frac{j}{\hbar} \mathbf{E}(t) \left[e^{j(\varepsilon_{e,\mathbf{k}} - \varepsilon_{h,\mathbf{k}})t} \mathbf{d}_{e,h} \rho_{h,e}^{\text{int}}(\mathbf{k}, t) - e^{-j(\varepsilon_{e,\mathbf{k}} - \varepsilon_{h,\mathbf{k}})t} \mathbf{d}_{e,h}^* \rho_{e,h}^{\text{int}}(\mathbf{k}, t) \right], \tag{2.47}$$

which adopting the new notation becomes

$$\frac{d}{dt} f_{e,\mathbf{k}}(t) = \frac{j}{\hbar} \mathbf{E}(t) \left[\mathbf{d}_{e,h}(\mathbf{k}) p_{\mathbf{k}}^*(t) - \mathbf{d}_{e,h}^*(\mathbf{k}) p_{\mathbf{k}}(t) \right]. \tag{2.48}$$

- $\rho_{h,h}^{\text{int}}(\mathbf{k}, t)$ has the same meaning for holes in VB:

$$\begin{aligned}
 \frac{\partial}{\partial t} \rho_{h,h}^{\text{int}}(\mathbf{k}, t) &= \frac{j}{\hbar} \mathbf{E}(t) \left[e^{j(\varepsilon_{h,\mathbf{k}} - \varepsilon_{e,\mathbf{k}})t} \mathbf{d}_{e,h}^* \rho_{e,h}^{\text{int}}(\mathbf{k}, t) - e^{-j(\varepsilon_{h,\mathbf{k}} - \varepsilon_{e,\mathbf{k}})t} \mathbf{d}_{e,h} \rho_{h,e}^{\text{int}}(\mathbf{k}, t) \right] = \\
 &= -\frac{\partial}{\partial t} \rho_{e,e}^{\text{int}}(\mathbf{k}, t),
 \end{aligned} \tag{2.49}$$

or equivalently

$$\begin{aligned}
 \frac{d}{dt} f_{h,\mathbf{k}}(t) &= \frac{j}{\hbar} \mathbf{E}(t) \left[\mathbf{d}_{e,h}(\mathbf{k}) p_{\mathbf{k}}^*(t) - \mathbf{d}_{e,h}^*(\mathbf{k}) p_{\mathbf{k}}(t) \right] = \\
 &= \frac{d}{dt} f_{e,\mathbf{k}}(t).
 \end{aligned} \tag{2.50}$$

- $\rho_{e,h}^{\text{int}}(\mathbf{k}, t)$ is instead associated to the interband polarization:

$$\frac{\partial}{\partial t} \rho_{e,h}^{\text{int}}(\mathbf{k}, t) = \frac{j}{\hbar} \mathbf{E}(t) \left[e^{j(\varepsilon_{h,\mathbf{k}} - \varepsilon_{e,\mathbf{k}})t} \mathbf{d}_{e,h}(\mathbf{k}) \left(\rho_{h,h}^{\text{int}}(\mathbf{k}, t) - \rho_{e,e}^{\text{int}}(\mathbf{k}, t) \right) \right], \quad (2.51)$$

which can be rewritten as

$$\frac{d}{dt} p_{\mathbf{k}}(t) = -\frac{j}{\hbar} \mathbf{E}(t) \mathbf{d}_{e,h}(\mathbf{k}) [f_{e,\mathbf{k}}(t) + f_{h,\mathbf{k}}(t) - 1]. \quad (2.52)$$

Incoherent regime and scattering rates

In real systems, the quantum coherence is lost due to dissipative and dephasing processes, occurring on a rather short time scale (in the order of femtoseconds), caused by the interaction of carriers among themselves or with phonons. The physical description of such interactions is complex and it is not analyzed in this Thesis. However, thanks to the density matrix approach, a set of phenomenological scattering rates can be inserted in the dynamic equations derived before, thus allowing to describe in a more immediate way the behavior of occupation probabilities and polarization [28].

- The CB occupation probability rate equation becomes:

$$\begin{aligned} \frac{d}{dt} f_{e,\mathbf{k}}(t) = & \frac{j}{\hbar} \mathbf{E}(t) \left[\mathbf{d}_{e,h}(\mathbf{k}) p_{\mathbf{k}}^*(t) - \mathbf{d}_{e,h}^*(\mathbf{k}) p_{\mathbf{k}}(t) \right] + \\ & + \sum_{\mathbf{k}'} \left[R_{e,\mathbf{k}' \rightarrow \mathbf{k}}(f_{e,\mathbf{k}}, f_{e,\mathbf{k}'}) - R_{e,\mathbf{k} \rightarrow \mathbf{k}'}(f_{e,\mathbf{k}}, f_{e,\mathbf{k}'}) \right] + \\ & - R_{e,\mathbf{k}}^{\text{rec}}(f_{e,\mathbf{k}}, f_{h,\mathbf{k}}). \end{aligned} \quad (2.53)$$

- The relaxation rate $R_{e,\mathbf{k}' \rightarrow \mathbf{k}}(f_{e,\mathbf{k}}, f_{e,\mathbf{k}'})$ describes intraband phenomena leading to an increment in the number of carriers in the state \mathbf{k} , hence it is characterized by a positive sign. This rate must obey Pauli exclusion principle, and it explicitly depends on the occupation probabilities of the two states involved in the transition:

$$R_{e,\mathbf{k}' \rightarrow \mathbf{k}}(f_{e,\mathbf{k}}, f_{e,\mathbf{k}'}) = \frac{f_{e,\mathbf{k}'}(t) [1 - f_{e,\mathbf{k}}(t)]}{\tau_{e,\mathbf{k}' \rightarrow \mathbf{k}}}, \quad (2.54)$$

where $\tau_{e,\mathbf{k}' \rightarrow \mathbf{k}}$ is a phenomenological time constant describing the strength of the scattering process.

- On the other hand, a negative sign is associated to any intraband process which reduces the population in the state \mathbf{k} , with electrons that are moving towards a different state \mathbf{k}' as denoted by the term $R_{e,\mathbf{k} \rightarrow \mathbf{k}'}(f_{e,\mathbf{k}}, f_{e,\mathbf{k}'})$. Also

in this case, the rate can be expressed exploiting a phenomenological time constant:

$$R_{e,\mathbf{k}\rightarrow\mathbf{k}'}(f_{e,\mathbf{k}}, f_{e,\mathbf{k}'}) = \frac{f_{e,\mathbf{k}}(t)[1 - f_{e,\mathbf{k}'}(t)]}{\tau_{e,\mathbf{k}\rightarrow\mathbf{k}'}}. \quad (2.55)$$

In the absence of external perturbations, electrons in CB tend to a quasi-equilibrium distribution (with quasi-Fermi levels for each type of carrier), and this must be ensured by imposing

$$\frac{\tau_{e,\mathbf{k}\rightarrow\mathbf{k}'}}{\tau_{e,\mathbf{k}'\rightarrow\mathbf{k}}} = \exp\left(\frac{E_{\lambda,\mathbf{k}'} - E_{\lambda,\mathbf{k}}}{k_{\text{B}}T}\right), \quad (2.56)$$

where $k_{\text{B}} = 8.617 \times 10^{-5} \text{ eV K}^{-1}$ is the Boltzmann constant and T is the absolute temperature.

- Concerning interband recombination phenomena, the rate $R_{e,\mathbf{k}}^{\text{rec}}(f_{e,\mathbf{k}}, f_{h,\mathbf{k}})$ ensures that the system is able to reach the equilibrium condition in the absence of external excitations, corresponding to a common Fermi level for electrons and holes placed within the material bandgap. Several processes can contribute to this rate, which can be evaluated as

$$R_{e,\mathbf{k}}^{\text{rec}}(f_{e,\mathbf{k}}, f_{h,\mathbf{k}}) = R_{\mathbf{k}}^{\text{sp}}(f_{e,\mathbf{k}}, f_{h,\mathbf{k}}) + R_{e,\mathbf{k}}^{\text{nr}}(f_{e,\mathbf{k}}) + R_{e,\mathbf{k}}^{\text{Aug}}(f_{e,\mathbf{k}}, f_{h,\mathbf{k}}). \quad (2.57)$$

The first contribution is related to *spontaneous emission*, involving the recombination of an electron-hole pair leading to the emission of a photon, whose rate is expressed with the time constant approach as

$$R_{\mathbf{k}}^{\text{sp}}(f_{e,\mathbf{k}}, f_{h,\mathbf{k}}) = \frac{1}{\tau_{\mathbf{k}}^{\text{sp}}} f_{e,\mathbf{k}} f_{h,\mathbf{k}}. \quad (2.58)$$

Due to the presence of traps within the material bandgap, *non-radiative recombination* processes can also occur, described by the rate

$$R_{e,\mathbf{k}}^{\text{nr}}(f_{e,\mathbf{k}}) = \frac{1}{\tau_{e,\mathbf{k}}^{\text{nr}}} f_{e,\mathbf{k}}. \quad (2.59)$$

Finally, *Auger recombination* causes the loss of an electron-hole pair while promoting another carrier to a higher energy state, thus guaranteeing the energy conservation. Several possible approaches have been proposed to model Auger processes, and the one presented in [32] has been adopted here, yielding²

$$R_{e,\mathbf{k}}^{\text{Aug}}(f_{e,\mathbf{k}}, f_{h,\mathbf{k}}) = \frac{1}{\tau_{e,\mathbf{k}}^{\text{Aug}}} \left[(f_{e,\mathbf{k}})^2 f_{h,\mathbf{k}} + \frac{1}{2} f_{e,\mathbf{k}} (f_{h,\mathbf{k}})^2 \right]. \quad (2.60)$$

²With this approach, it has been assumed that the carrier that is promoted to an excited level belongs to the same initial state \mathbf{k} , but with opposite spin.

- Concerning holes, the VB occupation probability rate equation is obtained similarly:

$$\begin{aligned} \frac{d}{dt} f_{h,\mathbf{k}}(t) = & \frac{j}{\hbar} \mathbf{E}(t) \left[\mathbf{d}_{e,h}(\mathbf{k}) p_{\mathbf{k}}^*(t) - \mathbf{d}_{e,h}^*(\mathbf{k}) p_{\mathbf{k}}(t) \right] + \\ & + \sum_{\mathbf{k}'} \left[R_{h,\mathbf{k}' \rightarrow \mathbf{k}}(f_{h,\mathbf{k}}, f_{h,\mathbf{k}'}) - R_{h,\mathbf{k} \rightarrow \mathbf{k}'}(f_{h,\mathbf{k}}, f_{h,\mathbf{k}'}) \right] + \\ & - R_{h,\mathbf{k}}^{\text{rec}}(f_{h,\mathbf{k}}, f_{h,\mathbf{k}}). \end{aligned} \quad (2.61)$$

The same considerations carried out for the CB analysis can be considered valid here, clearly using hole levels instead of electron ones. The only difference to be reported concerns the Auger recombination rate, which becomes

$$R_{h,\mathbf{k}}^{\text{Aug}}(f_{e,\mathbf{k}}, f_{h,\mathbf{k}}) = \frac{1}{\tau_{h,\mathbf{k}}^{\text{Aug}}} \left[(f_{h,\mathbf{k}})^2 f_{e,\mathbf{k}} + \frac{1}{2} f_{h,\mathbf{k}} (f_{e,\mathbf{k}})^2 \right]. \quad (2.62)$$

- The microscopic interband polarization rate equation is completed as follows:

$$\left[\frac{d}{dt} + j(\varepsilon_{e,\mathbf{k}} - \varepsilon_{h,\mathbf{k}}) + \gamma_p \right] p_{\mathbf{k}}(t) = -\frac{j}{\hbar} \mathbf{E}(t) \mathbf{d}_{e,h}(\mathbf{k}) [f_{e,\mathbf{k}}(t) + f_{h,\mathbf{k}}(t) - 1], \quad (2.63)$$

where $\varepsilon_{e,\mathbf{k}} - \varepsilon_{h,\mathbf{k}}$ is called the *frequency detuning*, expressing the frequency difference between the two bands, whereas γ_p represents an additional damping rate for the interband polarization.

The equations presented in this analysis represent the theoretical basis for a model describing the interaction between QD materials and external electromagnetic fields. In particular, light propagating along a QD-based laser diode cavity triggers the effects introduced before, which must be taken into account when characterizing such devices.

2.2.3 Rate equations under current injection

Starting from the set of equations derived in the previous steps, a complete system of rate equations governing the carrier dynamics in self-assembled QD structures under current injection can be obtained. Some assumptions are listed here, and they will be maintained in the following analysis.

- Three discrete energy levels are considered in the QD material, corresponding to the ones depicted in Figure 2.4 and Figure 2.5. As mentioned before the ground state is characterized by a degeneracy $D_{\text{GS}} = 2$, while the first and second excited states have $D_{\text{ES1}} = 4$ and $D_{\text{ES2}} = 6$, respectively. Such behavior comes from the presence of both in-plane quantum numbers and spin degeneracies.

- The index $\mathbf{k} = (p, m)$ introduced previously runs over all the possible eigenstates of the unperturbed Hamiltonian. However, it is reasonable to assume that degenerate states behave in the same way with respect to an incoming electromagnetic field, hence the population dynamics should be identical. In this way, such index will be referred to the considered QD discrete energy levels, i.e. $\mathbf{k} = (\text{GS}, \text{ES1}, \text{ES2})$.
- Carrier capture and escape processes occurring between high-energy QW states and quantized QD levels are assumed to be cascade phenomena, hence involving scattering effects among adjacent states only [33]. As an example, a direct electron capture from the wetting layer to the ground state is not possible, and it is described as a series of capture steps involving the two excited states, too.
- As stated at the end of the energy levels evaluation, 2D Quantum Well delocalized states are characterized by a transition to a continuum, which finally leads to the 3D bulk states distribution of the SCH.
- A forward bias provided by an applied current causes the injection of carriers at high energies, i.e. within the SCH barrier states. Then, a set of dissipative scattering processes allows the capture of electrons and holes into the QW wetting layer, subsequently reaching the QD states. Overall, the system is out of equilibrium, but in order to simplify the model SCH and WL are assumed to remain in a quasi-equilibrium condition, meaning that carriers in CB and VB are characterized by two distributions with quasi-Fermi levels: consequently, the occupation probabilities for SCH and WL are considered almost null in the following. Such assumption is valid if scattering processes leading these two subsystems to a Fermi distribution occur in a rather short time scale, in the order of few tens of fs [34].
- The total number of carriers per unit length in the considered state is denoted as $n_{\lambda, \mathbf{k}}$, where electrons and holes are identified by means of the usual band index $\lambda = e, h$. Notice that this quantity is related to the occupation probabilities introduced in the previous computations as

$$n_{\lambda, \mathbf{k}}(z, t) = W N_1 N_D D_{\mathbf{k}} \bar{f}_{\lambda, \mathbf{k}}(z, t), \quad (2.64)$$

where z is the electromagnetic wave propagation direction, W is the device width, N_1 and N_D are the number of stacked DWELL layers and the QD surface density in each of them, $D_{\mathbf{k}}$ is the state degeneracy and $\bar{f}_{\lambda, \mathbf{k}}$ represents the occupation probability averaged over the transverse directions of the device.

The dynamic behavior is presented separately for each allowed energy state, in order to construct the set of differential equations describing the device response

for both types of carriers. This is initially carried out in **forward bias conditions**, meaning that current injection is considered while no bias voltage is applied. The overall behavior of the material is reported in Figure 2.8, where only electron levels in CB are represented.

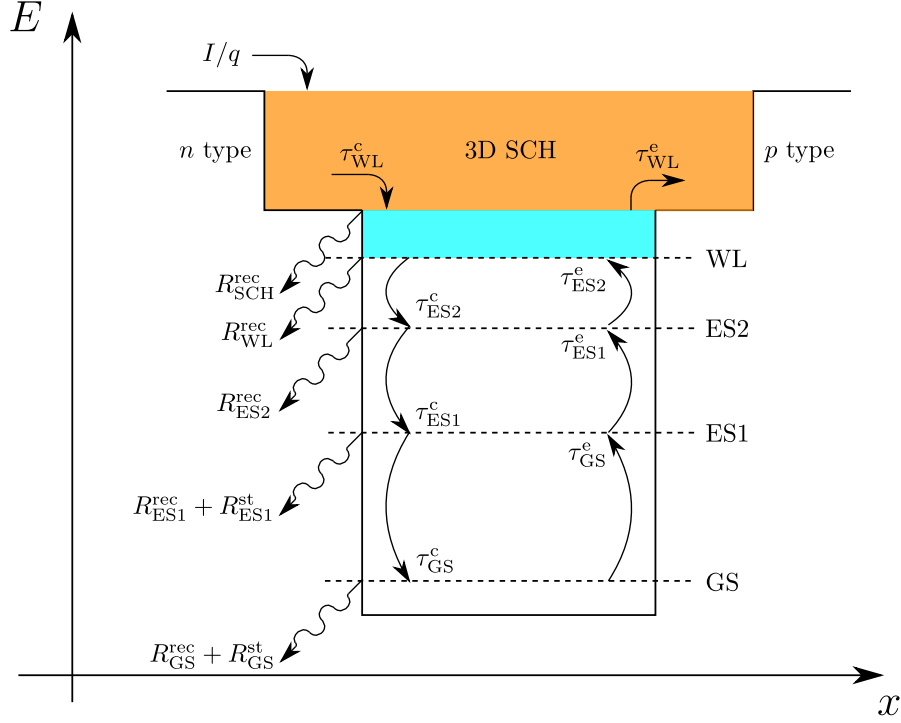


Figure 2.8: Electrons transitions between allowed states in conduction band, under forward bias conditions.

Separate Confinement Heterostructure

The SCH carriers evolution in time is described by the rate equations

$$\begin{aligned} \frac{\partial}{\partial t} n_{\lambda, \text{SCH}} = & \eta_i \frac{J}{q} W + \frac{n_{\lambda, \text{WL}}}{\tau_{\lambda, \text{WL} \rightarrow \text{SCH}}} - \frac{n_{\lambda, \text{SCH}}}{\tau_{\lambda, \text{SCH} \rightarrow \text{WL}}} + \\ & - \frac{B_{\text{SCH}}}{W h_{\text{SCH}}} n_{\lambda, \text{SCH}} n_{\lambda', \text{SCH}} - \frac{n_{\lambda, \text{SCH}}}{\tau_{\lambda, \text{SCH}}^{\text{nr}}}. \end{aligned} \quad (2.65)$$

- Carriers are pumped into the SCH by means of the externally applied bias current $I = JW$, similarly to any semiconductor laser. The internal quantum efficiency η_i determines the percentage of current which is effectively transformed into carriers.

- The escape rate $R_{\lambda, \text{QW} \rightarrow \text{SCH}}$ from the QW wetting layer towards the SCH states is proportional to the number of carriers available in the initial state, and its strength is evaluated through the time constant $\tau_{\lambda, \text{QW} \rightarrow \text{SCH}} = \tau_{\lambda, \text{QW} \rightarrow \text{SCH}}^e$. The sign of this rate is positive, since it tends to increment the number of carriers in the considered state.
- The opposite process, corresponding to the capture rate $R_{\lambda, \text{SCH} \rightarrow \text{QW}}$, is characterized by a negative sign due to the fact that carriers are leaving the SCH states to move towards the WL ones. Notice that in this case an additional time constant related to carrier diffusion in the SCH region should be included, thus obtaining $\tau_{\lambda, \text{SCH} \rightarrow \text{QW}} = \tau_{\lambda, \text{SCH} \rightarrow \text{QW}}^c + \tau_{\lambda, \text{SCH} \rightarrow \text{QW}}^{\text{dif}}$. This characteristic time can be computed as [35]

$$\tau_{\lambda, \text{SCH} \rightarrow \text{QW}}^{\text{dif}} = \frac{L_{\text{dif}}^2}{2D_{\lambda}} = \left(\frac{h_{\text{SCH}}}{2} \right)^2 \frac{q}{2\mu_{\lambda} k_{\text{B}} T}, \quad (2.66)$$

where L_{dif} is the diffusion length, assumed to be equal to half the barrier height h_{SCH} , while the carrier diffusion coefficient D_{λ} is evaluated by means of Einstein relations from the mobility μ_{λ} and the voltage equivalent of temperature $k_{\text{B}} T/q$.

- The characteristic time constants must satisfy the balance condition presented in Equation 2.56, hence it must be

$$\frac{\tau_{\lambda, \text{WL} \rightarrow \text{SCH}}}{\tau_{\lambda, \text{SCH} \rightarrow \text{WL}}} = \frac{D_{\text{WL}}}{D_{\text{SCH}}} \exp\left(\frac{E_{\lambda, \text{SCH}} - E_{\lambda, \text{WL}}}{K_{\text{B}} T}\right), \quad (2.67)$$

where the effective densities of states for SCH and WL can be evaluated as [27]

$$D_{\text{SCH}} = \frac{2}{h_{\text{SCH}}} \frac{2\pi m_{\lambda, \text{SCH}}^* k_{\text{B}} T}{\hbar^2}, \quad D_{\text{WL}} = \frac{N_1}{h_{\text{WL}}} \frac{m_{\lambda, \text{WL}}^* k_{\text{B}} T}{\pi \hbar^2}. \quad (2.68)$$

- Among the interband processes, the spontaneous emission contribution is taken into account in the SCH rate equation. The coefficient B_{SCH} , normalized by the barrier area, expresses the recombination process strength between electrons and holes belonging to the SCH. Spontaneous emission is a second-order phenomenon ($R_{\mathbf{k}}^{\text{sp}} \propto n_{\mathbf{k}}^2$), as highlighted by the product between two different populations.
- Finally, non-radiative recombination is also considered and modeled through the characteristic time constant $\tau_{\lambda, \text{SCH}}^{\text{nr}}$, whereas Auger recombination is neglected in this state.

Wetting layer.

Concerning the Quantum Well WL, the carrier rate equations yield

$$\begin{aligned} \frac{\partial}{\partial t} n_{\lambda, \text{WL}} = & \frac{n_{\lambda, \text{SCH}}}{\tau_{\lambda, \text{SCH} \rightarrow \text{WL}}} - \frac{n_{\lambda, \text{WL}}}{\tau_{\lambda, \text{WL} \rightarrow \text{SCH}}} + \frac{n_{\lambda, \text{ES2}}}{\tau_{\lambda, \text{ES2} \rightarrow \text{WL}}} - \frac{n_{\lambda, \text{WL}}(1 - \bar{f}_{\lambda, \text{ES2}})}{\tau_{\lambda, \text{WL} \rightarrow \text{ES2}}} + \\ & - \frac{B_{\text{WL}}}{Wh_{\text{WL}}} n_{\lambda, \text{WL}} n_{\lambda', \text{WL}} - \frac{n_{\lambda, \text{WL}}}{\tau_{\lambda, \text{WL}}^{\text{nr}}}. \end{aligned} \quad (2.69)$$

- The same escape and capture rates introduced in the case of the SCH are present in this relation, clearly with an opposite sign related to the reversed transition direction.
- Similarly, a couple of scattering processes from (escape) and towards (capture) the second excited state is introduced. Notice that no occupation probability for the WL is present concerning the escape mechanism, which depends only on the ES2 population $n_{\lambda, \text{ES2}}$ and on the characteristic time constant $\tau_{\lambda, \text{ES2} \rightarrow \text{WL}}$, due to the assumption of quasi-equilibrium in the well states. On the other hand, in order for a carrier to be captured into the ES2 level, this must not be completely filled, hence the additional factor $(1 - \bar{f}_{\lambda, \text{ES2}})$ is introduced. In this case the balance condition yields

$$\frac{\tau_{\lambda, \text{ES2} \rightarrow \text{WL}}}{\tau_{\lambda, \text{WL} \rightarrow \text{ES2}}} = \frac{D_{\text{ES2}} N_{\text{D}}}{D_{\text{WL}}} \exp\left(\frac{E_{\lambda, \text{WL}} - E_{\lambda, \text{ES2}}}{K_{\text{B}} T}\right), \quad (2.70)$$

where the effective density of states for the second excited state is substituted by its degeneracy, multiplied by the dot surface density N_{D} .

- As in the previous case, spontaneous emission (with strength B_{WL}) and non-radiative (time constant $\tau_{\lambda, \text{WL}}^{\text{nr}}$) recombination processes are considered as the only interband phenomena, whereas Auger recombination is neglected.

Second excited state.

The highest QD level considered in this analysis is the second excited state, characterized by population rate equations yielding

$$\begin{aligned} \frac{\partial}{\partial t} n_{\lambda, \text{ES2}} = & \frac{n_{\lambda, \text{WL}}(1 - \bar{f}_{\lambda, \text{ES2}})}{\tau_{\lambda, \text{WL} \rightarrow \text{ES2}}} - \frac{n_{\lambda, \text{ES2}}}{\tau_{\lambda, \text{ES2} \rightarrow \text{WL}}} + \\ & + \frac{n_{\lambda, \text{ES1}}(1 - \bar{f}_{\lambda, \text{ES2}})}{\tau_{\lambda, \text{ES1} \rightarrow \text{ES2}}} - \frac{n_{\lambda, \text{ES2}}(1 - \bar{f}_{\lambda, \text{ES1}})}{\tau_{\lambda, \text{ES2} \rightarrow \text{ES1}}} + \\ & - \frac{n_{\lambda, \text{ES2}} \bar{f}_{\lambda', \text{ES2}}}{\tau_{\text{ES2}}^{\text{sp}}} - \frac{n_{\lambda, \text{ES2}}}{\tau_{\lambda, \text{ES2}}^{\text{nr}}} - \frac{\bar{f}_{\lambda, \text{ES2}} \bar{f}_{\lambda', \text{ES2}} (n_{\lambda, \text{ES2}} + n_{\lambda', \text{ES2}}/2)}{\tau_{\lambda, \text{ES2}}^{\text{Aug}}} - R_{\text{ES2}}^{\text{st}}. \end{aligned} \quad (2.71)$$

- Capture and escape rates between ES2 and WL are the same presented before, with opposite sign.
- The scattering phenomena causing carriers to move towards (escape, positive sign) or from (capture, negative sign) ES2 from/towards the lower excited state depend on the two population densities and on the occupation probabilities of these two states. Moreover, they satisfy the balance relation

$$\frac{\tau_{\lambda,ES1 \rightarrow ES2}}{\tau_{\lambda,ES2 \rightarrow ES1}} = \frac{D_{ES1}}{D_{ES2}} \exp\left(\frac{E_{\lambda,ES2} - E_{\lambda,ES1}}{K_B T}\right), \quad (2.72)$$

where the two degeneracies have been used as effective densities of states for the considered energy levels.

- Among the interband processes, spontaneous emission (second order, time constant τ_{ES2}^{sp}), non-radiative scattering phenomena (first order, with characteristic time $\tau_{\lambda,ES2}^{nr}$), and Auger recombination (third order, phenomenological time constant $\tau_{\lambda,ES2}^{Aug}$) have been introduced in these rate equations.
- Furthermore, an additional term has been added to include the possibility of having *stimulated emission* recombination in ES2. From a carrier rate perspective, this phenomenon is apparently the same as spontaneous emission, but it actually occurs in the presence of an electromagnetic radiation: photons that are emitted thanks to electron-hole pairs recombination in these conditions are said to be *coherent*, i.e. they are characterized by the same wavelength (or frequency) as the impinging wave. The value of $R_{\mathbf{k}}^{st}$ can be computed by considering additional elements related to the waveguide structure, as will be presented in Chapter 3.

First excited state.

The rate equations for ES1 yield

$$\begin{aligned} \frac{\partial}{\partial t} n_{\lambda,ES1} = & \frac{n_{\lambda,ES2}(1 - \bar{f}_{\lambda,ES1})}{\tau_{\lambda,ES2 \rightarrow ES1}} - \frac{n_{\lambda,ES1}(1 - \bar{f}_{\lambda,ES2})}{\tau_{\lambda,ES1 \rightarrow ES2}} + \\ & + \frac{n_{\lambda,GS}(1 - \bar{f}_{\lambda,ES1})}{\tau_{\lambda,GS \rightarrow ES1}} - \frac{n_{\lambda,ES1}(1 - \bar{f}_{\lambda,GS})}{\tau_{\lambda,ES1 \rightarrow GS}} + \\ & - \frac{n_{\lambda,ES1} \bar{f}_{\lambda',ES1}}{\tau_{ES1}^{sp}} - \frac{n_{\lambda,ES1}}{\tau_{\lambda,ES1}^{nr}} - \frac{\bar{f}_{\lambda,ES1} \bar{f}_{\lambda',ES1} (n_{\lambda,ES1} + n_{\lambda',ES1}/2)}{\tau_{\lambda,ES1}^{Aug}} - R_{ES1}^{st}. \end{aligned} \quad (2.73)$$

The same considerations as before can be carried out concerning both intraband and interband processes. Transitions between ES1 and GS obey the balance relation

$$\frac{\tau_{\lambda,GS \rightarrow ES1}}{\tau_{\lambda,ES1 \rightarrow GS}} = \frac{D_{GS}}{D_{ES1}} \exp\left(\frac{E_{\lambda,ES1} - E_{\lambda,GS}}{K_B T}\right). \quad (2.74)$$

Ground state.

Finally, the populations in the ground state evolve as

$$\begin{aligned} \frac{\partial}{\partial t} n_{\lambda, \text{GS}} = & \frac{n_{\lambda, \text{ES1}} (1 - \bar{f}_{\lambda, \text{GS}})}{\tau_{\lambda, \text{ES1} \rightarrow \text{GS}}} - \frac{n_{\lambda, \text{GS}} (1 - \bar{f}_{\lambda, \text{ES1}})}{\tau_{\lambda, \text{GS} \rightarrow \text{ES1}}} + \\ & - \frac{n_{\lambda, \text{GS}} \bar{f}_{\lambda', \text{GS}}}{\tau_{\text{GS}}^{\text{sp}}} - \frac{n_{\lambda, \text{GS}}}{\tau_{\lambda, \text{GS}}^{\text{nr}}} - \frac{\bar{f}_{\lambda, \text{GS}} \bar{f}_{\lambda', \text{GS}} (n_{\lambda, \text{GS}} + n_{\lambda', \text{GS}}/2)}{\tau_{\lambda, \text{GS}}^{\text{Aug}}} - R_{\text{GS}}^{\text{st}}. \end{aligned} \quad (2.75)$$

GS is the lowest QD energy level, hence no transition to and from states below it is possible.

Excitonic model

When charge neutrality is assumed for each state of the structure, the rate equations describing the dynamic behavior of the device are significantly simplified. In particular, this widespread approach is known as the *excitonic*³ approximation [36], and it implies that electron and hole dynamics must be coincident to ensure neutrality.

The complete correlation between CB and VB populations allows to state that:

$$\begin{cases} n_{e, \mathbf{k}} = n_{h, \mathbf{k}} = n_{\mathbf{k}} \\ \bar{f}_{e, \mathbf{k}} = \bar{f}_{h, \mathbf{k}} = \bar{f}_{\mathbf{k}} \\ \tau_{e, \mathbf{k} \leftrightarrow \mathbf{k}'} = \tau_{h, \mathbf{k} \leftrightarrow \mathbf{k}'} = \tau_{\mathbf{k} \leftrightarrow \mathbf{k}'} \end{cases} . \quad (2.76)$$

According to these simplifications, rate equations for one population only can be solved, and they can be rewritten as follows.

- Separate Confinement Heterostructure:

$$\begin{aligned} \frac{\partial}{\partial t} n_{\text{SCH}} = & \eta_i \frac{J}{q} W + \frac{n_{\text{WL}}}{\tau_{\text{WL} \rightarrow \text{SCH}}} - \frac{n_{\text{SCH}}}{\tau_{\text{SCH} \rightarrow \text{WL}}} + \\ & - \frac{B_{\text{SCH}}}{W h_{\text{SCH}}} n_{\text{SCH}}^2 - \frac{n_{\text{SCH}}}{\tau_{\text{SCH}}^{\text{nr}}}. \end{aligned} \quad (2.77)$$

- Wetting layer:

$$\begin{aligned} \frac{\partial}{\partial t} n_{\text{WL}} = & \frac{n_{\text{SCH}}}{\tau_{\text{SCH} \rightarrow \text{WL}}} - \frac{n_{\text{WL}}}{\tau_{\text{WL} \rightarrow \text{SCH}}} + \frac{n_{\text{ES2}}}{\tau_{\text{ES2} \rightarrow \text{WL}}} - \frac{n_{\text{WL}} (1 - \bar{f}_{\text{ES2}})}{\tau_{\text{WL} \rightarrow \text{ES2}}} + \\ & - \frac{B_{\text{WL}}}{W h_{\text{WL}}} n_{\text{WL}}^2 - \frac{n_{\text{WL}}}{\tau_{\text{WL}}^{\text{nr}}}. \end{aligned} \quad (2.78)$$

³An exciton is a weakly-bounded electron-hole pair, hence the name of this approximation refers to the fact that the two types of carriers are considered to evolve in the same way.

- Second excited state:

$$\begin{aligned}
 \frac{\partial}{\partial t} n_{\text{ES2}} = & \frac{n_{\text{WL}}(1 - \bar{f}_{\text{ES2}})}{\tau_{\text{WL} \rightarrow \text{ES2}}} - \frac{n_{\text{ES2}}}{\tau_{\text{ES2} \rightarrow \text{WL}}} + \\
 & + \frac{n_{\text{ES1}}(1 - \bar{f}_{\text{ES2}})}{\tau_{\text{ES1} \rightarrow \text{ES2}}} - \frac{n_{\text{ES2}}(1 - \bar{f}_{\text{ES1}})}{\tau_{\text{ES2} \rightarrow \text{ES1}}} + \\
 & - \frac{n_{\text{ES2}} \bar{f}_{\text{ES2}}}{\tau_{\text{ES2}}^{\text{sp}}} - \frac{n_{\text{ES2}}}{\tau_{\text{ES2}}^{\text{nr}}} - \frac{n_{\text{ES2}} \bar{f}_{\text{ES2}}^2}{\tau_{\text{ES2}}^{\text{Aug}}} - R_{\text{ES2}}^{\text{st}}.
 \end{aligned} \tag{2.79}$$

- First excited state:

$$\begin{aligned}
 \frac{\partial}{\partial t} n_{\text{ES1}} = & \frac{n_{\text{ES2}}(1 - \bar{f}_{\text{ES1}})}{\tau_{\text{ES2} \rightarrow \text{ES1}}} - \frac{n_{\text{ES1}}(1 - \bar{f}_{\text{ES2}})}{\tau_{\text{ES1} \rightarrow \text{ES2}}} + \\
 & + \frac{n_{\text{GS}}(1 - \bar{f}_{\text{ES1}})}{\tau_{\text{GS} \rightarrow \text{ES1}}} - \frac{n_{\text{ES1}}(1 - \bar{f}_{\text{GS}})}{\tau_{\text{ES1} \rightarrow \text{GS}}} + \\
 & - \frac{n_{\text{ES1}} \bar{f}_{\text{ES1}}}{\tau_{\text{ES1}}^{\text{sp}}} - \frac{n_{\text{ES1}}}{\tau_{\text{ES1}}^{\text{nr}}} - \frac{n_{\text{ES1}} \bar{f}_{\text{ES1}}^2}{\tau_{\text{ES1}}^{\text{Aug}}} - R_{\text{ES1}}^{\text{st}}.
 \end{aligned} \tag{2.80}$$

- Ground state:

$$\begin{aligned}
 \frac{\partial}{\partial t} n_{\text{GS}} = & \frac{n_{\text{ES1}}(1 - \bar{f}_{\text{GS}})}{\tau_{\text{ES1} \rightarrow \text{GS}}} - \frac{n_{\text{GS}}(1 - \bar{f}_{\text{ES1}})}{\tau_{\text{GS} \rightarrow \text{ES1}}} + \\
 & - \frac{n_{\text{GS}} \bar{f}_{\text{GS}}}{\tau_{\text{GS}}^{\text{sp}}} - \frac{n_{\text{GS}}}{\tau_{\text{GS}}^{\text{nr}}} - \frac{n_{\text{GS}} \bar{f}_{\text{GS}}^2}{\tau_{\text{GS}}^{\text{Aug}}} - R_{\text{GS}}^{\text{st}}.
 \end{aligned} \tag{2.81}$$

2.2.4 Rate equations under reverse bias voltage

Passively mode-locked lasers are characterized by the presence of a reversely biased region (see Chapter 3), hence the QD material behavior in the presence of an external static electric field perpendicular to the stacked layers (i.e. in the x direction) should also be analyzed. The total electric field is given by

$$F_x = \frac{V + V_{\text{bi}}}{h_{\text{SCH}}}, \tag{2.82}$$

where V is the applied voltage and V_{bi} is the built-in potential of the junction.

An applied electric field modifies the QD wavefunctions due to its effect on the 3D confinement potential: this is known as *Quantum-Confined Stark Effect* (QCSE), initially found in QWs and subsequently reported in Quantum Dot systems too [37, 38]. As a consequence, a downwards shift in the characteristic electron and

hole energy levels has been reported, thus leading to smaller interband transition energies for the QD states and therefore inducing a shift of the absorption spectrum towards lower frequencies [39]. However, such effect turned out to be negligible in QD structures, hence it will not be included in the model.

On the other hand, the effect of an externally applied static electric field on intraband carrier dynamics is relevant in this discussion. The band structure is “tilted” in the presence of such field along the growth direction, and tunneling processes towards SCH from lower energy levels are also possible [40]. Figure 2.9 shows the usual band structure of the device, modified due to the presence of an external electric field in the x direction. In order to introduce an additional term for the tunneling escape rates from QD and WL levels towards the SCH, the Wentzel-Kremer-Brillouin approximation for a triangular well can be used [40, 41]:

$$R_{\lambda,\text{WL}}^{\text{tun}} = \frac{\hbar\pi}{2m_{\lambda,\text{WL}}^* h_{\text{WL}}^2} \exp\left(-\frac{4}{3} \frac{\sqrt{2m_{\lambda,\text{SCH}}^*} (E_{\lambda,\text{SCH}} - E_{\lambda,\text{WL}})^{3/2}}{q\hbar F_x}\right) n_{\lambda,\text{WL}}, \quad (2.83)$$

$$R_{\lambda,\mathbf{k}}^{\text{tun}} = \frac{\hbar\pi}{2m_{\lambda,\mathbf{k}}^* h_{\text{QD}}^2} \exp\left(-\frac{4}{3} \frac{\sqrt{2m_{\lambda,\text{SCH}}^*} (E_{\lambda,\text{SCH}} - E_{\lambda,\mathbf{k}})^{3/2}}{q\hbar F_x}\right) n_{\lambda,\mathbf{k}}, \quad (2.84)$$

Furthermore, due to a reduction in the confinement potential barrier, thermionic escape mechanisms from QW and QD (only ES2) states are enhanced. The induced reduction is linear, and the escape characteristic times of these levels are modified by introducing a field-dependent component:

$$\tau_{\lambda,\text{WL}\rightarrow\text{SCH}}(F_x) = \tau_{\lambda,\text{WL}\rightarrow\text{SCH}}(0) \exp\left(\frac{qF_x h_{\text{WL}}}{k_{\text{B}}T}\right), \quad (2.85)$$

$$\tau_{\lambda,\text{ES2}\rightarrow\text{WL}}(F_x) = \tau_{\lambda,\text{ES2}\rightarrow\text{WL}}(0) \exp\left(\frac{qF_x h_{\text{QD}}}{k_{\text{B}}T}\right), \quad (2.86)$$

where $\tau_{\lambda,\text{WL}\rightarrow\text{SCH}}(0)$ and $\tau_{\lambda,\text{ES2}\rightarrow\text{WL}}(0)$ are the characteristic time constants evaluated in the absence of an applied electric field, i.e. with $F_x = 0$.

Finally, carriers in the SCH region are accelerated by the static electric field, creating a drift current which reduces the population in this state. Such term can be expressed as

$$I_{\lambda,\text{SCH}}^{\text{drift}}(F_x) = \mu_{\lambda,\text{SCH}} F_x n_{\lambda,\text{SCH}}. \quad (2.87)$$

In conclusion, the SCH rate equation in the presence of a reverse bias voltage becomes

$$\begin{aligned} \frac{\partial}{\partial t} n_{\lambda,\text{SCH}} = & -\mu_{\lambda,\text{SCH}} F_x n_{\lambda,\text{SCH}} + \frac{n_{\lambda,\text{WL}}}{\tau_{\lambda,\text{WL}\rightarrow\text{SCH}}(F_x)} - \frac{n_{\lambda,\text{SCH}}}{\tau_{\lambda,\text{SCH}\rightarrow\text{WL}}} + \\ & - \frac{B_{\text{SCH}}}{Wh_{\text{SCH}}} n_{\lambda,\text{SCH}} n_{\lambda',\text{SCH}} - \frac{n_{\lambda,\text{SCH}}}{\tau_{\lambda,\text{SCH}}^{\text{nr}}} + R_{\lambda,\text{WL}}^{\text{tun}} + \sum_{\mathbf{k}} R_{\lambda,\mathbf{k}}^{\text{tun}}. \end{aligned} \quad (2.88)$$

The rate equations for WL and QD energy levels are not reported here, since they are simply modified by including the corresponding tunneling rate $R_{\lambda,\mathbf{k}}^{\text{tun}}$ with a negative sign.

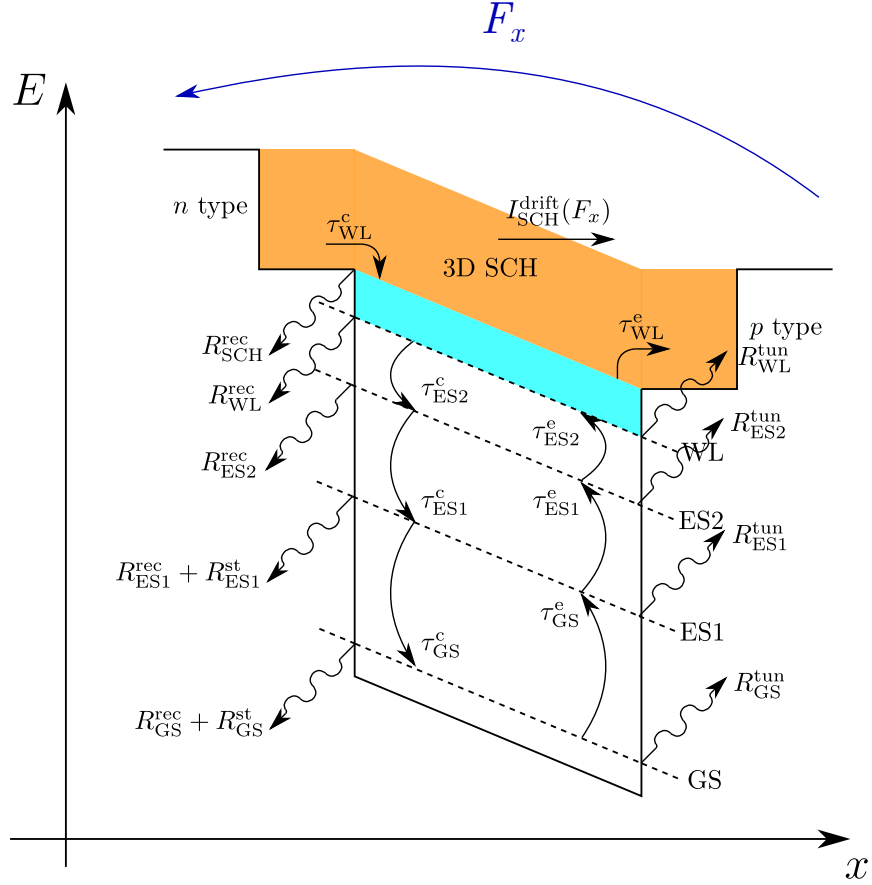


Figure 2.9: Electrons transitions between allowed states in conduction band, with an applied static electric field.

2.2.5 Concluding remarks

As previously pointed out, an ensemble of self-assembled QDs is not uniform in terms of size, composition and shape (Figure 2.10), thus leading to different characteristic interband transition energies. The ensemble can therefore be subdivided into N groups according to such transition energy, and Quantum Dots belonging to the same group are assumed to be identical. In these conditions, the physical system is said to be characterized by mixed states, since the N groups belonging to the ensemble are associated to different energy states.

The equations that have been derived during the analysis of pure states can immediately be generalized thanks to the adoption of the density matrix formalism, which accounts statistically for the presence of multiple pure substates. With this approach, the i^{th} group is characterized in terms of:

- the unique wavefunction Ψ_i describing its associated trapped carriers;
- the probability p_i for the carriers to belong to that specific group, satisfying the relation

$$\sum_{i=1}^N p_i = 1. \quad (2.89)$$

The density matrix for the complete mixed ensemble is then obtained by simply averaging the pure states density matrices by their probabilities, leading to the following generalization of Equation 2.37:

$$\rho^{\text{mix}}(t) = \sum_{i=1}^N p_i \rho^{i,\text{pure}}(t) = \sum_{i=1}^N \sum_{\mathbf{k}} p_i \rho_{\mathbf{k}}^{i,\text{pure}}(t). \quad (2.90)$$

In conclusion, it is rather straightforward that all the quantities described within the pure state framework can be generalized to the mixed states case in a similar way.

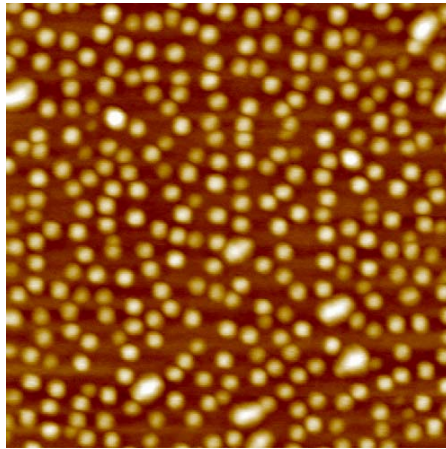


Figure 2.10: Atomic Force Microscopy image of InAs self-assembled QDs grown on a GaAs (100) substrate [42].

Chapter 3

Mode Locking in QD Lasers

3.1 General principle

As previously stated, the possibility to generate picosecond or sub-picosecond optical pulses from a monolithic device is gaining growing interest for applications in high-speed optical time division multiplexed (OTDM) and wavelength-division-multiplexed (WDM) communications. Femtosecond optical pulses can be routinely achieved in solid-state lasers based on titanium-doped sapphire material, exploiting a ML technique called *Kerr lens mode locking* [43]. However, due to the presence of a complex optical setup relying on lenses, such devices are bulky, expensive and they provide a low efficiency.

For these reasons, research efforts have recently been shifted towards more compact solutions involving monolithic semiconductor lasers that can be used for the generation of ultrashort pulses at repetition rates of tens of GHz. Mode locking in laser diodes is therefore presented in this section, starting from its general principle and an overview of the techniques introduced in Chapter 1, all aimed at the generation of micrometer- and millimeter-wave signals in lasers.

3.1.1 ML in a Fabry-Pérot cavity

In an edge-emitting laser with a Fabry-Pérot (FP) cavity, the electromagnetic field is described with a set of longitudinal modes [44], each of them with frequency

$$\omega_m = m \omega_R = m \frac{2\pi}{T_R} = m \frac{2\pi v_g}{2L} \quad m = 0, 1, \dots, \quad (3.1)$$

where m is the mode index, ω_R and T_R are the round trip angular frequency and time, respectively, v_g is the group velocity of the medium and L is the cavity length.

FP lasers are said to be *multimode*, meaning that the output field is given by the superposition of all its longitudinal modes:

$$V(t) = \sum_{m=0}^{\infty} V_m \exp [j (\omega_m t + \phi_m)], \quad (3.2)$$

where V_m is the amplitude¹ of the m^{th} longitudinal mode and ϕ_m is its phase. The latter is of great interest when considering ML operation, hence it has to be analyzed carefully in the design phase of the device.

- In general, the phases ϕ_m are randomly distributed and depend on time, meaning that the frequency of each longitudinal mode fluctuates around a certain value. In these conditions, the output signal frequency cannot be defined a priori.
- If the phases are still randomly distributed but do not depend on time (i.e. they have a constant random value), then a periodicity in the output signal can be retrieved. However, the time trace of the field intensity is still characterized by many oscillations superimposed to the required time trace, which should be a sequence of pulses with period T_R . This can be seen in Figure 3.1a, in which constant phase values randomly distributed in the range $[0, 2\pi]$ have been associated to each longitudinal mode. In some cases, a constant output signal with superimposed noise is also observed.
- When both the phase difference between adjacent modes $\Delta\phi$ and the individual phase values ϕ_m are constant in time, the *phase locking* condition is achieved. Consequently, the output signal consists of a pulse train with period T_R and much shorter duration, as it is shown in Figure 3.1b; this condition is called **amplitude modulation (AM) mode locking**.
- The width of each pulse in the time trace depends on the number of locked modes. Assuming to have N phase-locked modes all with the same amplitude V_0 , the total field magnitude can be evaluated as

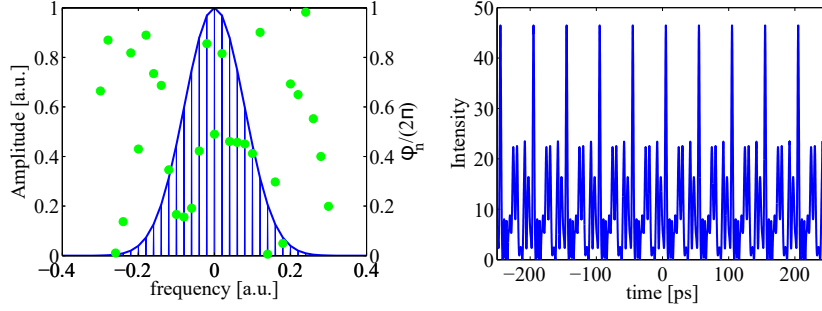
$$|V(t)| = |V_0| \frac{\sin [2\pi(N + 1) \Delta f \tau]}{\sin(2\pi\Delta f \tau)}, \quad (3.3)$$

where Δf is the constant frequency separation between adjacent modes and $\tau = t/2 + \pi\Delta\phi\Delta f$. These pulses are then separated in the time domain by a

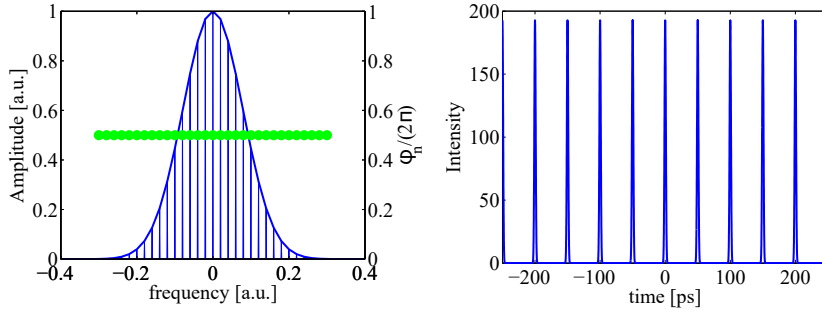
¹Notice that the number of modes that contribute to the output field is limited by the gain bandwidth of the semiconductor active material, which can work properly in a specific frequency range only. For this reason, a finite number of modes is characterized by an amplitude V_m which is significantly different from zero to actually play a role in the output field generation.

constant step $\Delta t = 1/\Delta f$, and their full width at half maximum is computed as

$$\text{FWHM} \approx \frac{1}{(2N + 1) \Delta f}. \quad (3.4)$$



(a) ϕ_m independent on time, but randomly distributed in the range $(0 \div 2\pi)$



(b) Fixed phase $\phi_m = \pi$ for all the longitudinal modes

Figure 3.1: Optical spectrum and output field time trace of a multimode laser without (a) and with (b) phase locking.

A formal description of the mode locking mechanism has been provided in [45], with a model based on coupled rate equations for three cavity modes that allows to study the time evolution of modes' amplitudes and phases. The beating between adjacent longitudinal modes causes a self-induced modulation of the carrier density in the material at multiples of the frequency spacing between them. Such carrier modulation causes the onset of dynamic refractive index and net gain variations in the homogeneous cavity material, thus leading to a four-wave mixing (FWM). Notice, however, that this type of modulation is due to interband phenomena that are dominant for mode spacings up to 1 GHz, whereas intraband effects (spectral hole burning, carrier heating) prevail for higher frequencies.

On top of this, the self-induced carrier pulsation also generates modulation

sidebands, acting as optical injection signals for the longitudinal modes. Such phenomenon can be seen in Figure 3.2, in which:

- the beating between modes E_1 (at intrinsic frequency ω_1^i) and E_2 (ω_2^i) generates an injection component $E_{inj,1}$ for the mode E_3 , moving it towards the final frequency ω_3 ;
- similarly, modes E_2 and E_3 (ω_3^i) generate a component $E_{inj,3}$, affecting the mode E_1 that is moved to frequency ω_1 .

This mechanism of *mutual injection-locking* reaches equilibrium when all the modes' spacing frequencies are locked to the same value Ω_{sp} : in these conditions, the power distribution among modes is correct and the phases are locked, meaning that the mismatch $\Delta\omega = \omega_k^i - \omega_k$ is reduced to zero.

A critical value of the initial angular frequency mismatch exists, identified as Δ_k^{\max} , above which the mutual locking of the three adjacent modes can no longer be guaranteed. Such limit value is usually lower when reducing the cavity length, since this corresponds to a decrease in the modes separation leading to strong higher-order beatings. Other parameters that should be taken into account in the ML range analysis are the linewidth enhancement factor α_H and the asymmetry between the two external modes (E_1 and E_3 in Figure 3.2), both directly affecting Δ_k^{\max} .

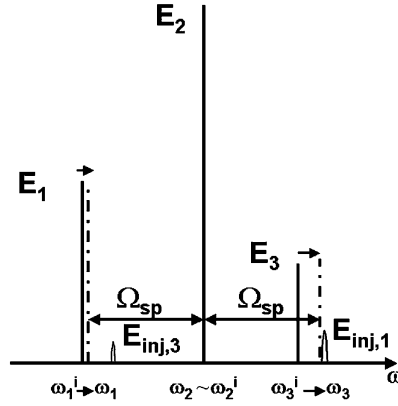


Figure 3.2: Mutual injection between three cavity modes [45].

3.1.2 Types of mode locking

Several techniques have been proposed to achieve the locking mechanism described before in real semiconductor lasers. The main ones are presented in the following, with some relevant examples taken from the literature.

Active ML

The coupling between modes can be achieved by modulating the injection current at a frequency equal to the cavity round trip one, or at one of its harmonics. In this way, the net modal gain (or equivalently the losses) experienced by the field is modulated as shown in Figure 3.3, causing a coherent power transfer from the main lasing mode to the adjacent ones. Phase locking between modes can therefore be achieved, and in particular AM mode locking is established through the so-called **active mode locking** (AML) technique.

The most straightforward approach to obtain AML is to insert an electro-optic modulator (EOM) into the laser cavity, driven by an externally applied electrical signal and producing a sinusoidal amplitude modulation of the light inside the cavity. In time domain, the EOM acts as a light switch, blocking it when “closed” and letting it pass through during the “open” periods. Notice that a rather low modulation strength is sufficient to effectively achieve phase locking, since the same pulse is attenuated in this way at each round trip: a steady state is reached after thousands of round trips, when the shortening effect introduced by the modulated losses is balanced by opposite pulse-broadening phenomena (e.g. limited gain bandwidth, chromatic dispersion). An example of this choice can be found in [46], yielding pulse widths in the range (6 ÷ 20) ps. while a more rigorous description of the underlying physical mechanisms is provided in [47].

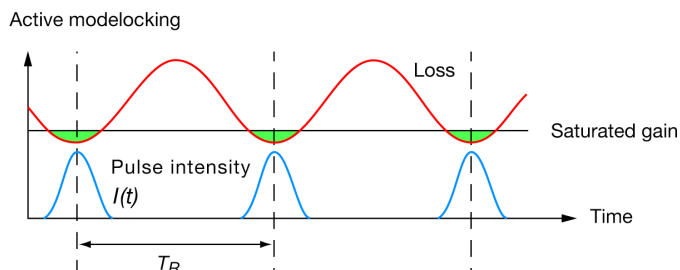


Figure 3.3: Losses modulation and pulse intensity in active mode locking [48].

Alternative approaches can also be followed in order to successfully achieve active ML in laser diodes. For instance, an acousto-optic modulator (AOM) can be inserted in the cavity instead of the more traditional EOM. This device is again driven by an electrical signal, but it induces a sinusoidal variation in the light frequency: for this reason, such mechanism relies on **frequency modulation** (FM) rather than working on the signal amplitude. The limited gain bandwidth of the material is exploited to filter out spectral components that are shifted above and below its limits, while the required one remains stable. An example of AML realized with this technique can be found in [49], with a pulse width around 2.7 ps.

Finally, a third possibility to achieve active mode locking is through external

current modulation, at the basis of the so-called *synchronous mode locking*. In this case, the pulses are directly obtained by turning on and off the laser by means of a pump source which is often another mode-locked laser (similarly to gain switching). An example relying on this approach is provided in [50]: pulse widths are lower than the AOM-based case (around 2.4 ps), but a rather accurate matching between external modulation frequency and ML laser cavity length is required.

Passive ML

A *saturable absorber* (SA) can be introduced at one end of the laser cavity to enable the phase locking between modes. The behavior of such element, which is explained more extensively in the following section, is strongly nonlinear: the circulating pulse is reshaped when crossing the SA section [51], thus achieving narrow pulses in the **passive mode locking** (PML) condition.

In general, a SA is a component whose losses are reduced at high optical intensities. When the ML pulse reaches this region, its leading and trailing edges are strongly absorbed, whereas the material losses are saturated (i.e. lower) facing the central portion of the pulse. Figure 3.4 shows the losses modulation mechanism in time domain explained before. The typical pulse width obtained with this technique is shorter than the AML case, especially when considering QD active materials allowing ultrafast recovery as in [40].

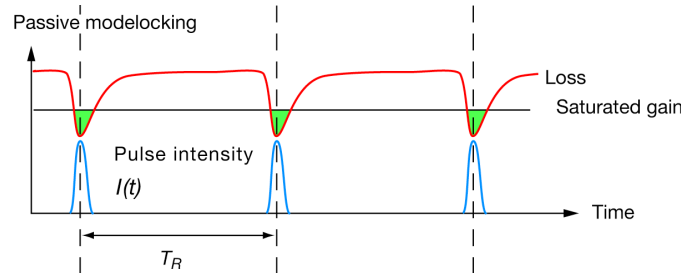


Figure 3.4: Losses modulation and pulse intensity in passive mode locking [48].

Harmonic ML

If the saturable absorber is placed at the center of a FP laser cavity, a pulse that passes through it saturates the material absorption not only for itself, but also for another one traveling in the opposite direction and simultaneously reaching the SA. Two optical pulses are therefore present in the cavity, and they collide in the absorber: the obtained repetition rate is consequently twice the fundamental one, determined by the cavity length. For this reason, such technique is called **colliding pulse mode locking** (CML), or **harmonic mode locking**.

Notice that this technique allows to achieve stable pulse trains at higher frequencies with respect to AML and PML, and it can be realized in both edge-emitting [52] or ring-shaped devices [53]. Concerning the latter, two pulses traveling in the cavity are always expected to collide in the SA section, which can therefore be placed at any point of the structure. However, the possibility of having a unidirectional light propagation along the structure should be considered, achievable with different approaches as explained at the end of this Chapter. Harmonic ML can still be achieved in these conditions, even though no pulses are colliding along the cavity.

Hybrid ML

In the **hybrid mode locking** (HML) technique, the presence of both current modulation (typical of AML) and saturable absorber (inherited from PML) are exploited to lock the modes' phases. In this way, a higher degree of flexibility is introduced, since both modulation and pulse shaping can be trimmed in order to obtain the required performances. This clearly causes an increased complexity when identifying the working regions, with specific methods presented in [54].

The RF modulation signal can also be applied to the absorber negative voltage, while keeping the injected current constant in the active regions. Such choice often yields better results due to the higher series resistance of the reverse biased SA section with respect to the gain portions, in which current modulation is strongly limited by the electrical RC bandwidth [55, 56].

Self ML

Mode locking has also been reported in single-section FP lasers with CW applied current, and **self mode locking** (SML) is said to occur [57], also known as Optical Frequency Comb (OFC) [58]. These devices are clearly less complex than the ones required for the other techniques, with a single electrode necessary for the external control; however, this simplicity is paid in terms of tunability, as well as pulse quality and power management [59]. Moreover, small variations in the device fabrication can lead to relevant changes in its behavior, thus highlighting a low robustness with respect to process variations [60].

3.2 ML with saturable absorbers

In this section, an insight on mode-locked laser diodes relying on one or more saturable absorber sections is presented, starting from the description of different device structures that have been proposed in the literature. Then, a reference structure is chosen to illustrate the complementary behavior of gain and SA sections, followed by a more specific focus on the parameters that characterize the latter.

3.2.1 Device configurations

Figure 3.5 reports some of the cavity configurations that have been proposed in order to obtain the mode locking condition in laser diodes with a SA.

The first demonstrations of both active [61] and passive [62] ML in semiconductor lasers have been achieved with a configuration similar to the one reported in Figure 3.5a. Here, the laser is placed in an external cavity including both gain (forward biased) and SA (reverse biased) sections, which can either be discrete or monolithically integrated. The insertion of an external reflector realized through diffraction grating (Figure 3.5b) allows to perform a frequency tuning of the emitted radiation, thanks to its wavelength selectivity. However, this setup is bulky and fragile: more recent devices rely on a single chip on which all the required functions can be integrated [63].

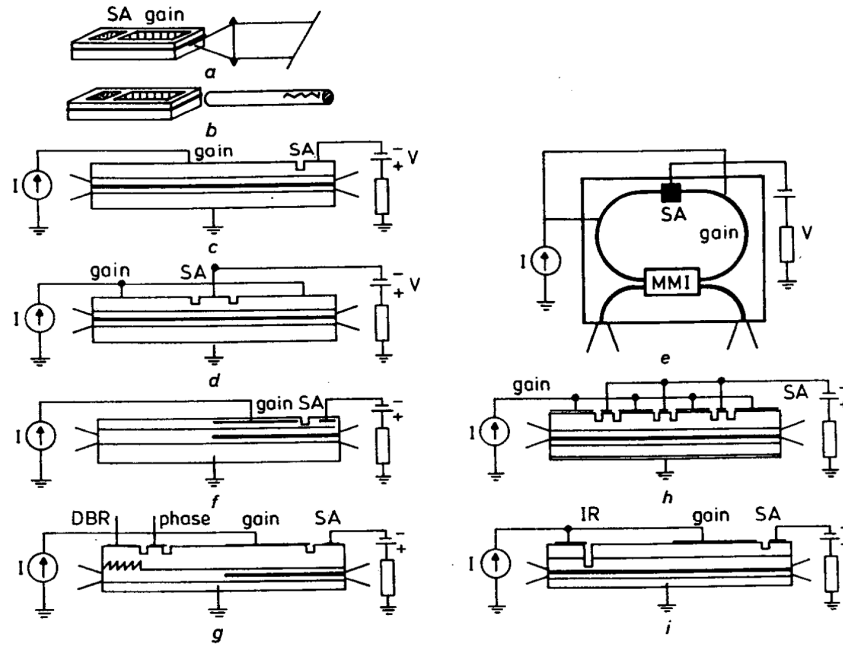


Figure 3.5: Examples of ML laser diodes configurations with a saturable absorber [52].

The simplest configuration for a monolithic cavity, similar to the one proposed in [64], is reported in Figure 3.5c. This structure can be used for both passive and hybrid mode locking, the latter relying on the electro-absorption effect of the SA section when modulated with an AC voltage. As discussed before, harmonic mode locking can also be achieved by placing the SA section in the center of the cavity (Figure 3.5d), or exploiting a ring structure (Figure 3.5e).

Increasing the device complexity, a higher degree of tunability can be achieved.

As an example, a passive waveguide can be integrated in the monolithic structure in order to reduce the threshold current while improving the robustness to noise (Figure 3.5f). A distributed Bragg reflector (DBR) can also be inserted to control the emission wavelength of the pulses (Figure 3.5g). Finally, a more refined control of the CML regime is possible by introducing a higher number of SA sections along the cavity (Figure 3.5h), with an overall repetition rate that has to be determined accordingly.

3.2.2 Pulse amplification and shaping

The basic structure that will be analyzed in the following is depicted in Figure 3.6. Overall, a ridge waveguide can be identified in this schematic, with two electrically isolated portions that represent the gain (with current injection) and absorption (under reverse bias voltage) sections. Such device is taken as a reference in the description of the phenomena leading to passive ML in semiconductor lasers, and the same considerations can easily be extended to multi-section devices designed to work in harmonic mode locking condition.

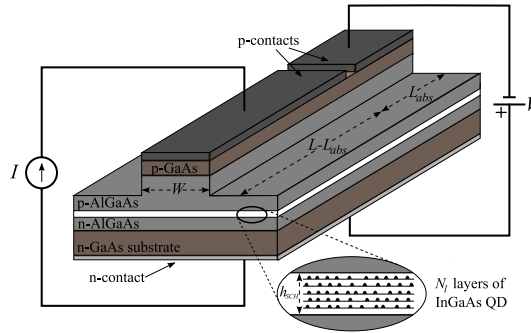


Figure 3.6: Reference structure for passive mode locking in QD lasers [18].

Pulse amplification in the active section

Injecting a current into a semiconductor material ensures the carrier inversion condition in the biased region, thus leading to a net modal gain for the electromagnetic wave propagating in the cavity. In particular, the following phenomena take place when a high-energy pulse reaches the active section of a ML laser.

1. The leading edge of the pulse is amplified with a specific gain per unit length.
2. Due to stimulated emission processes, a large recombination is induced in the energy states resonant with the pulse frequency, leading to a strong depletion of these states.

3. The aforementioned depletion may lead to a non-equilibrium distribution for electrons and holes within the semiconductor material called *spectral hole burning*, while for intense enough pulses a significant depletion of the total carrier density in the active medium may take place.
4. As a consequence, the gain reduces and the following portions of the pulse experience a *gain compression*, i.e. a reduced amplification.
5. The gain tends to recover its initial value with a characteristic time constant that depends on the carriers intraband dynamics, hence the trailing edge amplification is usually much larger than the central portion of the pulse.

Overall, a pulse traveling along a gain section is subject to a nonlinear amplification, larger in its outermost regions and therefore causing a **pulse broadening**. Notice that distortion phenomena may also arise in the case of highly energetic pulses, causing the signal to be useless for the target application.

Pulse shaping in the saturable absorber

The coupling between longitudinal modes of a laser in passive or harmonic ML regime is provided by the nonlinear absorption saturation in the reversely biased section, referred to as the saturable absorber. A dual behavior with respect to the gain section can be identified.

1. The leading edge of an incoming pulse is strongly absorbed, due to the interaction with the biased material.
2. In the energy states resonant with the pulse, optical generation of electron-hole pairs causes the carrier density to increase following this absorption.
3. The excess concentration of carriers tends to saturate the absorption mechanism, again with a nonlinear dynamic, so in this case the central portion of the pulse undergoes an *absorption bleaching* and it is less attenuated.
4. Photo-generated carriers are then leaving their energy levels due to thermionic escape, tunneling and recombination processes.
5. The absorption tends to recover its initial unsaturated value (again with a characteristic time constant), so the trailing edge of the optical pulse experiences a higher absorption with respect to its central portion.

The nonlinear absorption of a pulse traveling along the SA section allows to perform a **pulse shaping**, since its outermost portions undergo a stronger attenuation with respect to the central one. Clearly, such pulse shaping must compensate the broadening that takes place in the active section in order to achieve a stable ML condition.

3.2.3 SA parameters

Saturable absorbers can be realized in two different geometries. The most straightforward one is known as the *waveguide saturable absorber*, and it is directly realized by reversely biasing a section of the laser structure. Thanks to its simplicity and compactness, such choice is typical for integrated optical circuits and in-plane semiconductor lasers, hence the devices presented in this Thesis rely on it.

A second possibility is to combine a stacked DBR structure with a standalone semiconductor SA, in the so-called *semiconductor saturable absorber mirror* (SESAM) configuration. In this case, the reflectivity increases with the incoming optical power, thanks to the loss saturation in the semiconductor material.

Irrespective of the chosen geometry, a set of parameters has to be considered carefully when designing a saturable absorber, and the main ones are introduced in the following.

- **Modulation depth (or strength)**: it represents the difference between saturated and unsaturated behavior of the absorber. When dealing with a waveguide SA, it can be determined by simply considering the absorption coefficient variation in the two cases, i.e.

$$\alpha_{\text{sat,abs}} = \alpha_{\text{uns,abs}} - \alpha_{\text{ns,abs}}. \quad (3.5)$$

In Equation 3.5, the saturated losses $\alpha_{\text{sat,abs}}$ have been obtained by subtracting the non-saturable ones $\alpha_{\text{ns,abs}}$ (introduced for instance by mirrors) from the initial unsaturated value $\alpha_{\text{uns,abs}}$. Equivalently, the associated extinction ratio can be expressed as

$$\text{ER}_{\text{abs}} = \exp \left[\Gamma_{xy} (\alpha_{\text{uns,abs}} - \alpha_{\text{ns,abs}}) L_{\text{abs}} \right], \quad (3.6)$$

where Γ_{xy} and L_{abs} represent the waveguide confinement factor and the SA section length, respectively.

- **Recovery time**: it is the characteristic time needed for the SA to recover from its saturated condition. From a physical perspective, the absorption saturates when the number of photo-generated carriers is rather high, following an increase in the optical intensity of the incoming ML pulse. In order to restore its unsaturated properties, a massive depletion should therefore take place, possibly enhanced by the presence of an applied negative bias voltage. Clearly, the recovery time must be significantly shorter than the repetition period, whereas its relationship with the pulse duration is less straightforward: the SA is said to operate between two limit cases, known as *slow* and *fast saturable absorber regimes*, depending on whether its characteristic time is longer or shorter than the provided pulse width.

- **Saturation fluence:** this parameter expresses how fast the SA is able to saturate its absorption coefficient with the incoming light pulse. In the slow SA case, the absorber saturation can be approximated as [27]

$$\alpha_{\text{abs}}(F_{\text{in}}) \approx (\alpha_{\text{uns,abs}} - \alpha_{\text{ns,abs}}) \exp\left(-\frac{F_{\text{in}}}{F_{\text{sat}}}\right) + \alpha_{\text{ns,abs}}, \quad (3.7)$$

where the incident light fluence F_{in} is determined as the integral of the incident power normalized to the SA cross section:

$$F_{\text{in}}(t) = \frac{1}{A_{\text{abs}}} \int_{-\infty}^t P_{\text{in}}(\tau) d\tau. \quad (3.8)$$

From Equation 3.7, the saturation fluence F_{sat} should be as low as possible in order to have a responsive SA with respect to input light fluctuations. However, assuming a constant value for this parameter is possible only in the case of slow SA, while it can be affected by external parameters (such as pulse duration and shape) when the recovery time approaches the ML pulse width. On the other hand, the characterization of a fast absorber should rely on the input saturation intensity I_{sat} (power per unit area):

$$\alpha_{\text{abs}}(I_{\text{in}}) \approx \frac{\alpha_{\text{uns,abs}} - \alpha_{\text{ns,abs}}}{1 + I_{\text{in}}/I_{\text{sat}}} + \alpha_{\text{ns,abs}}. \quad (3.9)$$

- **Linewidth enhancement factor (LEF):** this parameter allows to describe the self-phase modulation and chirp introduced by the SA section and affecting the ML pulse. A refractive index change causes a variation in the dynamic properties of semiconductor lasers, modeled by means of the Henry parameter [65] defined as

$$\alpha_{\text{H}} = -\frac{4\pi}{\lambda} \frac{dn_{\text{r}}/dn}{dg/dn}. \quad (3.10)$$

In Equation 3.10, which is valid at the emission wavelength λ , the variation of both material refractive index n_{r} and gain per unit length g with respect to the carrier density n is considered. Notice that the Henry factor is rather similar to the chirp parameter of a conventional electro-absorption modulator, given the analogies between such structure and the SA introduced in this context, with typical values in the range $\alpha_{\text{H}} = (0 \div 1)$. On the contrary, semiconductor amplifiers and lasers based on QW material are generally characterized by a higher linewidth enhancement factor, approximately $\alpha_{\text{H}} = (2 \div 3)$, thus leading to stronger self-phase modulation and chirp phenomena. This effect is automatically included in the model presented in the following by means of Kramers-Krönig relations.

3.3 ML in QD lasers

Semiconductor Quantum Dots have been extensively investigated in recent years as active media for passively mode-locked laser diodes. The reason behind this growing interest is related to a number of potential advantages and peculiar properties enabled by the presence of nanometric features in the cavity [66]. An overview of these properties is provided in this section, followed by a state of the art analysis concerning QD-based lasers exploited in mode locking condition.

3.3.1 Typical characteristics

The introduction of QD materials in the SA and gain sections of a monolithically integrated laser diode has brought a set of advantages and peculiar phenomena that have been widely investigated in the literature. The main features reported in the description of QD-based SA and active materials are briefly outlined.

Peculiar features of QD saturable absorbers

The basic principles at the basis of SA operation are the same in the case of bulk, QW and QD materials. The latter, however, exhibit some characteristic traits that may lead to possible improvements concerning different figures of merit of such component.

- **Absorption bandwidth:** this is the main feature to describe the operation of SA materials, since expressing the time required for the absorber to be efficiently saturated. The absorption bandwidth is *finite*, and mainly determined according to the inhomogeneous broadening, in the case of self-assembled QD materials. This is in contrast with the *semi-infinite* bandwidth reported in bulk and QW materials, in which any photon with energy higher than the material bandgap can in principle be absorbed. Notice, however, that such bandwidth cannot be efficiently saturated over its whole range: carrier-carrier interactions lead to thermalization processes at the picosecond or sub-picosecond scale, hence the slow absorption saturation mechanism is ensured in a narrow spectral region near the absorption cut-off, whereas fast absorption saturation (usually weak, due to spectral hole burning) prevails for higher-energy carriers. On the other hand, carrier-carrier scattering phenomena are replaced by slower capture and escape characteristic times in QD materials, leading to the prevalence of slow absorption saturation in the whole band and consequently to a broader range of tunability for the generation of ultrashort optical pulses.
- **Absorption recovery:** QD materials intrinsically exhibit ultrafast carrier dynamics. This allows to exploit them for the realization of saturable absorbers in ML lasers working at rather high repetition rates, in which the

absorption recovery must take place within the round trip time of the cavity. Several research contributions can be found in the literature concerning this characteristic time, which is not further investigated in this Thesis. As an example, [67] reports a theoretical interpretation of this phenomena based on a time constant approach.

- **Saturation fluence:** the optical power associated to each pulse traveling along a ML laser cavity is usually rather small, especially when considering high repetition rates. Thanks to the delta-like DOS of QD materials, the saturation fluence F_{sat} is lower than in bulk or QW materials, and this allows the self-starting of ML even at rather small pulse energies. Further details concerning the physical processes behind the absorption saturation in QD materials can be found in [27].

Other features

Quantum Dots usage is not limited to the SA section of ML lasers, strictly required for passive, hybrid and harmonic mode locking: additional improvements in the device performance can be obtained by exploiting QDs in the gain sections, too.

- **Gain bandwidth:** due to the non-uniform distribution of sizes in the self-assembled QD ensemble, the gain spectrum experiences the inhomogeneous broadening introduced in Subsection 2.1.3. Even though this may seem an issue, it actually represents one of the main motivations for the insertion of Quantum Dots in ML lasers, since allowing to achieve a broad gain bandwidth that leads to the presence of many longitudinal modes in the cavity, and therefore to the generation of ultra-short pulses with sub-picosecond widths. The inhomogeneous nature of gain may also enable better performances in terms of jitter and relative intensity noise between adjacent comb components.
- **Reduced gain levels:** increasing the dots inhomogeneity (and therefore the gain-bandwidth) has a detrimental effect on the maximum net modal gain that can be achieved from the QD GS transitions. Below a certain threshold, ES transitions become predominant while GS ones are inhibited. At the moment, the most promising results in terms of ML stability have been obtained with GS lasing only, but the simultaneous presence of both ground and excited state transitions may be useful in applications such as time-domain spectroscopy, optical interconnects, wavelength-division multiplexing and ultrafast optical processing [68, 69].
- **Gain recovery:** an ultrafast sub-picosecond gain recovery has been identified experimentally in layers of self assembled InAs QDs [70, 71], conversely with respect to the expected slow intraband carrier dynamics that could have

represented a limit in the applicability of QD active materials in sub-THz devices. From a theoretical perspective, such ultrafast dynamics cannot be attributed to electron-phonon scattering, but it has been explained by the occurrence of efficient Auger electron-electron scattering processes [72]. However, the time scale of these relaxation processes is still longer than that of Quantum Wells, due to the enhanced spectral hole burning non-linearities found in zero-dimensional materials.

- **Threshold current:** in the presence of QD-based devices, the threshold current required for lasing operation to start is rather low, and ML is usually achieved for injection levels just above such lower limit. This clearly represents an outstanding advantage with respect to bulk or QW devices, which require higher bias values to operate correctly, thus incurring in lower efficiencies and possibly increased optical noise due to amplified spontaneous emission.
- **Temperature sensitivity:** thanks to the discrete nature of the QD density of states, the performance dependence with respect to temperature is strongly reduced in devices relying on such technology. Also in this case, relevant benefits in terms of cost and footprint are introduced, since thermo-electric coolers or other temperature control systems are not strictly required.
- **Linewidth enhancement factor:** the possibility of achieving an ideally null LEF, enabled by the gain spectrum symmetry in QD structures, is rather appealing for a wide range of applications. Notice, however, that changes in the refractive index due to the presence of carriers in the excited states lead to an increase in the Henry parameter of the device, which can therefore be considered to be small for bias current values close to the threshold [73].

3.3.2 State of the art analysis

In the following, some relevant examples of mode-locked QD-based laser diodes taken from the literature are presented. A chronological order has been chosen for this overview, starting from the oldest results (up to 2010) and then moving to more recent ones. Relevant information related to ML type, emission wavelength, repetition rate and pulse width or power are reported according to their availability in the chosen references.

First results

One of the first demonstrations of passively mode-locked lasers based on QD material dates back to 2001, and it is reported in [74]. The device has been realized by exploiting MBE on a (001) n^+ -doped GaAs substrate, with an active region consisting of two InAs DWELL layers and GS emission at $\lambda_{GS} = 1278$ nm.

The authors present here a two-section laser diode with a repetition rate of $f_R = 7.4$ GHz (Figure 3.7a), with gain and SA lengths equal to $L_{\text{gain}} = 4.73$ mm and $L_{\text{abs}} = 850$ μm , respectively. The threshold current depends on the applied bias voltage, and in general its value is in the range $I_{\text{th}} = (30 \div 40)$ mA (Figure 3.7b). The pulse width reported in this paper, measured through an autocorrelation function assuming a hyperbolic secant-squared pulse, is $\Delta\tau = 17$ ps. This value increases at higher injection current values, since the modulation depth of the mode-locked pulse decreases (Figure 3.7c). Concerning the spectral properties, a $\Delta\lambda \approx 1$ nm has been reported, as it can be seen from Figure 3.7d.

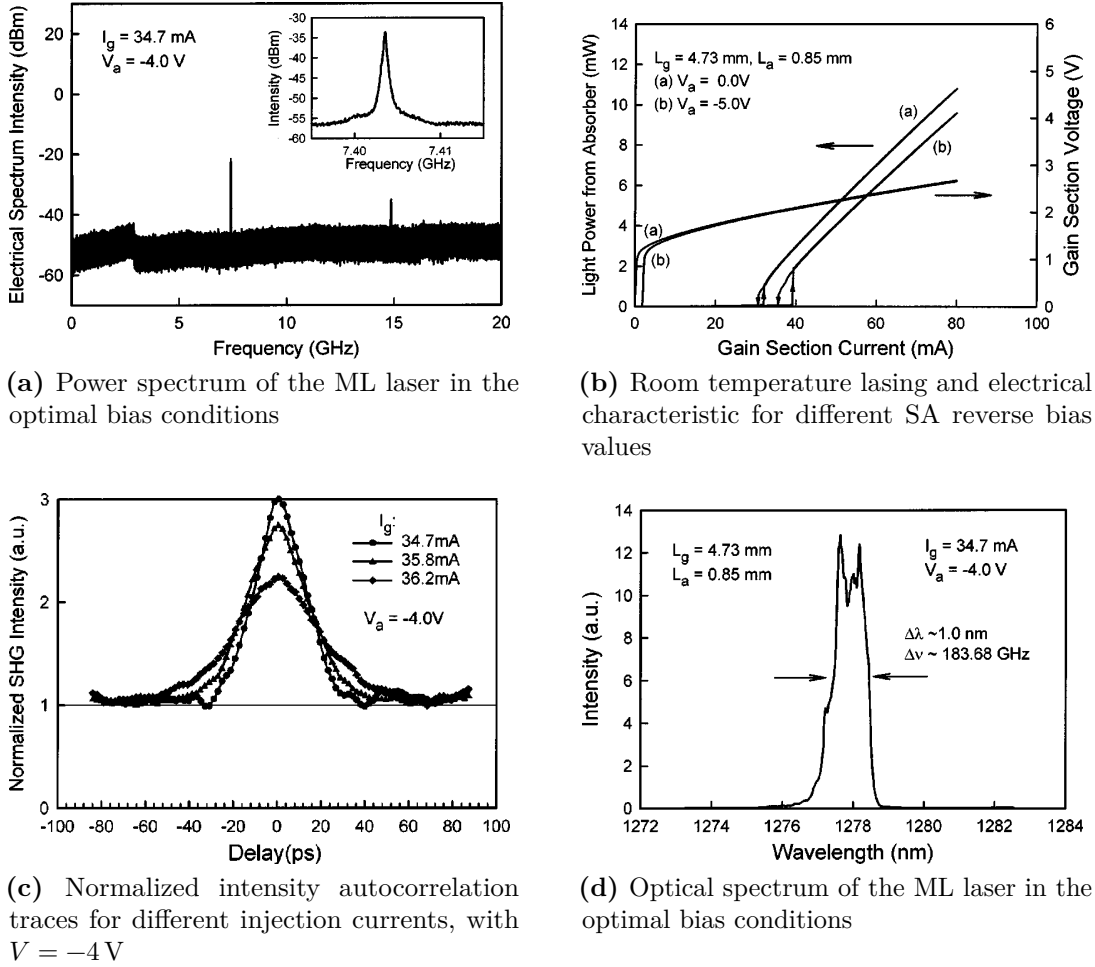


Figure 3.7: Significant results reported by Huang et al. [74].

In [75] the first example of hybrid ML in QD-based devices has been reported, three years later with respect to the previous reference. From the technological perspective, three layers of self-assembled $\text{In}_{0.5}\text{Ga}_{0.5}\text{As}$ have been grown epitaxially

on a GaAs:Si substrate by means of metal organic chemical vapor deposition (MOCVD), and embedded in a GaAs confinement layer.

A fundamental repetition rate $f_R \approx 10$ GHz has been obtained with a 3.9 mm cavity length, divided into $L_{\text{gain}} = 3.57$ mm and $L_{\text{abs}} = 330$ μm . Figure 3.8a reports the power spectra for HML and PML, the former obtained with a 10 GHz, 12 dB RF drive signal superimposed to the constant bias voltage of the SA section (equal to $V = 1.06$ V in both cases). The pulse width has been estimated to be lower than $\Delta\tau = 14.2$ ps (the exact value is not reported due to instrumentation limitations), while the FWHM of the optical spectrum is $\Delta\lambda \approx 0.8$ nm, as reported in Figure 3.8b. Finally, the measured pulse peak power is also provided, equal to $P_{\text{max}} = 4$ mW.

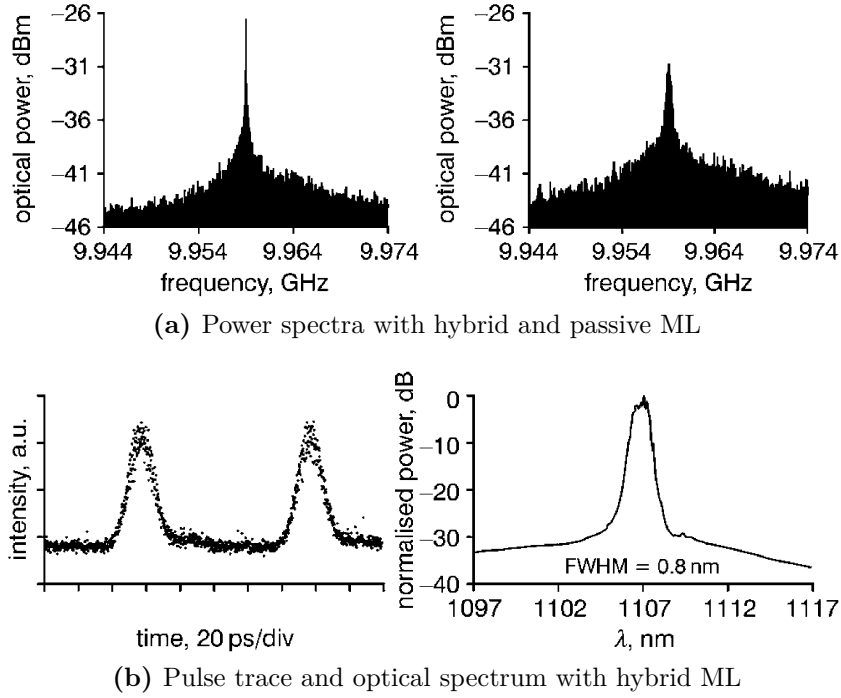


Figure 3.8: Significant results reported by Thompson et al. [75].

The same research group [76] reported the results obtained for a passive ML laser realized through MBE of a 10-layer stack of InAs QDs on GaAs:Si substrate, emitting at GS wavelength $\lambda_{\text{GS}} = 1290$ nm.

The proposed device is shorter, with $L_{\text{gain}} = 1.6$ mm and $L_{\text{abs}} = 600$ μm , hence the fundamental repetition rate is higher and approximately equal to $f_R \approx 18$ GHz (Figure 3.9a). In the time domain, a $\Delta\tau = 10$ ps pulse width has been obtained by assuming again a squared hyperbolic secant pulse profile, whereas the spectral bandwidth is reduced with respect to the previous cases, as it can be seen from Figure 3.9b.

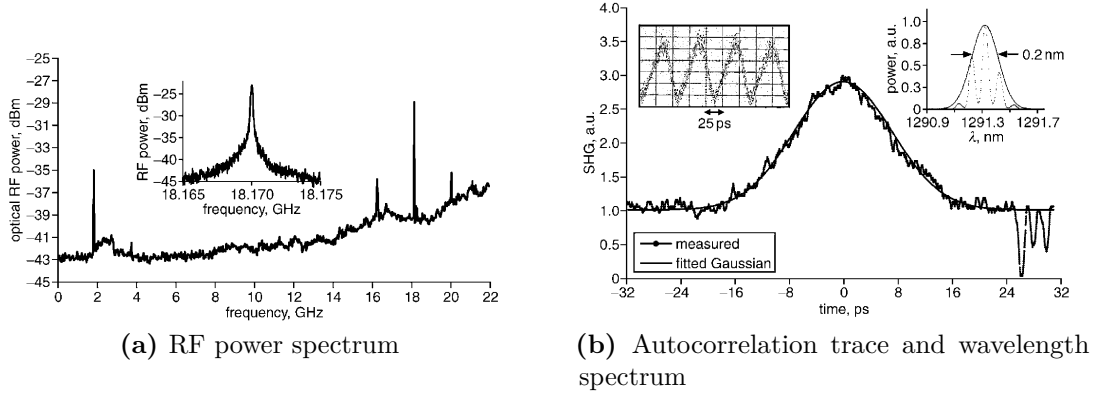


Figure 3.9: Significant results reported by Thompson et al. [76].

Some interesting results in terms of ultrashort, high power pulse generation in a relatively broad spectral range are reported in [77]. The reference device has been grown by means of MBE on a (100) GaAs substrate, with five self-assembled $\text{In}_{0.4}\text{Ga}_{0.6}\text{As}$ QD layers separated by GaAs barriers.

Apart from the relatively high repetition rate, equal to $f_R \approx 21$ GHz (lengths $L_{\text{gain}} = 1.8$ mm, $L_{\text{abs}} = 300$ μm), the most interesting results have been obtained in terms of pulse duration ($\Delta\tau = 390$ fs) and output peak power ($P_{\text{max}} \approx 1$ W, with pulses 2 ps wide). Clearly, the required bias values to achieve these impressive features are rather high, thus implying larger power consumption that may represent a strong limitation in the applicability of such device. The time trace and its corresponding optical spectrum for $I = 185$ mA and $V = -7.6$ V are reported in Figure 3.10a, whereas Figure 3.10b reports an interesting overview of the optical spectrum evolution as a function of the bias current, with fixed SA voltage $V = -8$ V.

The laser structure proposed in [78] for high-speed fiber communication links has been again realized with MBE on a n^+ -doped GaAs substrate, with a repetition rate of $f_R = 5.2$ GHz due to the rather long cavity ($L_{\text{gain}} = 6.8$ mm, $L_{\text{abs}} = 1$ mm). The performances of this device have been then summarized in [79]: the measured pulse width is equal to $\Delta\tau = 5.7$ ps (Figure 3.11a), whereas the maximum pulse power reported is $P_{\text{max}} = 290$ mW.

Complementary results have been reported in [80], where a similar device is characterized in terms of temperature stability within the range $T = (30 \div 60)$ $^{\circ}\text{C}$ (Figure 3.11b). Rather high ML peak power values, in the range $P_{\text{max}} = (0.9 \div 1.7)$ W, have been obtained with pulse widths $\Delta\tau = (3.2 \div 7)$ ps.

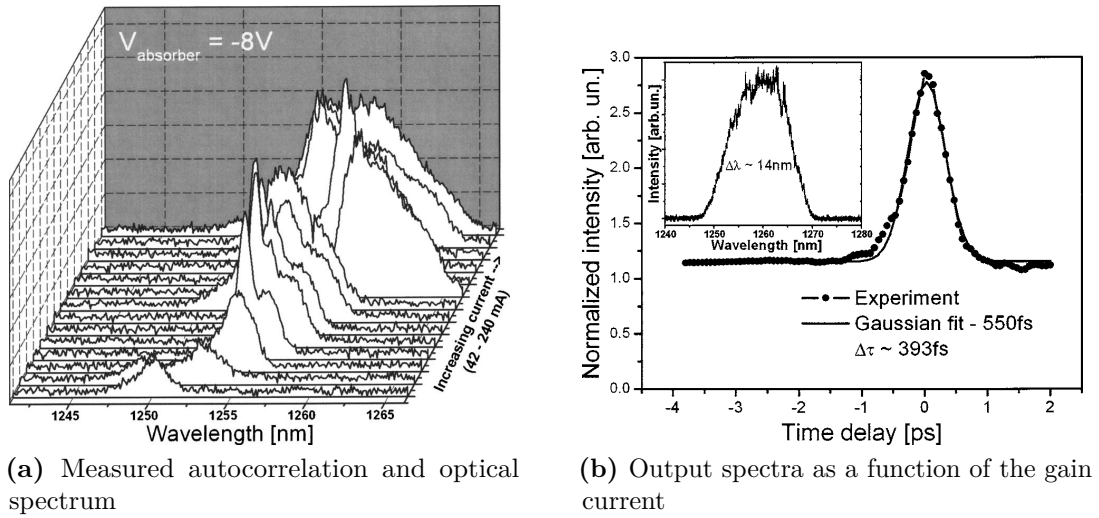


Figure 3.10: Significant results reported by Rafailov et al. [77].

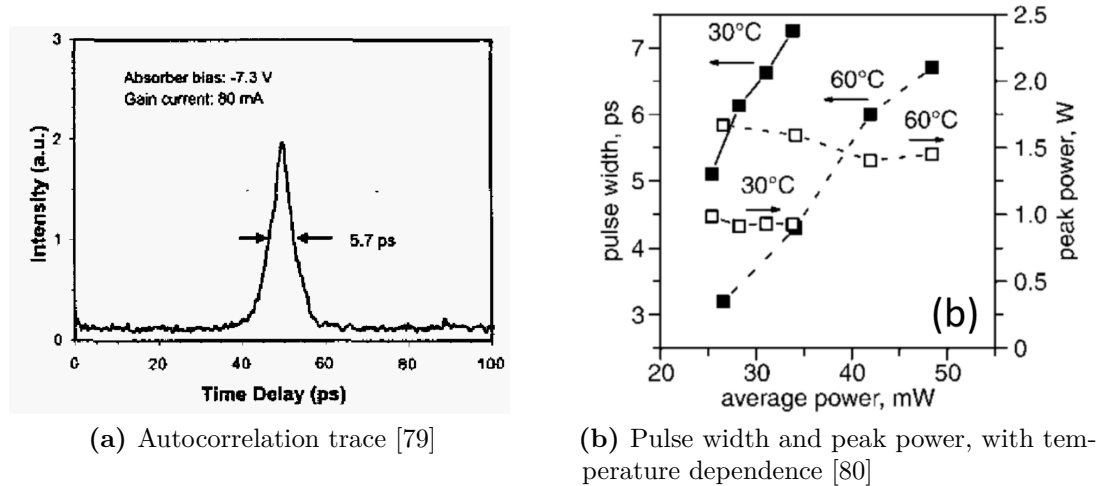


Figure 3.11: Results referred to the device presented in [78].

A comparison between PML and HML has been proposed in [56]. The laser source is characterized by an $\text{Al}_{0.35}\text{Ga}_{0.65}\text{As}/\text{GaAs}$ structure incorporating a 10-layer stack of InGaAs QDs emitting at $\lambda_{\text{GS}} = 1.28 \mu\text{m}$ grown by MBE.

The total length of the cavity is varied in the range $(500 \div 2000) \mu\text{m}$, with a 9 : 1 gain-to-SA length ratio, thus obtaining repetition rates $f_{\text{R}} = (80 \div 20) \text{GHz}$. In the shortest device case, a relatively small gain current is required to achieve PML (below 60 mA), while the bias voltage needs to be larger in absolute value than -4V to ensure the correct pulse shape. The main results in terms of ML

map and pulse width (with minimum values around $\Delta\tau = 1.5$ ps) are reported in Figure 3.12. Concerning HML, the resulting pulse width can be reduced to values below 2 ps, clearly paying in terms of overall device complexity due to the presence of an additional synchronizing mechanism to perform the correct modulation.

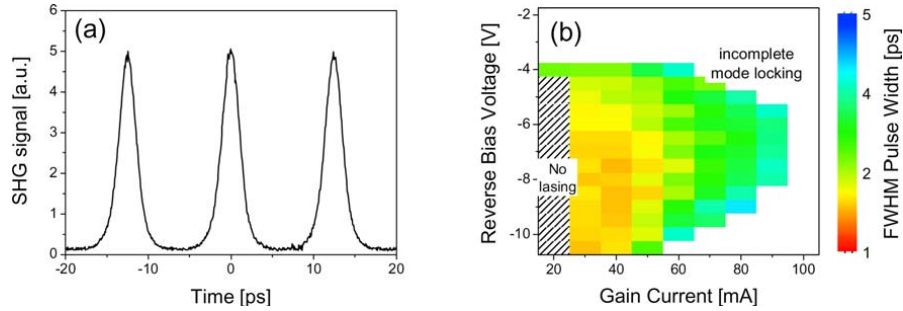


Figure 3.12: Significant results reported by Bimberg et al. [56].

The first example of colliding pulse ML has been reported in [81], obtained in a 3.9 mm long laser diode with three layers of InGaAs QDs emitting at $\lambda = 1.1 \mu\text{m}$, and in which the SA section is placed at the center of the device with a tolerance of $\pm 0.5 \mu\text{m}$ (Figure 3.13a).

The fundamental frequency of this device is $f_R = 10$ GHz, but the associated component is strongly suppressed and below the noise floor of the RF spectrum. On the other hand, the strongest peak in the spectrum is obtained as expected at $f = 2 \times f_R = 20$ GHz, providing evidence of the colliding pulse mechanism at twice the fundamental cavity frequency. Concerning the other figures of merit, the best pulse width achieved is $\Delta\tau = 7$ ps (Figure 3.13b), with a reverse bias voltage in the range $(-1.2 \div 0)$ V to guarantee the stability of the CML.

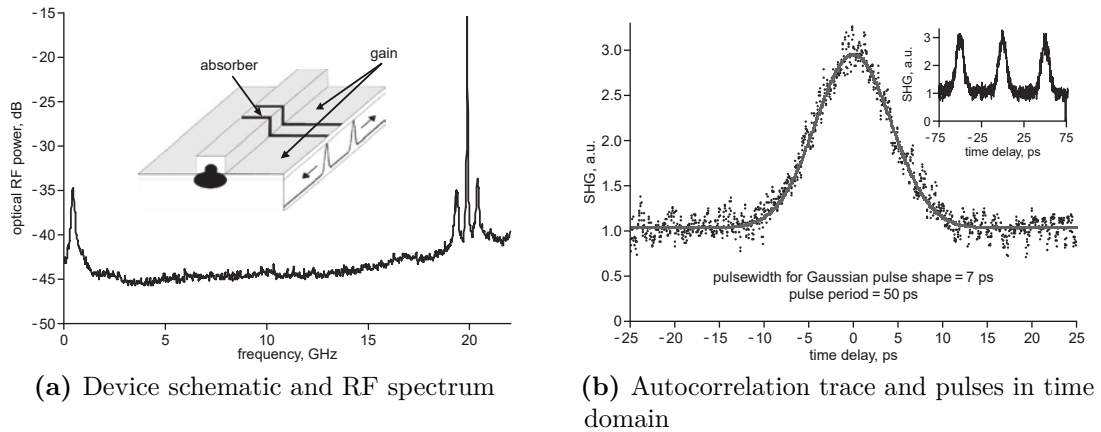


Figure 3.13: Significant results reported by Thompson et al. [81].

In [82], a thorough analysis of a QD laser diode in passive ML regime is carried out. This device is characterized by the presence of 15 self-organized InAs layers embedded in InGaAs Quantum Wells, with an overall length of 1 mm (given by the sum of $L_{\text{gain}} = 900 \mu\text{m}$ and $L_{\text{abs}} = 100 \mu\text{m}$) that corresponds to a fundamental repetition rate $f_{\text{R}} = 40 \text{ GHz}$.

The Authors report several plots that allow to establish how the bias values affect different device properties. For instance, the pulses FWHM clearly tends to reduce when increasing the reverse bias voltage (Figure 3.14a), whereas their average power decreases (Figure 3.14b). The locking range for the same device operated in hybrid mode locking conditions is also reported: it is synchronized with a 40 GHz, 14 dBm wave generator, yielding a maximum locking range of 30 MHz that decreases at higher injection currents as shown in Figure 3.14c.

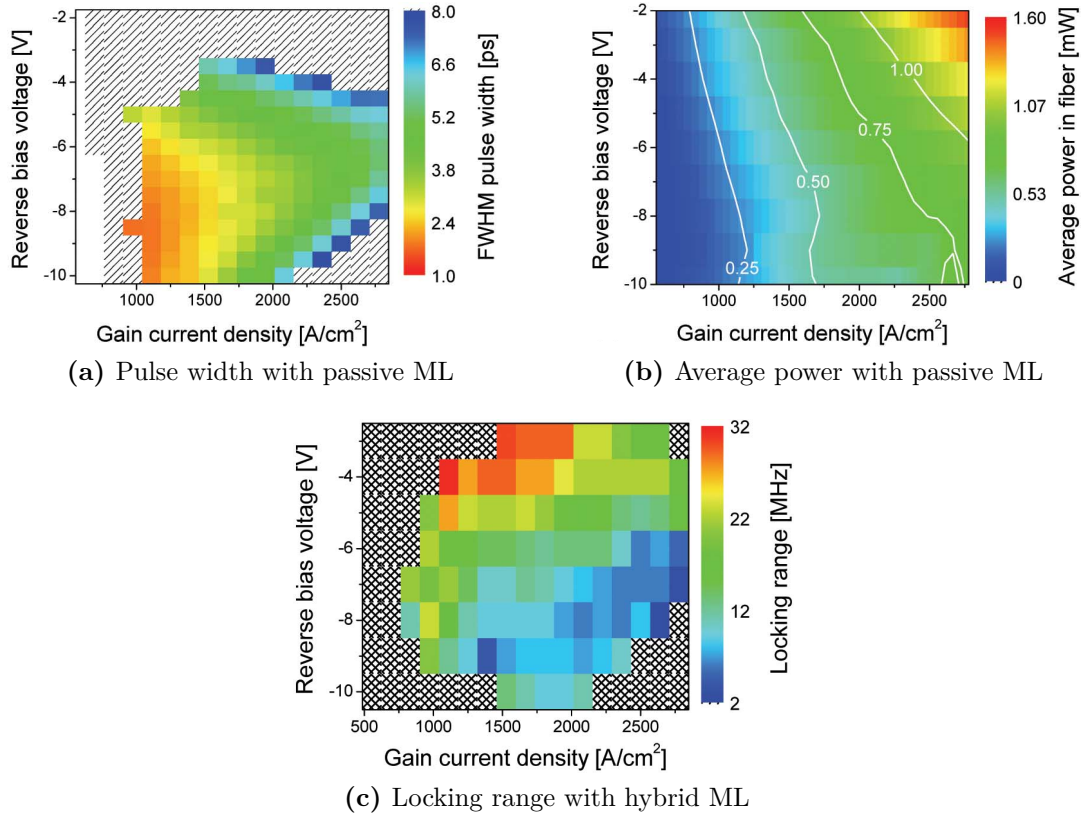


Figure 3.14: Significant results reported by Kuntz et al. [82].

Concerning self ML devices, the structure proposed in [83] allows to achieve it with a dual-wavelength emission: one central wavelength of the laser is located in the C-band ($\lambda_{\text{C}} = 1543.7 \text{ nm}$), while the other is in the L-band ($\lambda_{\text{L}} = 1571.7 \text{ nm}$). Five InAs QD layers, grown with chemical beam epitaxy, are embedded in the

InAs/InP laser structure, with a cavity length of $456\ \mu\text{m}$ that leads to a $92.5\ \text{GHz}$ fundamental frequency. Notice that the pulse width is lower when considering only emission at wavelength λ_L ($\Delta\tau = 930\ \text{fs}$, Figure 3.15a) with respect to the case with both wavelengths ($\Delta\tau = 930\ \text{fs}$, Figure 3.15a). Finally, the average power at injection current equal to $60\ \text{mA}$ has been reported to be equal to $9\ \text{mW}$. Notice that very similar results have been obtained separately for C-band [84] and L-band [85], again relying on self ML to obtain the optical frequency comb.

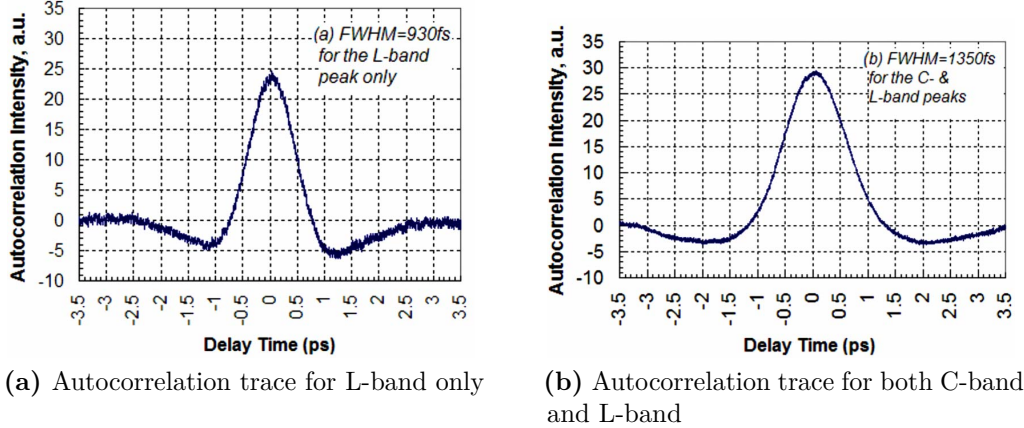
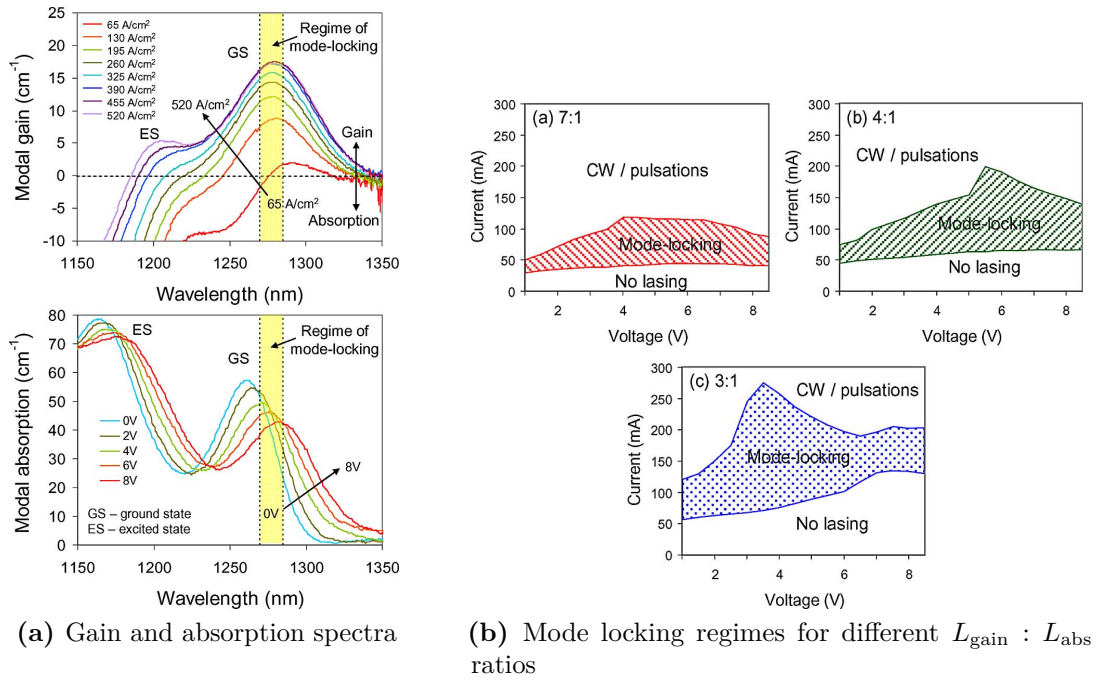


Figure 3.15: Significant results reported by Liu et al. [83].

The main advancements in two-section PML QD lasers up to the year 2009 are summarized in [86], where a InGaAs DWELL structure grown on a GaAs substrate through MBE is characterized in terms of gain and absorption spectra (Figure 3.16a), ML map (Figure 3.16b), pulse duration $\Delta\tau$, time-bandwidth product ($\text{TBP} = \Delta\tau \times \Delta\nu$), spectral width $\Delta\lambda$, central wavelength λ_{GS} , average and peak power P_{avg} and P_{max} . The main results are reported in Figure 3.16c in two different cases, varying the bias voltage with a fixed current value ($I = 66\ \text{mA}$) and vice versa ($V = -8\ \text{V}$).

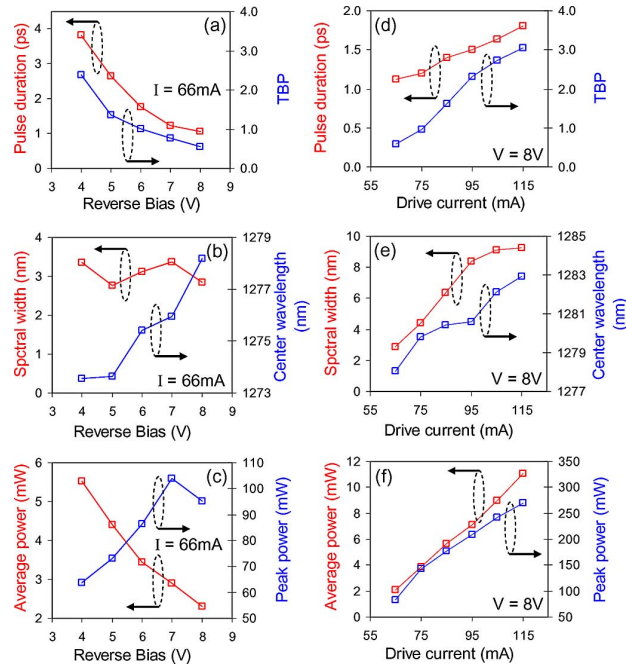
In the same paper some relevant considerations concerning the pulse width reduction and the enhancement of the output power are also proposed. Apart from the trivial approach consisting of a fine tuning of gain and absorber sections lengths, a solution relying on tapered waveguides is presented.

One of the first examples of possible application of PML semiconductor lasers based on QDs is reported in [87]. The microwave signal generated inside the ML device is extracted from its SA section, which behaves as a p-i-n photodetector: when an optical pulse travels this section, an electrical pulse is generated at the same repetition rate with a simple DC bias voltage. The proposed approach is then to integrate the monolithic laser diode with a reconfigurable fractal antenna as shown in Figure 3.17, acting as a compact RF signal generator.



(a) Gain and absorption spectra

(b) Mode locking regimes for different $L_{\text{gain}} : L_{\text{abs}}$ ratios



(c) Device characterization for fixed current and voltage values

Figure 3.16: Significant results reported by Thompson et al. [86].

Further details on the design procedure and device characterization can be found in the mentioned paper. In particular, the Authors highlight that the design strategy for microwave signal generation is different with respect to the one followed for obtaining short pulse trains with similar ML QD lasers: the optical power is not a concern in such applications, whereas here the electrical pulse extracted from the SA section should be maximized without impairing the ML regime stability.

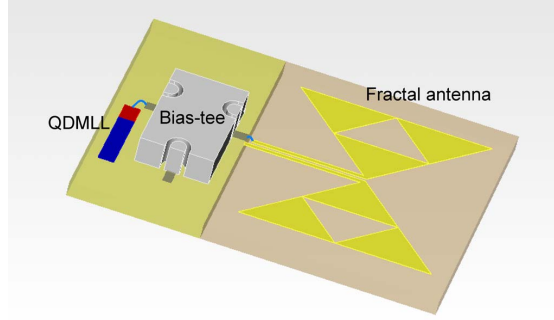


Figure 3.17: RF signal generator proposed by Lin et al. [87].

In order to improve the ML stability in two-section PML lasers, the insertion of an external optical feedback (i.e. an additional cavity, Figure 3.18a) has been proposed theoretically in [88] and verified in [89]. In the latter, a device based on a six-stack InAs QD active region emitting at $\lambda_{GS} = 1330$ nm is characterized in terms of RF linewidth both with and without the presence of an external fiber loop providing optical stabilization. Figure 3.18b shows that the presence of this feedback mechanism leads to a much narrower RF linewidth (reduced from 8 kHz to 350 Hz), and this is paid in terms of complexity, size and final repetition rate.

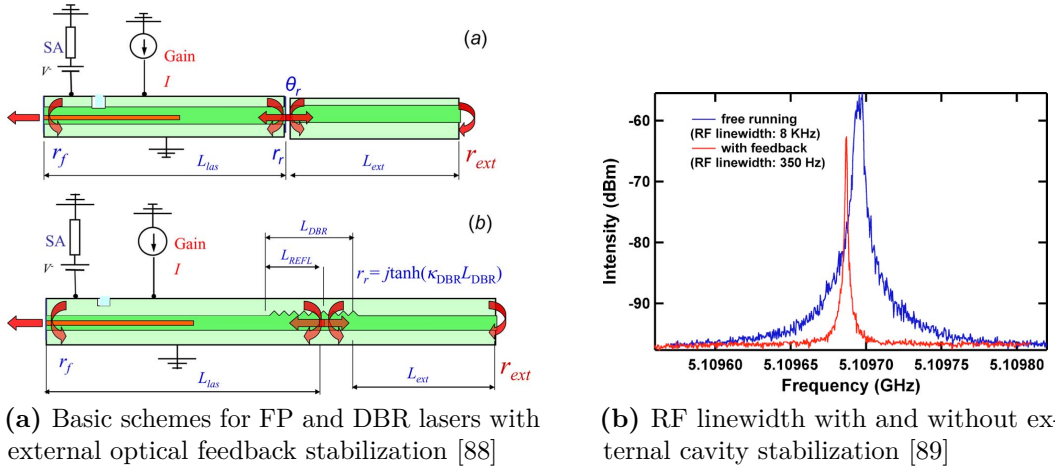
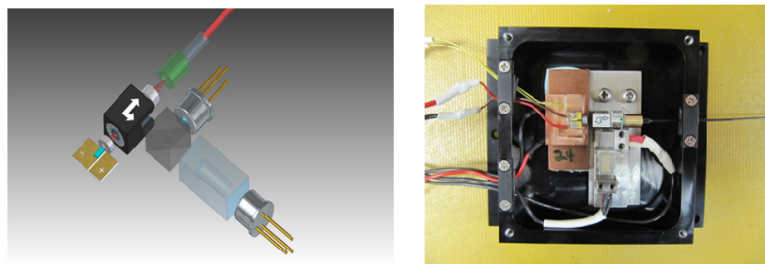


Figure 3.18: External optical feedback insertion to improve ML stability.

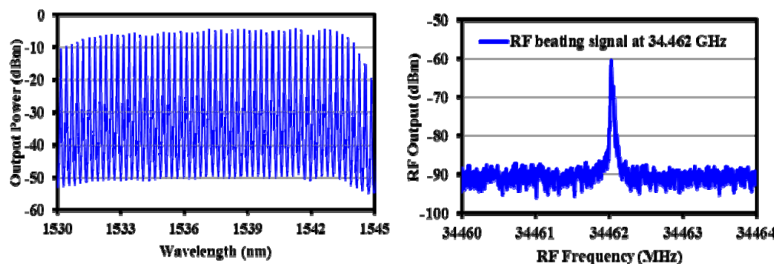
Latest achievements

More recently, a growing interest towards self-generated frequency combs has been developing, in particular for their application in data centers, Ethernet networks and coherent communications systems. An InAs/InP QD SML laser operating in the C-band (around 1.5 μm) with a fundamental repetition rate $f_R = 34.462$ GHz has been proposed in [90], representing a cheap but effective solution for coherent networking systems using the data format 16-QAM at the data rate of 28 Gbps.

In the proposed configuration, the laser source (with a 1.225 mm long cavity) and the control logic are embedded into an optical fiber pigtailed solution, as reported in Figure 3.19a. Apart from the characterization in terms of average output power ($P_{\text{avg}} = 43$ mW) and autocorrelation pulse width ($\Delta\tau = 29$ ps), the most interesting result has been obtained in terms of -3 dB optical spectrum bandwidth, equal to 12 nm and providing 45 channels with a signal-to-noise ratio over 40 dB (Figure 3.19b). Additional details on the proposed system have also been provided by the same authors in [91].



(a) Optical schematic and pigtailed implementation

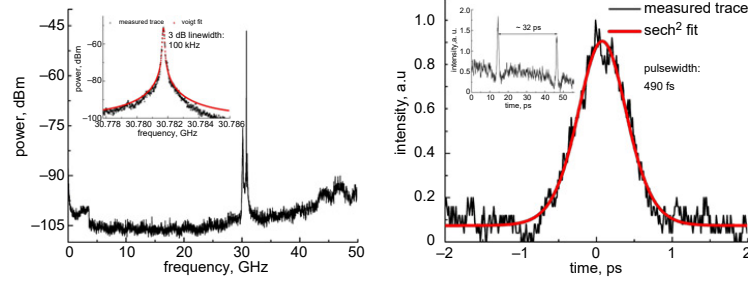


(b) RF linewidth with and without external cavity stabilization

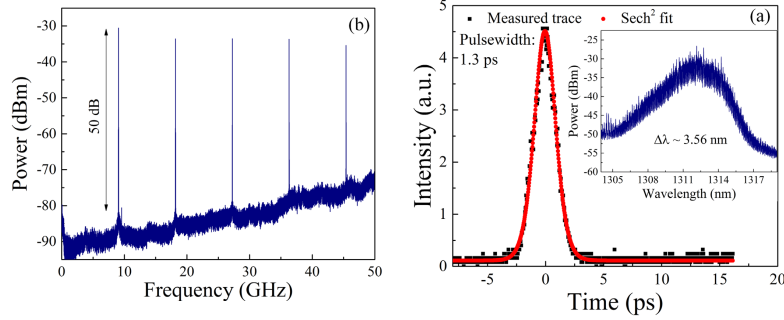
Figure 3.19: Optical setup and spectral results reported in [90].

Many research efforts have lately been aimed at Silicon Photonics (SiP) solutions, a fertile and promising field allowing to integrate photonic devices onto electronic chips. Optical pulses generation from PML single-section lasers directly grown on Ga/Si substrates has been investigated in [92], with a device operating at $f_R = 31$ GHz delivering pulse widths as low as $\Delta\tau = 490$ fs (Figure 3.20a).

The same research group has also proposed in [93] a monolithic 9 GHz PML QD laser diode grown on (100) Si, studying the effect of the SA-to-gain ratio in terms of threshold current and output power. The main results for a passive section length equal to 23% of the total cavity are reported in Figure 3.20b.



(a) Results for a gain current $I = 470$ mA reported in [92]



(b) Results with $L_{\text{abs}} : L = 0.23$, $I = 146$ mA reported in [93]

Figure 3.20: RF spectrum and pulse width results for devices with Si substrate.

Further contributions can be found in the literature, aimed at a more complete characterization of ML laser diodes to be included in Telecommunications applications. The main parameters considered in order to describe the device behavior in an application-oriented scenario are: threshold current, noise, RF spectrum [94, 95], temperature working range [96], linewidth enhancement factor [97]. Concerning CML, [98] reports a thorough characterization in terms of power and comb efficiency, whereas an example of simulation and some details on the adopted mathematical model are provided in [99]. Finally, the spectral performances obtained when increasing the number of stacked QD layers are shown in [100].

Final considerations

The proposed state of the art analysis is not meant to represent a complete description of the literature concerning QD-based laser diodes in ML condition,

since such a work would represent quite an intensive effort given the abundance of material concerning this topic. However, the examples presented before should provide an overall view of the fast and partially unexpected progress that these devices have undergone, mainly due to the strong improvements in the fabrication of nanometric features in semiconductor technology during the last 20 years.

From a practical perspective, the main parameters that could be used in the design of a Telecommunications system based on QD ML lasers have been extracted from the proposed articles. A comprehensive summary of them is presented in Table 3.1, which may represent a useful tool to compare different technological choices and implementations in terms of the aforementioned key performance indicators considering the final target application.

Ref.	Year	ML type	λ (μm)	f_R (GHz)	$\Delta\tau$ (ps)	P_{max} (mW)
[74]	2001	P	1.3	7.4	17	–
[75]	2003	P, H	1.1	10	< 14	4
[76]	2004	P	1.3	18	10	2.5
[77]	2005	P	1.3	21	< 2	1100
[79]	2005	P	1.3	5.2	5.7	290
[80]	2005	P	1.3	5	$(3.2 \div 7)$	< 1700
[56]	2006	P, H	1.3	$(20 \div 80)$	$(0.5 \div 2)$	–
[81]	2005	C	1.1	10×2	7	–
[82]	2007	P, H	1.3	40	2	–
[83]	2008	S	1.5	92.5	< 1	–
[84]	2008	S	1.5	45	0.312	–
[85]	2009	S	1.5	46	0.445	–
[86]	2009	P	1.3	20	1	105
[87]	2009	P	1.2	10	10	–
[89]	2010	P	1.3	5.1	–	–
[90]	2018	S	1.5	34	29	–
[92]	2018	P	1.3	31	0.49	40
[93]	2018	P	1.3	< 9	1.3	–
[94]	2019	P	1.3	20	< 12	–
[96]	2020	P	1.3	25.5	< 9	–
[95]	2021	P	1.5	23.5	–	–
[97]	2021	P	1.3	20	–	–
[100]	2021	P	1.3	81	< 1.85	–
[98]	2022	C	1.3	60	–	–
[99]	2022	C	1.3	80	–	< 10

Table 3.1: Main parameters extracted from the state of the art analysis.

3.4 Light propagation in QD waveguides

In order to study the behavior of pulses traveling along the laser cavity, a brief review of the electromagnetic field propagation in an optical waveguide is proposed, since constituting the basis for the following analysis. Then, the results obtained in Chapter 2 concerning the physical description of QD active materials are exploited to analyze the field evolution in waveguides relying on reduced dimensionality structures.

3.4.1 Traveling wave equations

The description of an electromagnetic field propagating in an active optical waveguide relies on **Maxwell equations** for the electric (\mathbf{E}) and magnetic (\mathbf{H}) fields in the frequency domain:

$$\begin{cases} \nabla \times \mathbf{E} = -j\omega\mu_0\mathbf{H} \\ \nabla \times \mathbf{H} = j\omega\epsilon_0\epsilon_r(\omega, \mathbf{r})\mathbf{E} + j\omega\mathbf{P}(\omega, \mathbf{r}) + \mathbf{J}(\omega, \mathbf{r}) \end{cases} \quad (3.11)$$

- $\mu_0 = 4\pi \times 10^{-7} \text{ H m}^{-1}$ is the magnetic permeability of the vacuum.
- $\epsilon_0 = 8.84 \times 10^{-12} \text{ F m}^{-1}$ is the vacuum permittivity.
- $\epsilon_r = \epsilon_r(\omega, \mathbf{r})$ is the space- and frequency-dependent background dielectric constant of the semiconductor medium, and in particular it varies along the transverse directions (x, y) of the waveguide providing the optical confinement.
- \mathbf{P} is the additional polarization induced by the semiconductor active medium, which can be related to the electric field through the electronic susceptibility as $\mathbf{P}(\omega, \mathbf{r}) = \epsilon_0\chi(\omega, \mathbf{r})\mathbf{E}(\omega, \mathbf{r})$ in the case of a linear² material response.
- \mathbf{J} is an additional stochastic current density modeling the spontaneous emission noise from the active medium.

Each vector quantity can be expressed with its longitudinal (subscript z , indicating the propagation direction) and transverse (subscript t) component as

$$\mathbf{A} = \mathbf{A}_t + A_z\hat{z} \quad \mathbf{A} = \mathbf{E}, \mathbf{H}, \mathbf{P}, \mathbf{J}. \quad (3.12)$$

²In general, the susceptibility $\chi(\omega, \mathbf{r})$ is a non-diagonal matrix, accounting for possible anisotropy in the optical response of the semiconductor medium.

In this way, Maxwell equations can be rewritten in terms of transverse components of the electric and magnetic field, obtaining the Marcuvitz-Schwinger [101] equations:

$$\begin{cases} \frac{\partial \mathbf{E}_t}{\partial z} = j\omega\mu_0 \left[\mathbf{1} + \frac{c^2}{\omega^2} \nabla_t \frac{1}{\epsilon_r} \nabla_t \right] (\mathbf{H}_t \times \hat{z}) - \nabla_t \left(\frac{P_z}{\epsilon_0 \epsilon_r} \right) - \nabla_t \left(\frac{J_z}{j\omega \epsilon_0 \epsilon_r} \right) \\ \frac{\partial \mathbf{H}_t}{\partial z} = j\omega \epsilon_0 \epsilon_r \left[\epsilon_r \mathbf{1} + \frac{c^2}{\omega^2} \nabla_t \nabla_t \right] (\hat{z} \times \mathbf{E}_t) + j\omega (\hat{z} \times \mathbf{P}_t) + \hat{z} \times \mathbf{J}_t \end{cases} \quad (3.13)$$

The longitudinal components of the two fields can then be obtained as:

$$\begin{cases} j\omega \epsilon_0 \epsilon_r E_z = \nabla_t (\mathbf{H}_t \times \hat{z}) \\ j\omega \mu_0 H_z = \nabla_t (\hat{z} \times \mathbf{E}_t) \end{cases} \quad (3.14)$$

Equation 3.13 and Equation 3.14 are fully equivalent to Maxwell equations (Equation 3.11). However, for a ridge waveguide as the one presented in Figure 3.6, the analytical solution of these equations cannot be obtained, unless a set of assumptions and approximations is introduced.

1. Marcuvitz-Schwinger homogeneous equations (i.e. with $\mathbf{P} = 0$, $\mathbf{J} = 0$) are solved at first, in order to determine the characteristic eigenmodes of the system.
 - (a) Considering the piecewise constant value of $\epsilon_r = \epsilon_r(\omega, \mathbf{r})$ along the transverse direction, two scalar Helmholtz equations are obtained and they can be solved by enforcing proper boundary conditions (mainly continuity conditions) at the interfaces between different materials.
 - (b) In the case of slab waveguides, ideal planar devices with no lateral confinement, the solution consists of a set of orthogonal modes, namely Transverse Electric (TE) and Transverse Magnetic (TM) ones, obtained analytically since the two Helmholtz equations are uncoupled.
 - (c) This is no longer true in ridge waveguides, but an analytical solution can still be obtained by introducing the quasi-TE and quasi-TM modes, i.e. assuming that the longitudinal magnetic or electric field component is negligible with respect to the transverse one: this approximation can be considered valid in multi-layered dielectric structures as the one taken as a reference for this study.
2. The complete Marcuvitz-Schwinger equations can then be solved exploiting the transverse modes obtained before and including two further approximations.
 - (a) The additional polarization induced by the semiconductor is usually negligible with respect to the background dielectric polarization, hence this term is treated as a perturbation.

- (b) Dipole moments related to the interband optical transitions in Quantum Dots are negligible in the growth direction, meaning that both the additional polarization and the spontaneous emission along the x axis can be considered null ($P_x \approx 0$, $J_x \approx 0$). In this way, the optical susceptibility is simplified as

$$\underline{\underline{\chi}}(\omega, \mathbf{r}) \approx \chi(\omega, x, y, z) \begin{pmatrix} 0 & 0 & 0 \\ 0 & 1 & 0 \\ 0 & 0 & 1 \end{pmatrix}. \quad (3.15)$$

3. The optical power flow along the propagation direction z carried out by quasi-TE and quasi-TM modes determined previously can be evaluated from the z component of the Poynting vector, defined as the vector product between electric and magnetic fields in the waveguide. The instantaneous power can then be obtained by integrating along the transverse direction:

$$S(t, z) = \frac{1}{2} \operatorname{Re} \left\{ \iint (\mathbf{E}_t \times \mathbf{H}_t^*) \cdot \hat{z} \, dx \, dy \right\}. \quad (3.16)$$

From this relation, the mode amplitudes for guided modes can be obtained, and since no terms related to the Quantum Dot optical response appear in the equations for quasi-TM modes amplitude, it can be concluded that QDs mainly interact with TE polarized fields as observed in [30, 31].

4. In order to further simplify the final equation for the modes amplitudes, the *slowly-varying envelope approximation* is finally introduced by considering that the second order derivative of the field in the longitudinal direction is much lower than the first order one, i.e.

$$\left| \frac{\partial^2}{\partial z^2} \right| \ll \left| \frac{\partial}{\partial z} \right|. \quad (3.17)$$

The field amplitude in time domain can then be expressed in terms of forward- (V^+) and backward-propagating (V^-), slowly-varying components:

$$V(z, t) = \sqrt{2 \frac{\omega_0 \mu_0}{\beta_0}} \left[V^+(z, t) e^{-j\beta_0 z} + V^-(z, t) e^{+j\beta_0 z} \right] e^{-j\omega_0 t}, \quad (3.18)$$

where ω_0 is the reference frequency and $\beta_0 = \beta(\omega_0)$ is the corresponding propagation constant.

The outcome of the presented sequence of approximations is a simplified form of the **traveling wave equations**, which consists of two independent, first order time domain equations for the forward- and backward-propagating amplitudes:

$$\pm \frac{\partial V^\pm(z, t)}{\partial z} + \frac{1}{v_{g,0}} \frac{\partial V^\pm(z, t)}{\partial t} = -\frac{\alpha_i}{2} V^\pm(z, t) - j \frac{\omega_0}{2c\epsilon_0 n_{r,0}} \Gamma_{xy} P^\pm(z, t) + F^\pm(z, t). \quad (3.19)$$

Equation 3.19 is valid at frequency $\omega = \omega_0$, hence the frequency-dependent terms are denoted with a subscript 0. In particular, the refractive index has been introduced here, defined as

$$n_r = n_r(\omega) = \sqrt{\epsilon_r(\omega)} \implies n_{r,0} = n_r(\omega_0). \quad (3.20)$$

The group velocity is linked to this quantity through the following relationship:

$$\frac{1}{v_g} = \frac{n_r}{c} \left(1 + \frac{\omega}{n_r} \frac{\partial n_r}{\partial \omega} \right) \implies v_{g,0} = \left[\frac{n_{r,0}}{c} \left(1 + \frac{\omega_0}{n_{r,0}} \frac{\partial n_r}{\partial \omega} \Big|_{\omega=\omega_0} \right) \right]^{-1}. \quad (3.21)$$

The speed of light in vacuum c , the dielectric permittivity ϵ_0 and the intrinsic waveguide losses α_i are constant term, the latter taking into account additional losses in the device due to doped regions, contacts or unwanted defects. Conversely, the forward and backward polarization P^\pm and spontaneous emission noise F^\pm are assumed to be slowly-varying in time along the propagation direction z , i.e. they change on a time scale much longer than the optical cycle $T_R = 2\pi/\omega_0$.

Notice that Equation 3.19 requires a set of boundary conditions to be solved, which in the case of a Fabry-Pérot cavity is given by the continuity equations at the two facets. Indicating the two power reflectivities as $R(z = 0) = R_0$ and $R(z = L) = R_L$, it is sufficient to impose for the field:

$$\begin{cases} V^+(z = 0, t) = \sqrt{R_0} V^-(z = 0, t) \\ V^+(z = L, t) = \sqrt{R_L} V^-(z = L, t) \end{cases}. \quad (3.22)$$

Equivalently, the instantaneous optical power (Poynting vector) can be expressed in terms of mode amplitudes as the superposition of the two propagating and counter-propagating waves:

$$S(z, t) = S^+(z, t) - S^-(z, t) = |V^+(z, t)|^2 - |V^-(z, t)|^2. \quad (3.23)$$

Boundary conditions then become:

$$\begin{cases} S^+(z = 0, t) = R_0 S^-(z = 0, t) \\ S^+(z = L, t) = R_L S^-(z = L, t) \end{cases}. \quad (3.24)$$

3.4.2 Waveguide theory and density matrix dynamics

The dynamic behavior of the microscopic interband polarization for a QD material depends on the local electric field $\mathbf{E}(t)$, assumed to be independent of the spatial coordinates in Chapter 2 since its wavelength (around $1 \mu\text{m}$) is much longer than the characteristic dot dimensions. When considering a complete waveguide device,

though, such dependence cannot be ignored, and the electric field is in general a function of both space and time $\mathbf{E}(x, y, z, t)$.

Following the procedure presented in this Section, the dependence on the transverse coordinates (x, y) can be eliminated by considering the wave equations projected on the TE mode. In addition to this, the slowly-varying envelope approximation allows to obtain a simple form for the electric field, expressed in terms of forward- and backward-propagating components in Equation 3.18. A *slowly-varying polarization* can be written in a similar form by projecting the microscopic polarization on the TE transverse direction, considering again the pure states notation for the sake of simplicity:

$$\iint p_{\mathbf{k}}(x, y, z, t) \cdot e_y(x, y) dx dy = \sqrt{2 \frac{\omega_0 \mu_0}{\beta_0}} \left[p_{\mathbf{k}}^+(z, t) e^{-j\beta_0 z} + p_{\mathbf{k}}^-(z, t) e^{+j\beta_0 z} \right] e^{j\omega_0 t}. \quad (3.25)$$

The macroscopic polarization induced by the QD ensemble can be determined as the expected value of the electric dipole moment per unit volume. In order to relate it to the microscopic interband polarization evaluated previously, the following density matrix property is exploited:

$$\langle \mathbf{d} \rangle = \text{tr} [\rho \mathbf{d}] = \text{tr} [-\mathbf{d} \rho], \quad (3.26)$$

where $\langle \mathbf{d} \rangle$ is the expected value of the electric dipole moment and tr represents the trace³ operator. The macroscopic polarization can then be written as

$$\mathbf{P}(t) = \frac{1}{V_{\text{QD}}} \text{tr} [-\mathbf{d} \rho] = \sum_{\mathbf{k}} \frac{D_{\mathbf{k}} N_{\text{D}}}{h_{\text{QD}}} \left[\mathbf{d}_{\text{e,h}}^*(\mathbf{k}) p_{\mathbf{k}}(x, y, z, t) - \mathbf{d}_{\text{e,h}}(\mathbf{k}) p_{\mathbf{k}}^*(x, y, z, t) \right], \quad (3.27)$$

where $V_{\text{QD}} = N_{\text{D}}/h_{\text{QD}}$ is the dot volume and the factor $D_{\mathbf{k}}$ takes into account the spin degeneracy. Exploiting the slowly-varying polarization defined previously, the macroscopic forward- and backward-propagating terms appearing in Equation 3.19 are therefore:

$$\Gamma_{xy} P^{\pm}(z, t) = \Gamma_{xy} \sum_{\mathbf{k}} \frac{D_{\mathbf{k}} N_{\text{D}}}{h_{\text{QD}}} (\mathbf{d}_{\text{e,h}}^*(\mathbf{k}) \cdot \hat{y}) p_{\mathbf{k}}^{\pm}(z, t), \quad (3.28)$$

where the scalar product $\mathbf{d}_{\text{e,h}}^*(\mathbf{k}) \cdot \hat{y}$ gives the y component of the dipole matrix element. Concerning the dynamic behavior of the slowly-varying polarization, the following relation can be obtained by integrating Equation 2.63 over the transverse coordinates (x, y) :

$$\begin{aligned} \frac{\partial}{\partial t} p_{\mathbf{k}}^{\pm}(z, t) = & - \left[j(\varepsilon_{\text{e,k}} - \varepsilon_{\text{h,k}} - \omega_0) + \gamma_p \right] p_{\mathbf{k}}^{\pm}(z, t) + \\ & - \frac{j}{\hbar} \Gamma_{xy} (\mathbf{d}_{\text{e,h}}^*(\mathbf{k}) \cdot \hat{y}) \left[f_{\text{e,k}}(z, t) + f_{\text{h,k}}(z, t) - 1 \right] V^{\pm}(z, t). \end{aligned} \quad (3.29)$$

³This corresponds to performing a sum over the diagonal elements.

This equation allows to establish a direct relation between the QD optical response and the traveling wave equations describing the field propagation along the waveguide. The optical confinement factor Γ_{xy} describes the incomplete overlap between the TE mode and the stacked QD layers, whereas the characteristic interband transition frequency $\varepsilon_{e,\mathbf{k}} - \varepsilon_{h,\mathbf{k}}$ is now shifted by the reference frequency ω_0 , introduced in the slowly-varying approximation.

3.4.3 Quantum Dot susceptibility

The polarization dynamics represents the starting point to analyze the spectral behavior of a QD ML laser, describing the physical phenomena at the basis of the model. The Fourier transform of Equation 3.29 can be computed:

$$\begin{aligned} p_{\mathbf{k}}^{\pm}(z, \Omega) &= -\frac{1}{j[\Omega - (\varepsilon_{e,\mathbf{k}} - \varepsilon_{h,\mathbf{k}} - \omega_0) + \Gamma]} \frac{j}{\hbar} \Gamma_{xy} (\mathbf{d}_{e,h}^*(\mathbf{k}) \cdot \hat{y}) \times \\ &\quad \times \left\{ [f_{e,\mathbf{k}}(z, \Omega) + f_{h,\mathbf{k}}(z, \Omega) - 1] \otimes V^{\pm}(z, \Omega) \right\} = \\ &= \frac{j}{\hbar \Gamma} \mathcal{L}_{\mathbf{k}}(\Omega) (\mathbf{d}_{e,h}(\mathbf{k}) \cdot \hat{y}) \left\{ [f_{e,\mathbf{k}}(z, \Omega) + f_{h,\mathbf{k}}(z, \Omega) - 1] \otimes V^{\pm}(z, \Omega) \right\}, \end{aligned} \quad (3.30)$$

where Ω is the Fourier frequency and Γ is called the *dephasing time* of the microscopic polarization. A complex Lorentzian function with FWHM 2Γ and centered in $\varepsilon_{e,\mathbf{k}} - \varepsilon_{h,\mathbf{k}} - \omega_0$ has been introduced, defined as

$$\mathcal{L}_{\mathbf{k}}(\Omega) = \frac{1}{1 + j \frac{\Omega - (\varepsilon_{e,\mathbf{k}} - \varepsilon_{h,\mathbf{k}} - \omega_0)}{\Gamma}}. \quad (3.31)$$

The impulse response of such function in the time domain is

$$\mathcal{L}_{\mathbf{k}}(t) = \Gamma e^{j(\varepsilon_{e,\mathbf{k}} - \varepsilon_{h,\mathbf{k}} - \omega_0)t} e^{-\Gamma t}. \quad (3.32)$$

The macroscopic forward- and backward-propagating polarization, expressed as functions of the microscopic one in Equation 3.28, can therefore be rewritten in the frequency domain as

$$\begin{aligned} \Gamma_{xy} P^{\pm}(z, \Omega) &= \Gamma_{xy} \sum_{\mathbf{k}} \frac{D_{\mathbf{k}} N_{\text{D}}}{h_{\text{QD}}} \frac{j}{\hbar \Gamma} \mathcal{L}_{\mathbf{k}}(\Omega) (|\mathbf{d}_{e,h}(\mathbf{k}) \cdot \hat{y}|^2) \times \\ &\quad \times \left\{ [f_{e,\mathbf{k}}(z, \Omega) + f_{h,\mathbf{k}}(z, \Omega) - 1] \otimes V^{\pm}(z, \Omega) \right\}. \end{aligned} \quad (3.33)$$

Equivalently, the time domain relation is obtained by anti-transforming the frequency domain one:

$$\begin{aligned} \Gamma_{xy}P^\pm(z, t) &= \Gamma_{xy} \sum_{\mathbf{k}} \frac{D_{\mathbf{k}}N_{\text{D}}}{h_{\text{QD}}} \frac{j}{\hbar\Gamma} \left(|\mathbf{d}_{\text{e,h}}(\mathbf{k}) \cdot \hat{y}|^2 \right) \times \\ &\times \mathcal{L}_{\mathbf{k}}(t) \otimes \left\{ [f_{\text{e,k}}(z, t) + f_{\text{h,k}}(z, t) - 1] V^\pm(z, t) \right\}, \end{aligned} \quad (3.34)$$

where the convolution product is given by

$$\begin{aligned} \mathcal{L}_{\mathbf{k}}(t) \otimes \left\{ [f_{\text{e,k}}(z, \Omega) + f_{\text{h,k}}(z, \Omega) - 1] V^\pm(z, \Omega) \right\} &= \\ = \Gamma \int_{-\infty}^t e^{j(\varepsilon_{\text{e,k}} - \varepsilon_{\text{h,k}} - \omega_0)(t-\tau)} e^{-\Gamma(t-\tau)} [f_{\text{e,k}}(z, \tau) + f_{\text{h,k}}(z, \tau) - 1] V^\pm(z, \tau) d\tau. \end{aligned} \quad (3.35)$$

In order to simplify the previous relation, the **adiabatic approximation** is introduced. This consists in assuming a fast decaying time for the exponential term $e^{-\Gamma(t-\tau)}$ when $\tau \rightarrow -\infty$, meaning that the polarization value at time t only depends on the past evolution of occupation probabilities $f_{\lambda,\mathbf{k}}(z, t)$ and field $V^\pm(z, t)$ in a short time interval given by the characteristic dephasing rate $1/\Gamma \approx 100$ fs. In other words, the system has a memory limited to few hundreds of fs, and since the occupation probabilities evolve on a much longer time scale they can be moved out of the integral. Such assumption cannot be considered in general for the forward- and backward-propagating fields, hence the simplified macroscopic polarization relation yields

$$\begin{aligned} \Gamma_{xy}P^\pm(z, t) &= \Gamma_{xy} \sum_{\mathbf{k}} \frac{D_{\mathbf{k}}N_{\text{D}}}{h_{\text{QD}}} \frac{j}{\hbar\Gamma} \left(|\mathbf{d}_{\text{e,h}}(\mathbf{k}) \cdot \hat{y}|^2 \right) \times \\ &\times [f_{\text{e,k}}(z, t) + f_{\text{h,k}}(z, t) - 1] \left\{ \mathcal{L}_{\mathbf{k}}(t) \otimes V^\pm(z, t) \right\}. \end{aligned} \quad (3.36)$$

The slowly-varying traveling polarization terms appearing in the wave equations can also be defined as

$$\epsilon_0 \bar{\chi}(z, t) \otimes V^\pm(z, t) = \epsilon_0 \int_{-\infty}^t \bar{\chi}(z, t - \tau) V^\pm(z, \tau) d\tau, \quad (3.37)$$

where the traveling susceptibility is given by

$$\bar{\chi}(z, t) = \chi(z, t) e^{-j\omega_0 t}. \quad (3.38)$$

In the time domain, the following expression relating the susceptibility to the Quantum Dot properties can be derived from the results obtained within the adiabatic approximation:

$$\bar{\chi}(z, t) = \frac{1}{\epsilon_0} \sum_{\mathbf{k}} \frac{D_{\mathbf{k}}N_{\text{D}}}{h_{\text{QD}}} \frac{j}{\hbar\Gamma} \left(|\mathbf{d}_{\text{e,h}}(\mathbf{k}) \cdot \hat{y}|^2 \right) [f_{\text{e,k}}(z, t) + f_{\text{h,k}}(z, t) - 1] \mathcal{L}_{\mathbf{k}}(t). \quad (3.39)$$

Moving to the frequency domain, the time dependence remains due to the presence of the occupation probabilities outside of the convolution integral in the adiabatic approximation:

$$\bar{\chi}(z, t, \Omega) = \frac{1}{\epsilon_0} \sum_{\mathbf{k}} \frac{D_{\mathbf{k}} N_D}{h_{\text{QD}}} \frac{j}{\hbar \Gamma} \left(|\mathbf{d}_{e,h}(\mathbf{k}) \cdot \hat{y}|^2 \right) [f_{e,\mathbf{k}}(z, t) + f_{h,\mathbf{k}}(z, t) - 1] \mathcal{L}_{\mathbf{k}}(t, \Omega). \quad (3.40)$$

This result can be used in the following to analyze some additional phenomena that can be described using the MS-DDE model.

Gain and refractive index spectra

The optical response of a QD active medium consists of an amplification (or attenuation) term and a corresponding phase change induced by the incoming electromagnetic radiation. The gain spectrum can be obtained from the imaginary part of the QD susceptibility as

$$\begin{aligned} g(z, t, \Omega) &= \frac{\omega_0}{c n_{r,0}} \text{Im} \{ \bar{\chi}(z, t, \Omega) \} = \\ &= \sum_{\mathbf{k}} g_{0,\mathbf{k}} [f_{e,\mathbf{k}}(z, t) + f_{h,\mathbf{k}}(z, t) - 1] \text{Re} \{ \mathcal{L}_{\mathbf{k}}(t, \Omega) \}, \end{aligned} \quad (3.41)$$

where the *characteristic gain* $g_{0,\mathbf{k}}$ has been defined as

$$g_{0,\mathbf{k}} = \frac{\omega_0}{c n_{r,0}} \frac{1}{\epsilon_0} \frac{D_{\mathbf{k}} N_D}{h_{\text{QD}}} \frac{1}{\hbar \Gamma} \left(|\mathbf{d}_{e,h}(\mathbf{k}) \cdot \hat{y}|^2 \right). \quad (3.42)$$

Similarly, the refractive index change spectrum is given by

$$\begin{aligned} \Delta n_r(z, t, \Omega) &= \frac{1}{2n_{r,0}} \text{Re} \{ \bar{\chi}(z, t, \Omega) \} = \\ &= \sum_{\mathbf{k}} \frac{c}{\omega_0} g_{0,\mathbf{k}} [f_{e,\mathbf{k}}(z, t) + f_{h,\mathbf{k}}(z, t) - 1] \text{Im} \{ \mathcal{L}_{\mathbf{k}}(t, \Omega) \}. \end{aligned} \quad (3.43)$$

Notice, however, that the effect of the electromagnetic field is not limited to interband transitions between electron and hole confined states in the QD material. When the carrier densities in the active region are sufficiently large, additional contributions to absorption and refractive index spectra must be considered, caused by intraband transitions involving electron and hole plasmas within WL and SCH levels. An additional phenomenological loss term can be introduced in the traveling wave equations, proportional to these carrier densities [102]:

$$\alpha^{\text{pl}} = \Gamma_{xy} \sum_{\lambda} k_{\lambda,\text{WL}}^{\text{pl}} \frac{n_{\lambda,\text{WL}}}{h_{\text{WL}} N_{\text{I}} W} + \Gamma_{xy} \sum_{\lambda} k_{\lambda,\text{SCH}}^{\text{pl}} \frac{n_{\lambda,\text{SCH}}}{h_{\text{SCH}} W}, \quad (3.44)$$

where $k_{\lambda,\text{WL}}^{\text{pl}}$ and $k_{\lambda,\text{SCH}}^{\text{pl}}$ are characteristic free carrier absorption coefficients, measured in cm^2 . Similarly, refractive index changes due to the same plasma phenomena are modeled as [103]

$$\Delta n_r^{\text{pl}} = \Gamma_{xy} \sum_{\lambda} K_{\lambda,\text{WL}}^{\text{pl}} \frac{n_{\lambda,\text{WL}}}{h_{\text{WL}} N_1 W} + \Gamma_{xy} \sum_{\lambda} K_{\lambda,\text{SCH}}^{\text{pl}} \frac{n_{\lambda,\text{SCH}}}{h_{\text{SCH}} W}. \quad (3.45)$$

The coefficients $K_{\lambda,\text{WL}}^{\text{pl}}$ and $K_{\lambda,\text{SCH}}^{\text{pl}}$ describe the dependence of the refractive index changes with respect to the WL and SCH carrier densities, and they can be obtained according to the Drude formula for the optical response of a free plasma:

$$K_{\lambda,\text{WL}}^{\text{pl}}(\omega) = -\frac{q^2}{2\epsilon_0 n_{r,0} m_{\text{WL}}^* \omega^2}, \quad K_{\lambda,\text{SCH}}^{\text{pl}}(\omega) = -\frac{q^2}{2\epsilon_0 n_{r,0} m_{\text{SCH}}^* \omega^2}, \quad (3.46)$$

where ω is the EM field frequency.

Stimulated emission rate

The stimulated emission rate from each QD state introduced in Section 2.2 can be computed starting from the microscopic polarization (satisfying Equation 2.63):

$$R_{\mathbf{k}}^{\text{st}} = -\frac{1}{\hbar} \frac{D_{\mathbf{k}} N_{\text{D}}}{h_{\text{QD}}} \frac{1}{c n_{r,0} \epsilon_0} \text{Im} \left\{ \left(\mathbf{d}_{\text{e,h}}(\mathbf{k}) \cdot \hat{\mathbf{y}} \right) p_{\mathbf{k}}^{*+}(z, t) V^+(z, t) + \left(\mathbf{d}_{\text{e,h}}(\mathbf{k}) \cdot \hat{\mathbf{y}} \right) p_{\mathbf{k}}^{*-}(z, t) V^-(z, t) \right\}. \quad (3.47)$$

The dependence with respect to the polarization terms can then be eliminated by substituting the relation derived within the adiabatic approximation, obtaining

$$R_{\mathbf{k}}^{\text{st}} = \frac{1}{\hbar} \frac{g_{0,\mathbf{k}}}{\omega_0} \left[f_{\text{e},\mathbf{k}}(z, t) + f_{\text{h},\mathbf{k}}(z, t) - 1 \right] \text{Re} \left\{ V^+(z, t) \left[\mathcal{L}_{\mathbf{k}}(\Omega) \otimes V^+(z, t) \right]^* + V^-(z, t) \left[\mathcal{L}_{\mathbf{k}}(\Omega) \otimes V^-(z, t) \right]^* \right\}. \quad (3.48)$$

This relation completes the set of rate equations required to fully describe the dynamic behavior of a QD-based laser diode derived with the density matrix approach.

Remarks on the inhomogeneous broadening

From the relations presented in this section, the filtering effect performed by the QD material on the electromagnetic field can be clearly seen. In particular, a Lorentzian filter is associated to an interband transition, weighted by the occupation probabilities and with a FWHM proportional to the dephasing rate of the microscopic polarization.

In the case of a QD ensemble, each of the N groups is characterized by a different interband transition energy, leading to a set of Lorentzian filters whose effect is broadened with respect to the individual ones. Such broadening mechanism of the optical interband transitions corresponds to the *homogeneous broadening* phenomenon introduced in Chapter 2, and it causes the gain spectral bandwidth to be much larger than the homogeneous linewidth of a single interband transition due to such superposition of effects.

3.4.4 Spontaneous emission noise

From a physical perspective, spontaneous emission is one of the major recombination processes occurring within QD layers. However, when considering semiconductor waveguides, this also represents a distributed source of electromagnetic field along the device appearing in the traveling wave equations: this comes from Maxwell equations, which include a current density source \mathbf{J} that leads to the term $F^\pm(z, t)$ in Equation 3.19.

Instead of following a rigorous approach to describe spontaneous emission in semiconductor devices, it is convenient to derive a relation for the spontaneously emitted power per unit length per unit bandwidth starting from the gain spectrum presented in Equation 3.41. Following Einstein approach as suggested in [44], it is possible to obtain:

$$\left|F^\pm(z, \Omega)\right|^2 = \frac{\beta^{\text{sp}}}{2} N_D W N_1 \sum_{\mathbf{k}} D_{\mathbf{k}} \frac{\Gamma \hbar (\varepsilon_{e,\mathbf{k}} - \varepsilon_{h,\mathbf{k}})}{\pi} R_{\mathbf{k}}^{\text{sp}}(z, t) \text{Re}\{\mathcal{L}_{\mathbf{k}}(\Omega)\}. \quad (3.49)$$

The spontaneous emission coupling factor β^{sp} takes into account the fact that only a small portion of the whole spontaneously emitted radiation couples with the TE mode of the optical waveguide. This fact could also be seen from Equation 3.11, in which the current density term has been projected in the transverse direction through an external product with the unit vector \hat{z} . Typical values for β^{sp} range from 10^{-3} to 10^{-4} , further divided by 2 assuming that propagating and counterpropagating spontaneously emitted waves are equally split in half.

Notice also that the spontaneous emission rate $R_{\mathbf{k}}^{\text{sp}}(z, t)$ appearing in the previous relation has been evaluated through a phenomenological characteristic time constant $\tau_{\mathbf{k}}^{\text{sp}}$ in Section 2.2, yielding

$$R_{\mathbf{k}}^{\text{sp}}(f_{e,\mathbf{k}}, f_{h,\mathbf{k}}) = \frac{1}{\tau_{\mathbf{k}}^{\text{sp}}} f_{e,\mathbf{k}} f_{h,\mathbf{k}}. \quad (3.50)$$

Exploiting again Einstein approach, a direct relation between this spontaneous emission time constant and the characteristic gain $g_{0,\mathbf{k}}$ defined in Equation 3.42 can be found:

$$\frac{1}{\tau_{\mathbf{k}}^{\text{sp}}} = \frac{h_{\text{QD}}}{N_D N_1 D_{\mathbf{k}}} \frac{n_{r,0}^2 (\varepsilon_{e,\mathbf{k}} - \varepsilon_{h,\mathbf{k}}) \Gamma}{\pi c^2} g_{0,\mathbf{k}}. \quad (3.51)$$

3.5 MS-DDE model

The mathematical model at the basis of the simulation activity performed in this Thesis is now introduced. At first, a rapid overview of alternative approaches for the analysis of QD ML laser diodes is provided. A more thorough analysis of the model applicability is then carried out for the two types of laser structures that can be simulated, namely the ring and the edge-emitting configurations.

3.5.1 Modeling mode-locked QD lasers

The description of passively mode-locked lasers relying on self-assembled QD active media can be carried out exploiting Time-Domain Traveling-Wave (TDTW) models, as the one proposed in [18]. Such approach consists in the solution via a finite difference scheme of the traveling wave equations presented before, hence it provides the most accurate and realistic simulation results. Moreover, these models can be applied to a quite wide range of devices, with several commercial simulators of laser diodes relying on them.

However, the main limitations of a traveling wave approach are related to its computational requirements, both in terms of time and memory. In this framework, time and space axes have to be discretized with steps Δt and Δz , respectively: these quantities have to be sufficiently small in order to accurately describe the electromagnetic radiation evolution in the device, and they are often linked to each other. As an example, the time step should be shorter than the time constant of the fastest physical phenomenon that has to be included in the model (usually below 1 ps), whereas a thorough description of the propagating and counter-propagating pulses along a laser diode cavity requires a fine spatial discretization in the longitudinal direction (in the order of few μm).

Another approach, still performed in the time domain but limited to a small-signal analysis, is the Self-Consistent Pulse profile model. This represents the very first attempt to model mode locking in semiconductor lasers, and it has been proposed in the pioneering works of New [104] and Haus [105]. It is based on the assumption that the traveling pulse width is much smaller than the repetition period T_R , alongside the presence of lumped elements that represent the gain and absorption sections of the device. Several studies have then pursued improved version of this model [106, 107], simple but quite limited in terms of applicability.

An alternative way for studying ML laser diodes relies on the *modal analysis* technique, which can be static or dynamic. In this case, a frequency domain approach is chosen as the one presented in [108]. However, such technique is less general with respect to the TDTW one, mainly due to some restrictive assumptions in terms of low non-linearity and the presence of two time scales (slow and fast).

Finally, a large-signal iterative model can represent a trade-off between accuracy and computational requirements. This is the case of the proposed Delayed Differential Equation model, which allows to overcome the complexity of a TDTW approach while maintaining the possibility to include physical phenomena occurring on a rather short time scale. A more detailed analysis of this approach, including a comparison with respect to previous DDE models proposed in the literature, is carried out in the following sections.

3.5.2 Multi-Section Delayed Differential Equation model description

Given the high complexity and computational requirements of the TDTW model, as well as the limitations that affect other approaches presented in the previous section, the proposed DDE model provides an alternative, computationally-efficient solution enabling parametric analyses of QD laser diodes in ML conditions.

The analytical models proposed by New and Haus [104, 105] represent the theoretical ground on which this approach is based. The original DDE model formulation has been presented in [109], with a generalization of the aforementioned works, whereas its application for QD ML lasers has been brought forward in [110]. Though conceived for the simulation of unidirectional ring lasers, the same approach has also been extensively applied to Fabry-Pérot devices [111–113], with a qualitative agreement in the results with respect to TDTW simulations [19, 114].

A detailed derivation of the model, carried out starting from the traveling wave equations described in Equation 3.19, can be found in [109] and it is omitted here. However, the assumptions on which such derivation is based are listed in the following in order to make a significant comparison with the approach presented in this Thesis.

1. Ring cavities with unidirectional lasing only are considered.
2. Such ring consists of two sections, i.e. gain and saturable absorber.
3. Lasing from the QD ground state only is assumed when analyzing Quantum Dot-based devices [110].
4. Intrinsic waveguide losses, denoted with α_i in the following, are modeled as a lumped loss term in the reference section $z = 0$ of the device, as well as the coupling losses.
5. The finite gain spectral bandwidth of the semiconductor material introduces a filtering effect which is also modeled as a lumped element in the reference section $z = 0$.

To sum up, in its original formulation the DDE model could be employed in the analysis of either one of the two simple structures reported in Figure 3.21. In the following, the gain region (with length L_{gain}) is associated to a green color, whereas red is used to identify SA sections (length L_{abs}). Clearly, the reference section $z = 0$ mentioned before coincides with the one reached at the end of a round trip, i.e. $z = L$. This is the only point at which the device can be fully characterized by exploiting this approach.

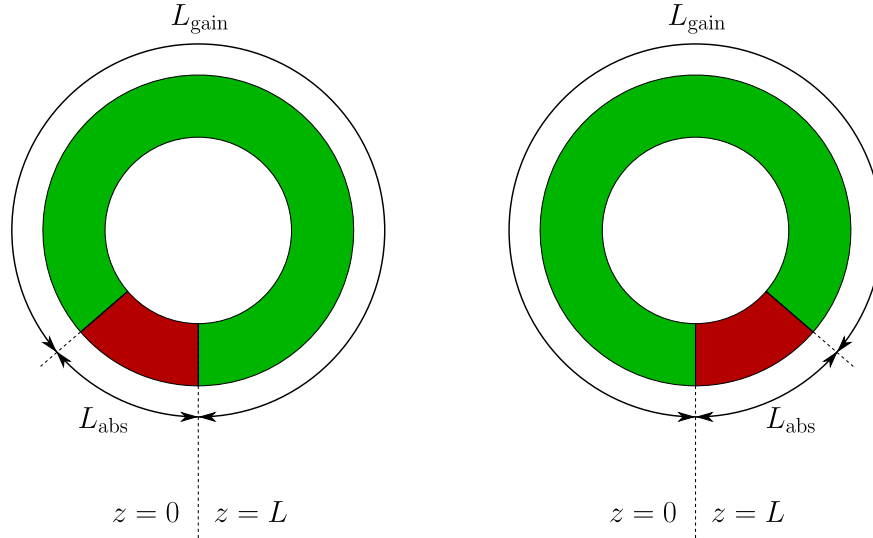


Figure 3.21: Ring structures correctly analyzed with the original DDE model formulation [109, 110].

The multi-section approach allows to lift the second assumption listed previously: the laser cavity is now assumed to be composed of an arbitrary number of electrically isolated sections that can be biased independently, thus adding the possibility of including many gain and/or SA section in the device. Moreover, a non-saturable loss term is introduced at the interface between each adjacent section, enabling a more accurate description of the intrinsic waveguide losses and granting the possibility to extract the internal signal at any of these interfaces (properly including the associated coupling losses). Hence, the fourth assumption introduced in the original model can be partially mitigated.

In addition to this, both ground and first excited state lasing can be treated with this generalized model, so that dual-wavelength devices can also be studied (assumption 3 extended to two energy levels). Finally, edge-emitting cavities are automatically converted into ring structures by considering the optical path inside the active material during a complete round trip: the coupling losses are associated to the power reflectivity of a facet, whereas the other one is modeled as a lumped loss

element localized at half the round trip. Notice, however, that the unidirectionality of the lasing mode is still assumed, as well as the presence of a lumped filtering effect at section $z = 0$ due to the finite material gain spectral bandwidth.

The simplest FP structure that can be analyzed with the MS-DDE approach is presented in Figure 3.22, which also shows the equivalent ring device corresponding to it. The main model elements are presented with references to this basic structure for the sake of simplicity, even though more complex devices can also be studied and will be presented in the following of this document.

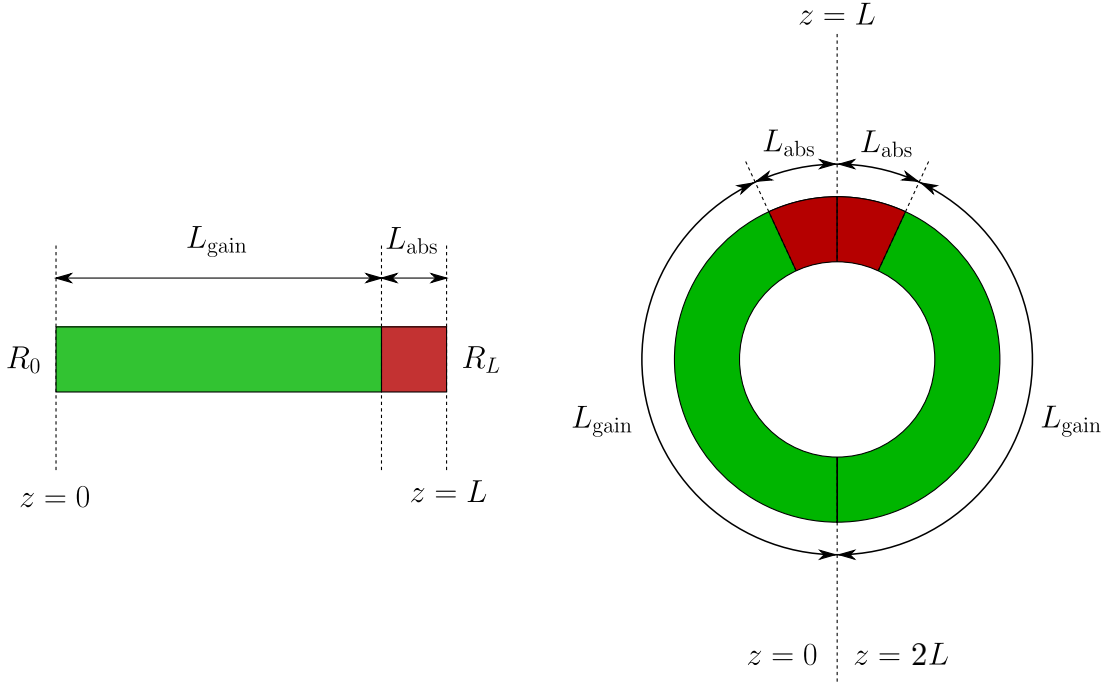


Figure 3.22: Basic FP and equivalent ring structures analyzed with the proposed MS-DDE model.

As stated before, the delayed differential equations governing the field evolution can be directly derived from the traveling wave ones (Equation 3.19). In particular, the following coordinate change in the time domain is introduced:

$$t \longrightarrow \tau = t - \frac{z}{v_g}, \quad (3.52)$$

where z is the longitudinal coordinate (which remains unchanged) while $v_g = c/n_r$ is the group velocity. In this reference framework, the DDEs for the field at both Ground State and first Excited State wavelengths yield

$$\frac{dV_i(\tau)}{dt} = -\Gamma V_i(\tau) + \Gamma R_i(\tau - T_R) V_i(\tau - T_R), \quad (3.53)$$

where the index $i = \text{GS, ES1}$ represents the energy level considered. The physical meaning of each term introduced in the previous equation is now explained in more details.

Spectral filtering and ML condition

Equation 3.53 can be rewritten as

$$\frac{1}{\Gamma} \frac{dV_i(\tau)}{dt} = -V_i(\tau) + R_i(\tau - T_R) V_i(\tau - T_R), \quad (3.54)$$

where the term 2Γ is the FWHM of the Lorentzian filter introduced in the previous Section, causing inhomogeneous gain broadening. A steady-state analysis can be carried out by neglecting the derivative term, or equivalently assuming the absence of spectral filtering due to the finite gain bandwidth (i.e. $\Gamma \rightarrow \infty$). In these conditions, the previous equation reduces to

$$V_i(\tau) = R_i(\tau - T_R) V_i(\tau - T_R). \quad (3.55)$$

From the physical perspective, Equation 3.55 states that a pulse at section $z = 0$ at time τ , $V_i(\tau)$, is equal to the one crossing the same section at the previous round trip, $V_i(\tau - T_R)$, that has experienced a round trip gain $R_i(\tau - T_R)$ during the subsequent propagation along the cavity. To achieve a stable mode locking regime in the absence of spectral filtering, the ML pulse must not change in successive round trips, and such condition can be expressed as

$$V_i(\tau) = V_i(\tau - T_R) \iff \begin{cases} R_i(\tau - T_R) = R_i(\tau) = 1, & V_i(\tau) \neq 0 \\ R_i(\tau - T_R) = R_i(\tau) < 1, & V_i(\tau) = 0 \end{cases}. \quad (3.56)$$

Notice that the second condition in Equation 3.56 is introduced to avoid the onset of instabilities due to spontaneous emission noise when the ML pulse power is zero.

When the limited gain bandwidth of the QD ensemble is taken into account, meaning that Γ is finite, the derivative term can no longer be neglected. In this case, a Lorentzian bandwidth limiting element is introduced in the device model, lumped in the reference section $z = 0$ and acting on the pulse at each round trip. Such filtering effect is represented by the derivative term in Equation 3.53, which can be rewritten as a convolution product to highlight it:

$$V_i(\tau) = [\Gamma \exp(-\Gamma\tau)] \otimes [R_i(\tau - T_R) V_i(\tau - T_R)]. \quad (3.57)$$

Round trip gain

The reference structure for this analysis is the two-section ring reported in Figure 3.23. Both the gain and SA sections are further subdivided into F isolated

slices: the carriers evolution is computed in each of these regions, at the boundaries of which the non-saturable losses are localized. The total cavity length is given by the sum of the F sections lengths, i.e.

$$L = \sum_{k=1}^F L_k, \quad (3.58)$$

from which the cold-cavity round trip time can be determined as

$$T_R = \frac{L}{v_g}. \quad (3.59)$$

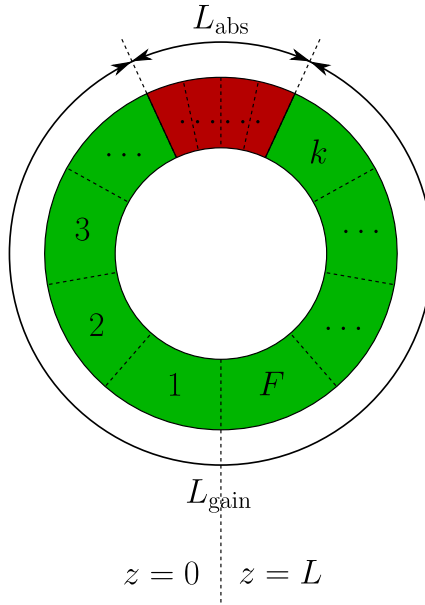


Figure 3.23: Two-section ring structure, subdivided into F electrically isolated slices.

The term R introduced in Equation 3.53 represents the round trip gain experienced by the pulse during the propagation along forward and reversely biased sections of the cavity. It depends on the nonlinear gain and absorption dynamics induced by the pulse circulating within the cavity, and it can be computed as

$$R_i(\tau) = \prod_{k=1}^F B_{i,k}(\tau) M_k, \quad (3.60)$$

where $i = \text{GS}$, ES1 refers again to the considered energy level. M_k describes the non-saturable losses localized between the k^{th} and the $(k+1)^{\text{th}}$ sections, including

intrinsic waveguide losses experienced by the field when traveling across the k^{th} section and output coupling losses localized at the interface:

$$M_k = \sqrt{K_k} \exp\left(-\frac{\alpha_i}{2} L_k\right). \quad (3.61)$$

The term $B_{i,k}(\tau)$ represents instead the amplification (or attenuation) and the phase change experienced by the field when traveling across the k^{th} section, and its value is different according to the analyzed wavelength:

$$\begin{cases} B_{\text{GS},k}(\tau) = \exp\left(\Gamma_{xy} \bar{g}_{\text{GS},k}(\tau) L_k\right) \times \exp\left(j\beta \Gamma_{xy} \bar{g}_{\text{ES1},k}(\tau) L_k\right) \\ B_{\text{ES1},k}(\tau) = \exp\left(\Gamma_{xy} \bar{g}_{\text{ES1},k}(\tau) L_k\right) \times \exp\left(-j\beta \Gamma_{xy} \bar{g}_{\text{GS},k}(\tau) L_k\right) \end{cases}. \quad (3.62)$$

In Equation 3.62, the average gain/absorption introduced by the QD GS or ES1 in the k^{th} section is given by

$$\bar{g}_{i,k}(\tau) = g_{0,i} \left(2\bar{f}_{i,k}(\tau) - 1\right), \quad (3.63)$$

where $g_{0,i}$ is the characteristic material gain for the dot energy level introduced in Equation 3.42, while $\bar{f}_{i,k}(\tau)$ represents the occupation probability in the i^{th} QD state averaged over the k^{th} section. The temporal dynamics of this occupation function in each section of the ring cavity are given by a system of rate equations:

$$\frac{d\bar{f}_{i,k}(\tau)}{d\tau} = \bar{R}_{i,k}^{\text{in}}(\tau) - \bar{R}_{i,k}^{\text{out}}(\tau) - \bar{R}_{i,k}^{\text{st}}(\tau). \quad (3.64)$$

The first two rates reported in Equation 3.64 are computed according to the equations presented in Section 2.2, while the stimulated emission rate in this case is evaluated as

$$\bar{R}_{i,k}^{\text{st}}(\tau) = \left(|B_{i,k}(\tau)|^2 - 1\right) \left(\prod_{m=1}^{k-1} |B_{i,m}(\tau)|^2 M_m^2\right) \frac{|V_i(\tau)|^2}{\hbar(\varepsilon_{e,i} - \varepsilon_{h,i}) L_k}. \quad (3.65)$$

Finally, the output power after a full round trip (i.e. at the end of the F^{th} section) is given by

$$P_i^{\text{out}}(\tau) = \frac{1 - K_F}{K_F} |V_i(\tau)|^2, \quad (3.66)$$

where K_F corresponds to the output coupling factor of the ring laser.

Equation 3.65 can be derived by following a similar approach to that proposed in [109], and it has a clear physical meaning in the DDE model framework. In particular, the total power lost at time τ due to electron-hole pairs recombination in the active material (at emission wavelength i and in section k) is

$$P_{i,k}^{\text{st}}(\tau) = \hbar(\varepsilon_{e,i} - \varepsilon_{h,i}) \bar{R}_{i,k}^{\text{st}}(\tau) L_k. \quad (3.67)$$

This quantity can be evaluated as the difference between instantaneous output and input power values from the considered k^{th} section:

$$P_{i,k}^{\text{st}}(\tau) = \underbrace{\prod_{m=1}^k |B_{i,m}(\tau)|^2 M_m^2 |V_i(\tau)|^2}_{P_{i,k}^{\text{out}}} - \underbrace{\prod_{m=1}^{k-1} |B_{i,m}(\tau)|^2 M_m^2 |V_i(\tau)|^2}_{P_{i,k}^{\text{in}}}. \quad (3.68)$$

Such equation guarantees the energy conservation in the active material, and it is valid when no additional non-saturable losses are distributed along the section, hence it can be exploited when considering them lumped at the interface between adjacent sections as assumed in the MS-DDE model.

3.5.3 Effects included in the model

Several additional effects should be taken into account when analyzing the behavior of semiconductor ML lasers. Some of them have been included in the proposed MS-DDE model, and they are presented in the following with a basic description of the physical mechanisms that may cause their presence.

Self-Phase Modulation

The gain (or absorption) spectrum induced by the QD semiconductor active medium and the associated changes in the refractive index have been determined in Section 3.4, with an explicit dependence on the imaginary and real part of the optical susceptibility, respectively. These two quantities are related through the **Kramers-Krönig relations** [28]:

$$\text{Re}\{\bar{\chi}(z, t, \Omega)\} = \frac{1}{\pi} \mathcal{P} \int_{-\infty}^{+\infty} \frac{\text{Im}\{\bar{\chi}(z, t, \Omega')\}}{\Omega' - \Omega} d\Omega', \quad (3.69)$$

$$\text{Im}\{\bar{\chi}(z, t, \Omega)\} = -\frac{1}{\pi} \mathcal{P} \int_{-\infty}^{+\infty} \frac{\text{Re}\{\bar{\chi}(z, t, \Omega')\}}{\Omega' - \Omega} d\Omega', \quad (3.70)$$

where \mathcal{P} is the Cauchy principal value of the integral [115].

Refractive index changes are due to both interband transitions (Equation 3.43) and intraband free carrier absorption (Equation 3.45). From these relations, it clearly appears that a variation in electron and hole populations leads not only to a nonlinear gain dynamics, but also to a nonlinear behavior of the refractive index. Hence, alongside a variation in the envelope, a phase shift is induced in the optical pulse traveling along the QD active medium. Such nonlinear phase change is commonly referred to as **self-phase modulation** (SPM), and the pulse is said to be *chirped* since its carrier frequency varies in time.

An unchirped ML pulse is characterized by a time-independent carrier frequency, corresponding to a constant phase over the whole bandwidth in the frequency domain. In this case, assuming a Gaussian envelope, a precise relation between the pulse duration in time $\Delta\tau$ (FWHM) and the -3 dB bandwidth $\Delta\nu$ of its optical power spectrum holds [116]:

$$\text{TBP} = \Delta\tau\Delta\nu = \frac{2 \log 2}{\pi} \approx 0.44. \quad (3.71)$$

This represents the theoretical lower bound for the *time-bandwidth product*, and the pulse is said to be **transform limited**. On the other hand, a linear carrier frequency chirp in time causes the power spectral density of the pulse to be broader with respect to the unchirped case, hence the TBP increases (TBP = $\Delta\tau\Delta\nu > 0.44$).

Notice that the minimum value of the TBP depends on the exact pulse shape: Gaussian envelopes are characterized by a TBP > 0.44 , whereas squared hyperbolic secant ones have TBP > 0.32 . In many applications, though, determining the pulse shape is not immediate, and different approaches can be followed.

- The most rigorous approach relies on the *Frequency Resolved Optical Gating* (FROG) technique [117].
- A Gaussian shape for the ML pulse envelope can be assumed, without further investigation of time- and frequency-domain behavior.
- The *intensity autocorrelation* can be characterized with common instruments, both in terms of time duration (commercial autocorrelator) and spectrum (optical spectrum analyzer), then the TBP is used to infer the pulse shape and to quantify the amount of chirp in the ML pulse.

Gain and refractive index dispersion

Due to its limited bandwidth, the gain spectrum in the forward biased sections of the device acts as a filter on the pulse. Clearly, a wide gain bandwidth allows to increase the number of longitudinal lasing modes that can contribute to the ML pulse formation, thus leading to a shorter pulse width.

In addition, also the refractive index of the cavity has a frequency dependent behavior, with an overall spectrum identified as $n_r(\omega)$. This comes from both the frequency dependence of the effective index of waveguide modes and the spectral behavior of the semiconductor active medium. Recall that the group velocity is inversely proportional to the refractive index derivative with respect to the frequency (Equation 3.21). If the second derivative $\partial^2 n_r(\omega)/\partial\omega^2$ is not null around the pulse carrier frequency, different spectral components propagate at different group velocities, and the material is said to be **dispersive**. This may lead to broadening and distortion phenomena in the ML pulses, especially in the case of ultrashort ones (characterized by a broad spectrum).

ML self-starting

The possibility for the mode locking regime to start autonomously represents an additional feature of QD ML lasers that need to be investigated.

1. When increasing the pump current in the active sections of the device, still remaining below threshold, random field oscillations are caused by spontaneous emission processes within the cavity.
2. If the current is gradually increased, a *first threshold* is reached where the unsaturated linear modal gain equals the total losses in the cavity, given by mirrors and SA section (both unsaturated).
3. Spontaneous emission noise tends to excite a large number of longitudinal cavity modes, with stochastic amplitudes and phases, leading to the presence of random noise spikes in the time domain signal which can be amplified along the device.
4. Further increasing the current, a *second threshold* is reached where a single noise spike becomes intense enough to cause absorption saturation in the SA section: in this way, such spike can be amplified and reshaped over successive round trips, leading to the formation of a single pulse circulating along the waveguide.

The same phenomenon can be explained from the frequency domain perspective. The initial noise spike is the result of a phase locking between different adjacent modes in a certain time interval, according to the basic description provided in Section 3.1. This phase relation is then preserved by the absorption saturation, leading to the onset of a stable ML regime.

Optical losses

The electromagnetic radiation is not completely restricted by the ridge waveguide section, since a portion of it falls out of the device boundaries as reported in Figure 3.24a. This phenomenon can also be inferred from the 2D simulation results reported in [118], where a modal analysis on single-mode waveguides has been carried out (Figure 3.24b).

Apart from the saturable and unsaturable loss terms that have been presented in the previous Sections, then, an additional contribution to the overall device losses can be associated to the ridge waveguide structure. The presence of these queues can be accounted for in the proposed MS-DDE model in order to provide a more complete description of the QD ML laser behavior.

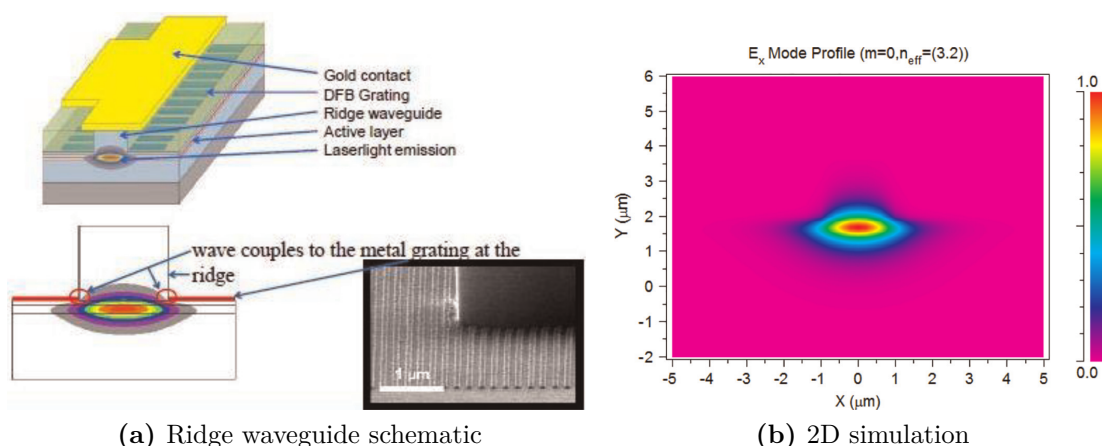


Figure 3.24: Structure and simulation results presented in [118].

Ring unidirectionality

Some further considerations can be provided concerning ring unidirectionality, which has been assumed for both previous and current versions of the DDE model. A basic ring structure would however result in bidirectional lasing, due to the rotational symmetry between propagating and counter-propagating modes along the cavity. In order to break such symmetry, different techniques have been presented in the literature, and two significant examples are reported in the following.

By introducing in the device a S-shaped waveguide within the ring resonator as the one shown in Figure 3.25, an asymmetric behavior for clockwise (CW) and counterclockwise (CCW) beams is obtained [119].

- The CW wave is launched from point A, and it propagates unchanged up to the coupling region B_1 . Here, part of it is evanescently coupled to the S structure, generating two waves that move towards C_1 (radiated out of the device) and B_2 . The same coupling occurs at the opposite end of the S waveguide, with a portion of the latter wave that is joint again to the main CW one inside the ring.
- Similarly, a part of the CCW signal launched from point A is evanescently coupled to the S-shaped element in B_2 , but the portion that propagates along it and is coupled back into the ring racetrack is transformed into CW moving at section B_1 .

In this way, the field propagating along the unwanted direction is partially converted into the preferred one through a double evanescent coupling mechanism. Overall, the field intensity is reduced (significant losses are introduced), but the desired mode prevails after a certain number of round trips along the cavity.

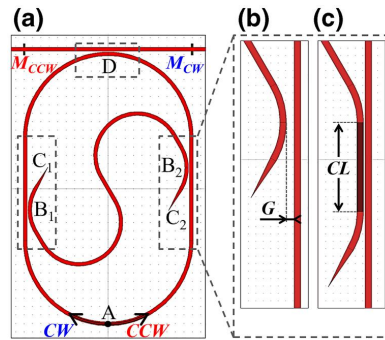


Figure 3.25: S-shaped waveguide embedded into the ring device [119].

An alternative approach presented in [120] exploits instead the presence of defects in the QD-based waveguide to tune the propagation direction in ring lasers. When a traveling wave encounters a defect in the active material, reflection phenomena may occur, thus leading to the presence of counterpropagating ML pulses. By means of defect engineering, such features can be tailored making the unwanted propagation direction less favorable than the wanted one, finally obtaining a unique ML pulse train prevailing. Notice also that this technique can be employed in order to tune the spacing between adjacent modes of harmonic frequency combs, providing a further “knob” to trim the device performance.

Chapter 4

Simulation Results

4.1 Unidirectional ring lasers

The main purpose of this Thesis has been to improve a pre-existing MS-DDE MATLAB program in terms of computational efficiency (with simulation times reduced of almost one order of magnitude) and generality, exploring the possibility of modeling harmonic ML too. In this way, the model represents a fast and reliable simulation tool that can be employed in the design phase of mode-locked semiconductor lasers. In particular, the starting point is always a set of known constraints and requirements, both technological (related to the device fabrication process) and fixed by the target application. For this reason, the following approach has been chosen in order to provide useful information during the preliminary stages of a design activity involving the presence of ML ring lasers.

1. At first, the main requirements in terms of repetition rate, bias range and size are introduced to mimic a real-life scenario.
2. Then, a suitable set of physical and technological parameters allowing to satisfy the initial constraints is identified. Notice that several quantities involved in the model depend on the material or the fabrication process, hence they cannot be exploited to tune the device properties. On the other hand, a certain degree of flexibility is still granted by the presence of other “knobs” through which the requirements can be fulfilled.
3. Once the obtained simulation results are compliant with the specifications, the parameters set is fixed and the number of sections constituting the device is varied. In this way, a direct comparison in terms of footprint, operating range and power consumption is carried out: the designer can then choose among different implementations according to other application-specific constraints.

In the following, an 8-section device working at a repetition rate equal to 75 GHz is designed, and then alternatives relying on a different number of sections are introduced. Before this analysis, though, few additional details concerning the application of the MS-DDE model to this specific type of device are provided.

4.1.1 MS-DDE modeling of ring structures

Consider again the reference 2-section ring structure, composed of a single gain-SA couple whose length is sliced into F electrically isolated subsections in order to perform the simulation with the MS-DDE model (Figure 4.1). A uniform current injection is assumed in the whole gain section, subdivided uniformly, hence all the forward biased slices are characterized by the same current density. On the other hand, the SA slices (again uniform among themselves, but in general characterized by a different length with respect to the gain ones) are reversely biased with an external negative voltage.

Concerning the output signal, it is assumed to be extracted in the middle of the gain section, i.e. at $z = 0$. Such extraction implies the presence of an output coupling mechanism, localized in the chosen reference section and modeled through a power transmission coefficient K which is lower than 100% from the internal field perspective. As an example, a 10% power extraction at section $z = 0$ corresponds to the following set of coupling losses:

$$K_k = \begin{cases} 1 & k = 1, 2, \dots, F - 1 \\ 0.9 & k = F \end{cases}, \quad (4.1)$$

meaning that 90% of the power is staying inside the cavity. In terms of traveling wave equations, the field boundary condition at the end of each round trip then becomes

$$V_i(t,0) = \sqrt{K_F} V_i(t, L), \quad (4.2)$$

where L is the total ring cavity length and the subscript $i = \text{GS}, \text{ES1}$ refers to the considered energy level.

The simulation of ring structures relies on the equations presented in Section 3.5, but some additional considerations have to be introduced in order to study the properties of such devices. In particular, the ML stability is investigated by considering the round trip gain experienced by the traveling pulses in the cavity, which can be rewritten in a different form with respect to Equation 3.60 as

$$|R_i(\tau)| = \exp \left[\left(G_i(\tau) - A_i(\tau) \right) L \right]. \quad (4.3)$$

The term $G_i(\tau)$, expressed in cm^{-1} , represents the overall amplification in the gain section, computed as

$$G_i(\tau) = \frac{1}{L} \sum_{k \in \text{G}} \ln \left(|B_{i,k}(\tau)| \right). \quad (4.4)$$

On the other hand, $A_i(\tau)$ (again in cm^{-1}) expresses the overall saturable and non-saturable losses experienced by the ML pulse over a round trip, given by

$$A_i(\tau) = \frac{\alpha_i}{2} + \frac{1}{L} \left[\sum_{k \in \text{SA}} \ln(|B_{i,k}(\tau)|) + \sum_{k=1}^F \ln\left(\frac{1}{\sqrt{K_k}}\right) \right]. \quad (4.5)$$

The ultrafast recovery of the ground state population after the pulse trailing edge, due to the presence of fast ES to GS transitions in the QD active material, leads to a steep increase of the gain term $G_{\text{GS}}(\tau)$. According to Equation 4.3, this corresponds to a window of net gain $R_{\text{GS}}(\tau) > 1$ which can cause a trailing edge instability in the presence of spontaneous emission noise. Such instability is usually prominent for bias currents just above threshold, whereas it becomes negligible increasing the applied current (since the positive net gain region tends to vanish).

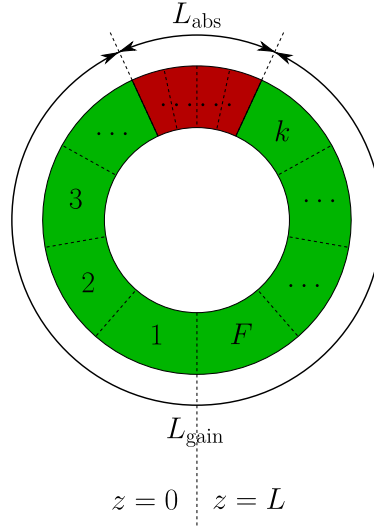


Figure 4.1: Two-section ring structure, divided into F electrically isolated slices.

4.1.2 Design and simulation of an 8-section device

As previously stated, the first step in the design process of a semiconductor ML laser is the identification of the main constraints and requirements dictated by both target application and technology. Concerning the final performance of the device, a repetition rate equal to $f = 75 \text{ GHz}$ is required in this study (GS emission), working at temperature $T = 298 \text{ K}$. In order to limit the total power consumption, the bias range should be limited to:

$$\begin{cases} I = (100 \div 400) \text{ mA} & z \in \text{G} \\ V = (-7.5 \div -2.5) \text{ V} & z \in \text{SA} \end{cases}. \quad (4.6)$$

Table 4.1 reports instead a list of the main physical parameters used in the simulation, which will be maintained in the different implementations presented in the following of this analysis.

Symbol	Description	Value
d	Ridge waveguide width	6 μm
α_i	Intrinsic waveguide losses	1.5 cm^{-1}
Γ_y	Transversal confinement factor	75%
Γ_x	Vertical confinement factor	10%
n_r	Refractive index	3.66
η_i	Internal quantum efficiency	85%
h_{SCH}	SCH height	180 nm
h_{QW}	QW height	7 nm
h_{QD}	QD height	5 nm
N_l	QD layers	12
N_D	QD surface density	$2.85 \times 10^{10} \text{ cm}^{-2}$
R_{QD}	QD radius	15.5 nm
ΔE^{inh}	FWHM inhomogeneous broadening	34 meV
$E_{(e-h),\text{GS}}$	GS interband transition energy	0.9904 eV
$E_{(e-h),\text{ES1}}$	ES1 interband transition energy	1.0597 eV
$\tau_{c,\text{GS}}$	GS capture time	0.3 ps
$\tau_{c,\text{ES1}}$	ES1 capture time	0.3 ps
V_{bi}	Built-in potential	0.8 V

Table 4.1: Main physical parameters used in the simulation [18].

Once these constraints have been fixed, the device performances are tuned by means of few remaining free parameters. From a preliminary analysis, the role of the output coupling coefficient has turned out to be crucial in the achievement of a stable harmonic ML. In particular, a high transmission value in the reference section¹ $z = 0$ allows to reach the locking condition for rather lower values of the bias current, hence a 10% signal extraction is considered (i.e. $K_F = 90\%$).

Given the interest in colliding pulse ML mechanisms in semiconductor QD lasers, the number of gain sections has been fixed to 4 (Figure 4.2), thus leading to an expected output frequency f corresponding to the fourth harmonic with respect

¹Recall that by using the MS-DDE model the output signal can be extracted at any interface between adjacent slices of the device, both in the gain and SA regions. The choice presented here is arbitrary, simply allowing a clearer description in terms of round trip gain for the field evolution inside the cavity.

to the fundamental one (f_R). Recall that the latter depends on the total cavity length as

$$f_R = \frac{1}{T_R} = \frac{v_g}{L} = \frac{c}{n_r L}. \quad (4.7)$$

By imposing the required repetition rate, $f = 75$ GHz, the ring length is then determined:

$$f_R = \frac{f}{4} = 18.75 \text{ GHz} \iff L = 4380 \text{ }\mu\text{m}. \quad (4.8)$$

Assuming a uniform division into slices of both gain and SA sections, it can be stated that

$$L_{\text{gain}} + L_{\text{abs}} = \frac{L}{4} = 1095 \text{ }\mu\text{m}, \quad (4.9)$$

where L_{gain} and L_{abs} are the lengths of each section composing the device. The chosen length for gain sections is $L_{\text{gain}} = 840 \text{ }\mu\text{m}$, whereas the SA regions represent approximately the 30% of the total cavity length. This is actually a rather large percentage when compared to standard devices working at the fundamental frequency, and it is justified by the high requirements in terms of pulse shaping when multiple pulses are present within a round trip period.

Finally, the number of slices has been set to $F = 40$, representing a trade-off between spatial resolution and computational efficiency. Spontaneous emission noise and plasma effects have not been considered in this preliminary design phase, whereas the contribution of self-phase modulation and additional waveguide losses due to boundary effects are included in the simulation. A portion of the MATLAB code corresponding to the described structure is reported in Section A.1.

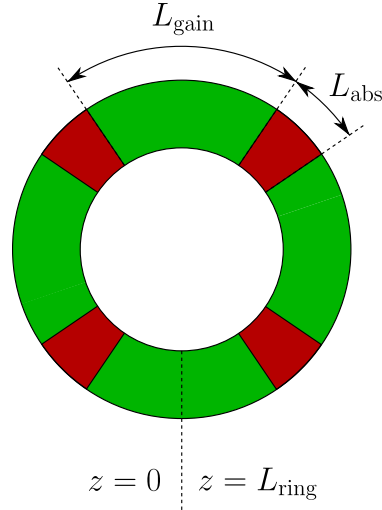


Figure 4.2: 8-section ring structure.

Repetition rate and stability

The device behavior has been analyzed in the active region current - reverse bias voltage plane, verifying for each couple of values if optical pulses are generated, extracting the repetition frequency from their RF spectrum and observing if they are stable or suffering from leading/trailing edge instabilities. The main simulation results for the 8-section ring structure presented before are reported in Figure 4.3, from which the device working boundaries can be established.

- The colormap allows to evaluate the achieved oscillation frequency with respect to the fundamental one, depending on the chosen bias values. In this case, the region of interest is the green one, corresponding to a harmonic mode locking at $f = 4 \times f_R = 75$ GHz as required.
- Superimposed on this map, the instability regions are highlighted by oblique black lines, determined according to Haus' criterion [105]. In particular, the net gain in the active material must become negative immediately after the ML pulse has passed, otherwise spontaneous emission noise may be amplified by a net gain window following the pulse trailing edge and leading to instability.

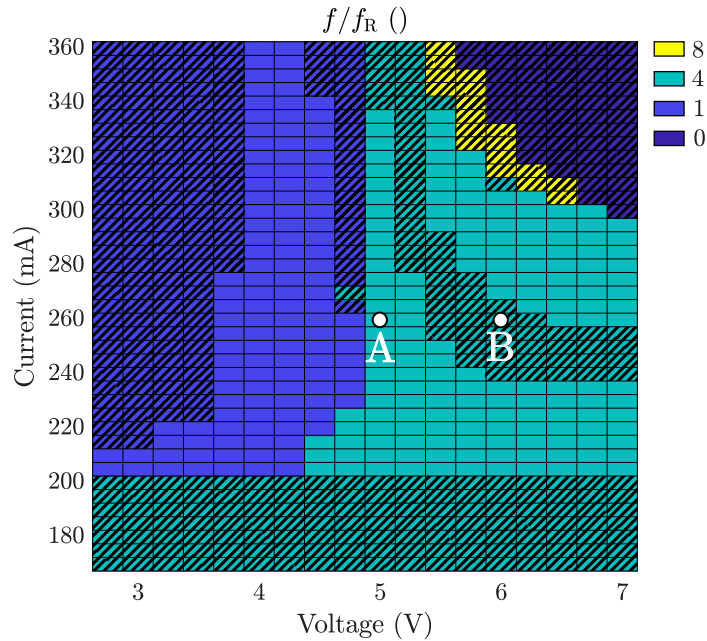


Figure 4.3: Map of the repetition rate with respect to the fundamental one, with highlighted unstable regions.

In the design phase of the whole system, the bias values have to be chosen according to the previous considerations in order to obtain a stable pulse train. An

exemplary comparison between stable and unstable points of the map is reported here, considering points A ($I = 260$ mA, $V = -5$ V) and B ($I = 260$ mA, $V = -6$ V) identified in the map.

- Point A.** This point is characterized by the desired frequency, and consequently four pulses can be identified within a round trip period $T_R = 53.5$ ps, as shown in Figure 4.4a. Notice that this can also be checked in the frequency domain, since the peak of the RF spectrum is located at the aforementioned frequency. This type of oscillation can be considered stable, meaning that the ML condition is achieved at the steady state and there are no net gain windows outside the pulses boundaries that may amplify the spontaneous emission noise. The pulse width has also been computed, exploiting the autocorrelation function of the pulses and assuming a Gaussian shape for them; a pulse width of 3.84 ps has been obtained.
- Point B.** Conversely, point B cannot be considered acceptable for harmonic ML operation. Despite being characterized by the correct output frequency, the pulses turn out to be distorted, and in particular characterized by a strong trailing edge instability that can be seen in Figure 4.4b. In these conditions, the oscillation is not stable, and generally the amplitudes of the pulses evolve without reaching a regular steady-state pulse generation.

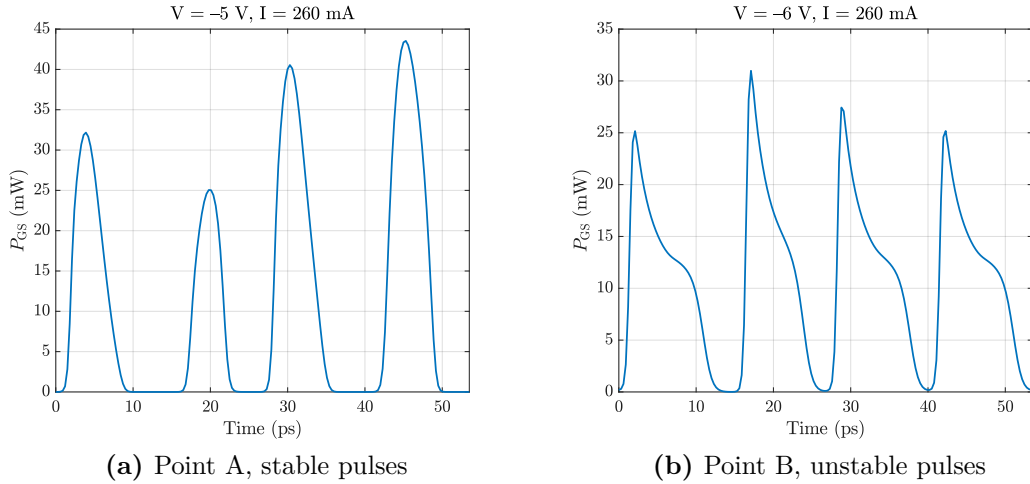


Figure 4.4: Pulses in the time domain within a round trip period.

As it was previously stated, the repetition rate obtained for each point of the map is determined by analyzing the RF spectrum of the device, and in particular it corresponds to the frequency associated to the spectral maximum. The two spectra

obtained for points A and B and the corresponding maxima (both at $f = 4 \times f_R$, identified by red markers) are reported in Figure 4.5a and Figure 4.5b, respectively. From these graphs, it can be inferred that:

- the obtained output signals cannot be perfectly sinusoidal due to the presence of several spectral lines at integer multiples of the fundamental frequency;
- stronger high-frequency components allow shorter pulses to be achieved;
- in the case of unstable configurations, low-frequency components are more spread around the multiples of f_R .

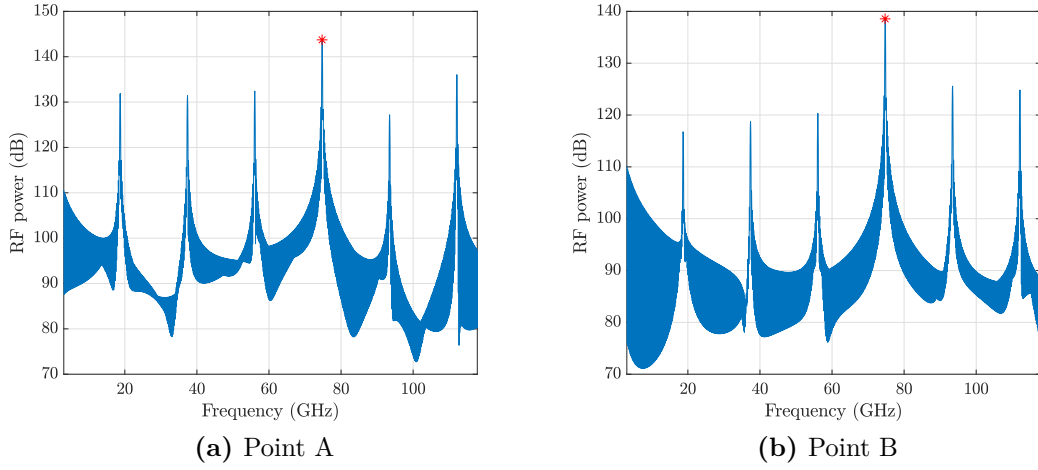


Figure 4.5: RF spectra for the two considered cases.

Photocurrent and output power

Other figures of merit have been obtained from the simulation. The average photocurrent extracted from the SA regions of the device has been computed as

$$\bar{I}_{\text{ph}} = \frac{qV\mu_n}{h_{\text{SCH}}^2} \bar{n}_{\text{SCH}}, \quad (4.10)$$

where q is the elementary electron charge, V is the applied reverse bias voltage, μ_n is the electron mobility in the conduction band, while h_{SCH} and \bar{n}_{SCH} are the SCH height and average carrier density, respectively. The results obtained with this approach are 101.6 mA for point A and 152.3 mA for point B, in line with the expectations since the latter is characterized by a larger bias voltage.

The photocurrent represents one of the key performance indicators when considering the possible usage of mode-locked QD lasers in RF applications, since it corresponds to the actual high-frequency electrical signal extracted from the saturable absorber. From an energy efficiency standpoint, its average value is useful to evaluate the conversion between input bias current and output photocurrent, around 40% for point A. However, in the case of RF signal generators as the one presented in Figure 4.6, the bandwidth-limiting effect due to additional electrical components (bias tee and antenna) can be taken into account by introducing a band-pass filter (BPF) in the model. Figure 4.7a reports the amplitude response of the chosen BPF, with a 10 GHz wide passband (highlighted by red dashed lines) centered at the chosen harmonic component $f = 75$ GHz. As a result, the extracted photocurrent becomes an almost perfectly sinusoidal signal (Figure 4.7b).

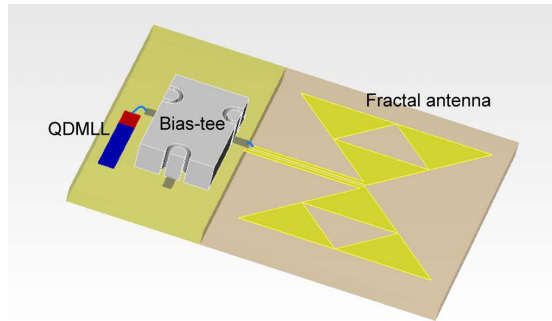


Figure 4.6: RF signal generator proposed by Lin et al. [87].

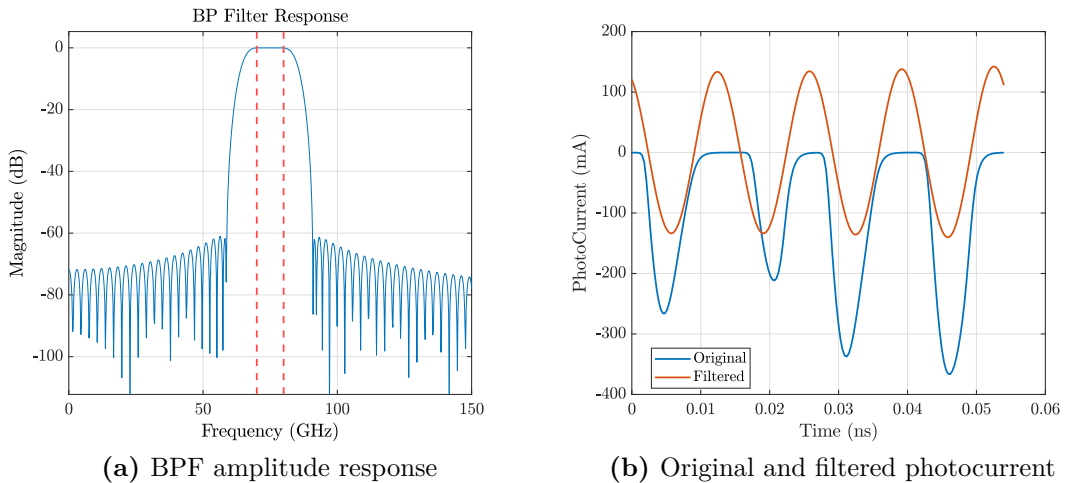


Figure 4.7: Filtering effect of external electrical components on the photocurrent.

Concerning the extracted pulse average and peak power (with a 10% output coupling coefficient), the former is expected to be smaller in a pulse train, since the light intensity should be nearly zero for large portions of the round trip period. This has been confirmed by analyzing the results for point A, yielding $P_{\text{avg}} = 1.27 \text{ mW}$ and $P_{\text{max}} = 4.88 \text{ mW}$. On the other hand, point B is characterized by lower peak values ($P_{\text{max}} = 3.56 \text{ mW}$) due to the instability of this operating conditions: the optical power is spread on a wider pulse, hence reducing its maximum value, whereas the average one is almost unchanged ($P_{\text{avg}} = 1.24 \text{ mW}$).

An overview of these two quantities in the whole bias map is reported in Figure 4.8. Both average and peak power appear to be higher for high current and low voltage values, i.e. approaching the top left corner of the two graphs. This can be easily explained by considering the repetition rate map (Figure 4.3): in the presence of a lower number of pulses circulating in the cavity, the power is more concentrated in each of them and therefore P_{max} is higher. Moreover, the pulse width increases when reducing the reverse voltage to the SA section, eventually causing leading edge instability, hence a larger average power is also obtained.

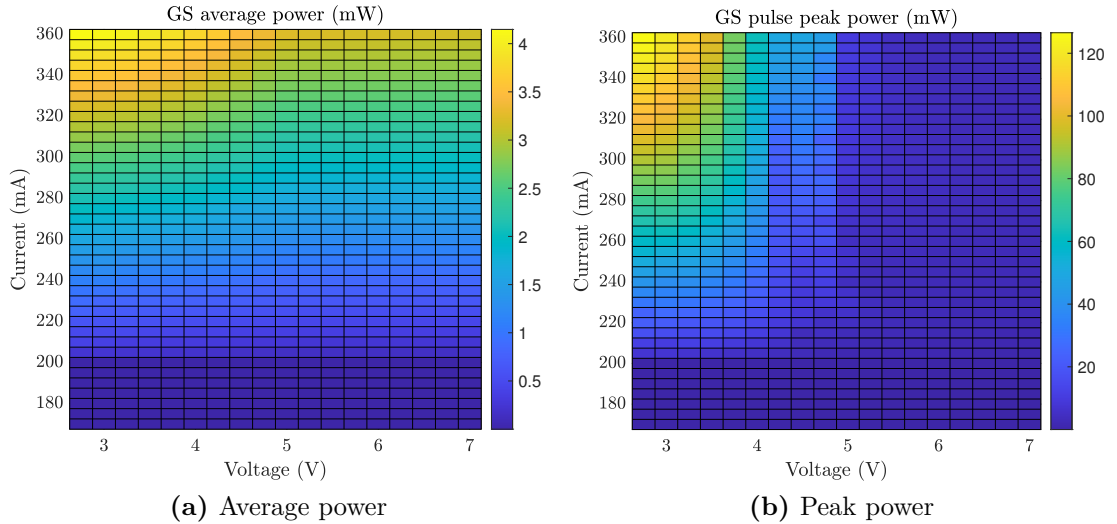


Figure 4.8: Average and peak power values in the considered bias range for the 8-section device.

4.1.3 Comparison with alternative structures

Once the reference 8-section device has been completely characterized, the number of gain-SA sections couples is varied to compare several possible design choices. The simulation results obtained in this phase of the study are presented in the following.

6-section

The number of sections is initially reduced to 6 without varying their individual lengths. Consequently, the total ring cavity length becomes

$$L = 3(L_{\text{gain}} + L_{\text{abs}}) = 3285 \mu\text{m}, \quad (4.11)$$

corresponding to a fundamental repetition rate $f_{\text{R}} = 25$ GHz.

Figure 4.9 shows the repetition rate achieved with this device in the same bias range as the 8-section one. Here the target frequency is $f = 3 \times f_{\text{R}} = 75$ GHz, corresponding to the green color in the map. The stability analysis shows that a larger portion of the map is not suffering from leading/trailing edge instabilities with respect to the previous case: this may be convenient when a precise control of the bias quantities is not possible.

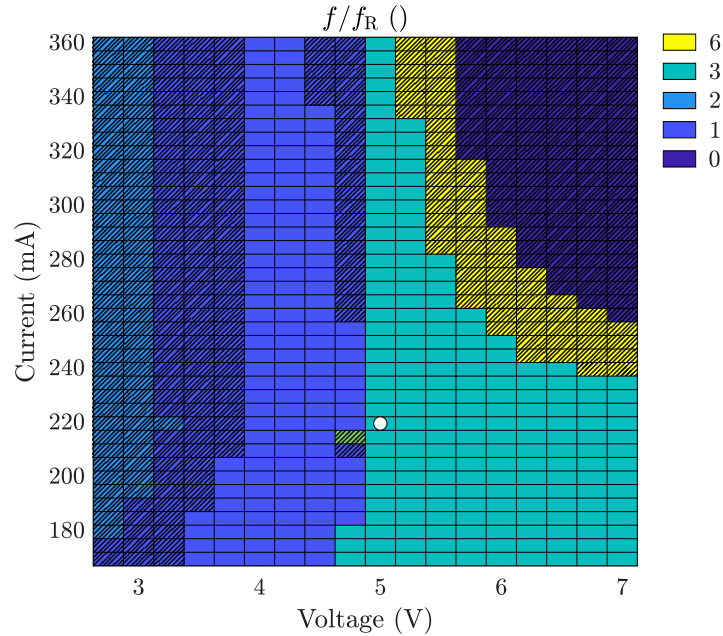


Figure 4.9: Repetition rate and stability, 6-section device. The marker highlights the chosen point for the following analysis.

A single bias point has been chosen on the map to make an explicit comparison between 6- and 8-section devices, characterized by $I = 220$ mA and $V = -5$ V. The correct locking frequency is confirmed by both the RF spectrum (Figure 4.10a) and the presence of three pulses in the round trip temporal window, which in this case is equal to $T_{\text{R}} = 40$ ps. These pulses appear to be stable (Figure 4.10b), but their width is higher with respect to the previous case (4.09 ps).

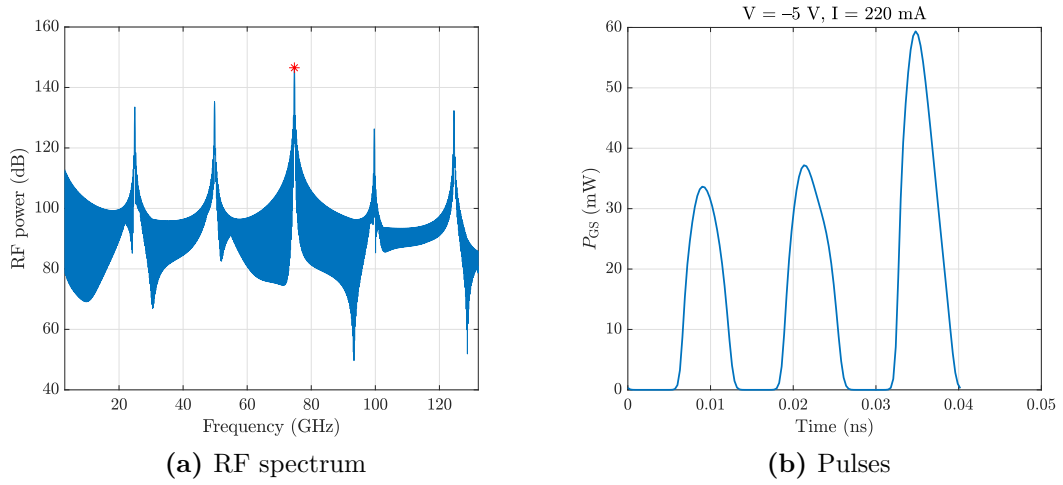


Figure 4.10: Frequency and time domain behavior for the chosen bias values for the 6-section device.

Having chosen the same bias voltage as a reference, the photocurrent is almost equal to the one obtained with the 8-section device ($\bar{I}_{ph} = 101.1 \text{ mA}$). On the other hand, both average ($P_{avg} = 1.68 \text{ mW}$) and peak power ($P_{max} = 6.97 \text{ mW}$) are higher in this case, and this consideration is valid for the whole considered range as expected in the presence of fewer but wider pulses (Figure 4.11).

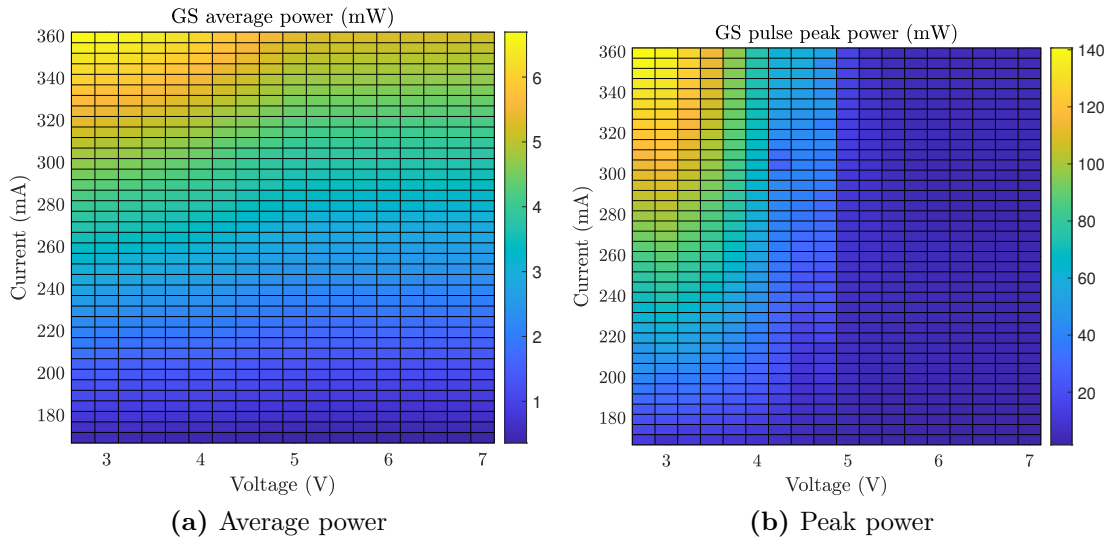


Figure 4.11: Average and peak power values in the considered bias range for the 6-section device.

4-section

The number of sections has then been reduced to 4, with a cavity length equal to

$$L = 2(L_{\text{gain}} + L_{\text{abs}}) = 2190 \mu\text{m}. \quad (4.12)$$

The fundamental repetition rate for this laser diode is $f_{\text{R}} = 37.5 \text{ GHz}$, and the required frequency $f = 2 \times f_{\text{R}} = 75 \text{ GHz}$ is obtained with a 2-pulse harmonic mode locking.

The stable area in the repetition rate map is strongly reduced in this case when compared to the previous ones (Figure 4.12), with rather few points satisfying Haus' stability criterion at a ML frequency equal to twice the fundamental one. Clearly, moving away from the initial total ring length would require different considerations in terms of bias current and single sections lengths, but these quantities have been constrained as explained before to highlight these differences.

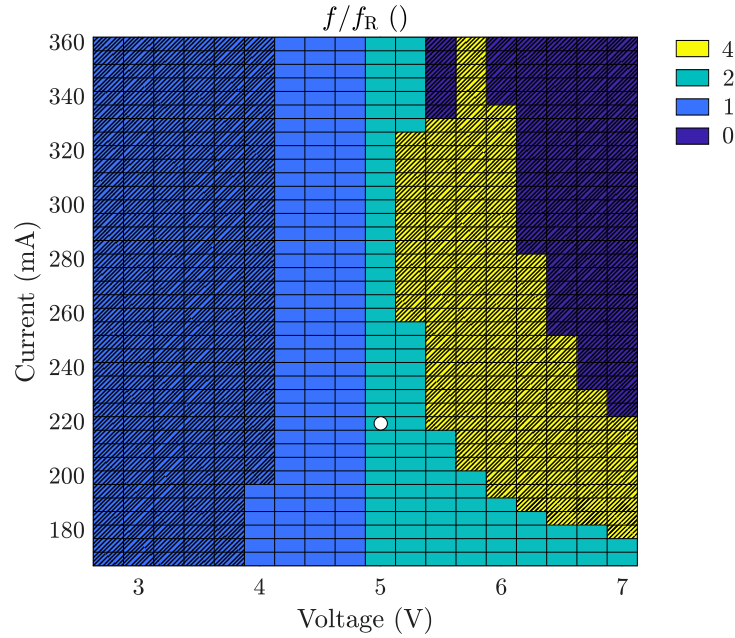


Figure 4.12: Repetition rate and stability, 4-section device. The marker highlights the chosen point for the following analysis.

The same point as in the 6-section case ($I = 220 \text{ mA}$, $V = -5 \text{ V}$) has been chosen as a reference for the pulse analysis, yielding a peak in the RF spectrum at twice the fundamental frequency as expected (Figure 4.13a). Notice, however, that such current value implies a higher gain in the active sections of the device, leading to the presence of very thin net gain windows at the boundaries of the pulse that may cause it to become wider. This is confirmed by studying the two

pulses reported in Figure 4.13b, which are characterized by a wider shape (4.98 ps) that preludes to a trailing edge instability, too.

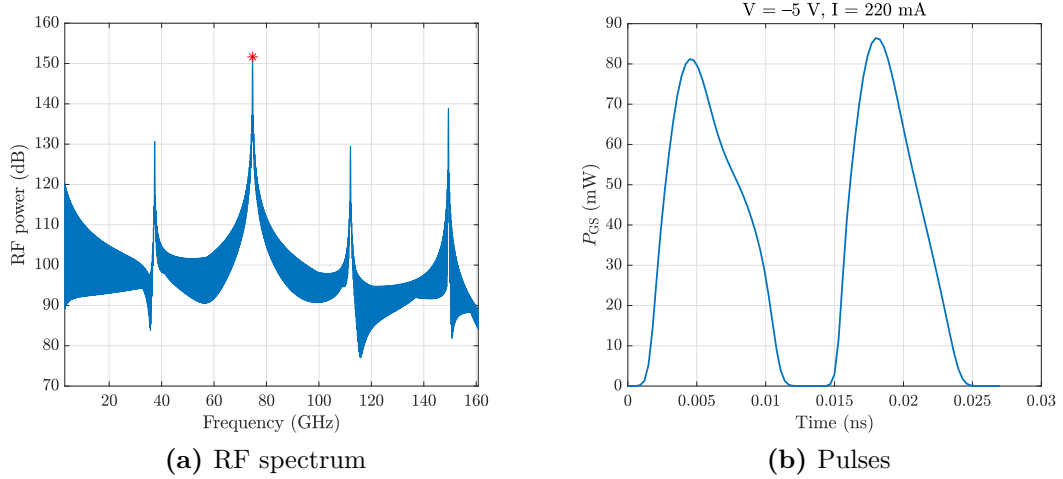


Figure 4.13: Frequency and time domain behavior for the chosen bias values.

The measured photocurrent for this 4-section device is higher than the ones obtained before ($\bar{I}_{ph} = 101.1$ mA), as well as both average ($P_{avg} = 3.96$ mW) and peak power ($P_{max} = 9.60$ mW) as reported in Figure 4.14.

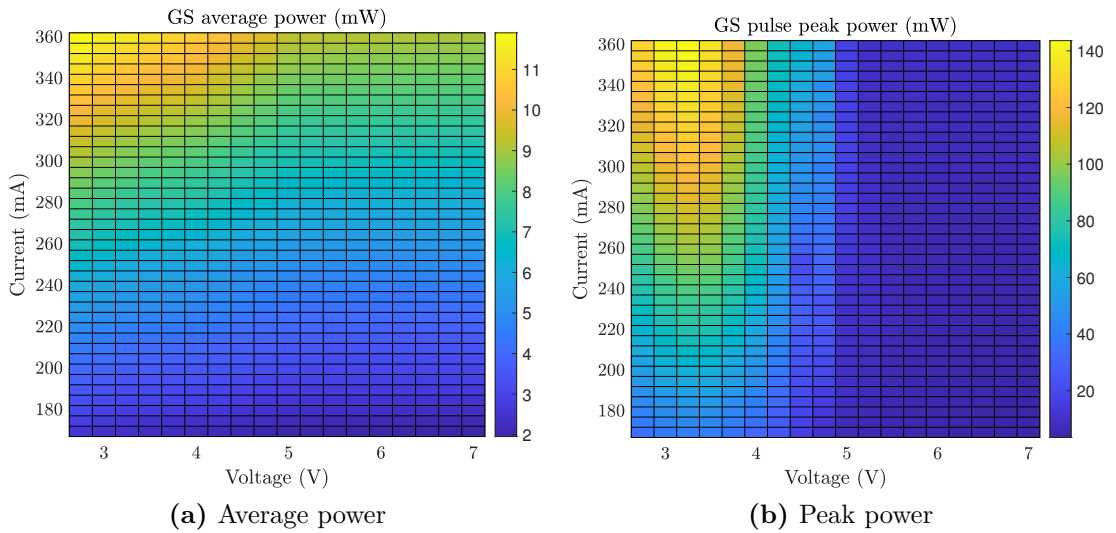


Figure 4.14: Average and peak power values in the considered bias range for the 4-section device.

2-section

Finally, the number of sections has been reduced to 2, thus implying a simple passive ML with no colliding pulses in the cavity. The target frequency is therefore the fundamental one, equal to $f = f_R = 75$ GHz and identified by the green regions in Figure 4.15. Here, two stable areas can be identified, with a low-voltage one that may be interesting for applications with tightly constrained reverse bias values.

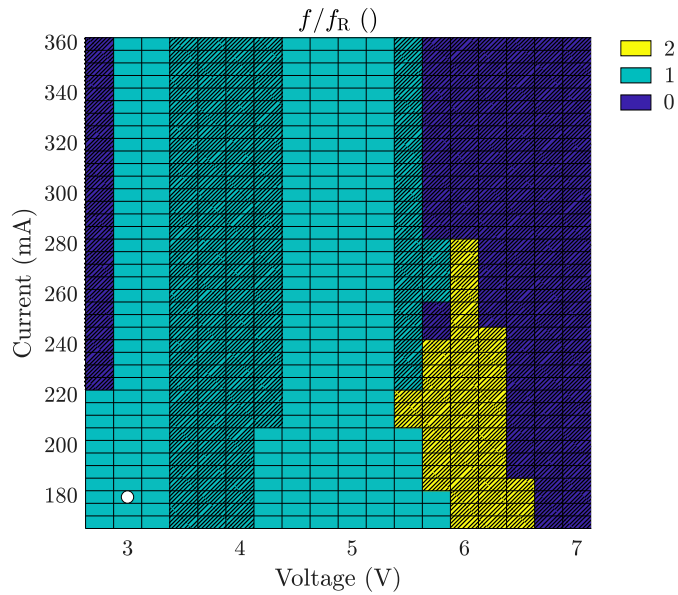


Figure 4.15: Repetition rate and stability, 2-section device. The marker highlights the chosen point for the following analysis.

The considerations on the bias values proposed when analyzing the 4-section devices remain valid, since the total cavity length is now 1/4 of the original one and therefore lower injection currents should be employed. Given the presence of the aforementioned stable region at low voltages, a reference point in this portion of the map has been chosen for the pulse analysis ($I = 180$ mA, $V = -3$ V), with a peak in the RF frequency at f_R (Figure 4.16a) and a single stable pulse in a round trip period, approximately 5.10 ps wide (Figure 4.16b).

Concerning the photocurrent, its value is lower than in the previous cases due to the choice of a smaller bias voltage ($\bar{I}_{ph} = 77.1$ mA). On the contrary, average ($P_{avg} = 8.62$ mW) and peak power ($P_{max} = 30.50$ mW) have the highest values as expected, and their map is shown in Figure 4.17.

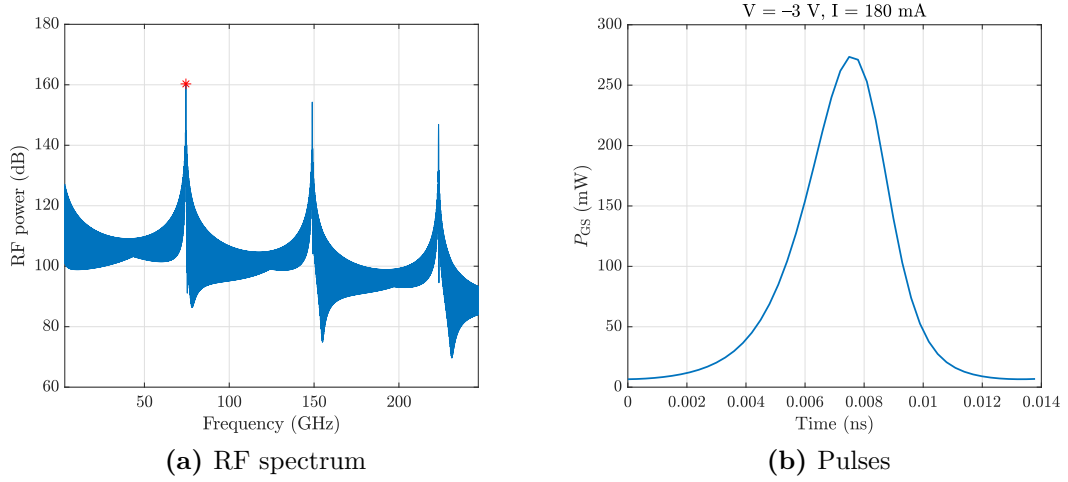


Figure 4.16: Frequency and time domain behavior for the chosen bias values.

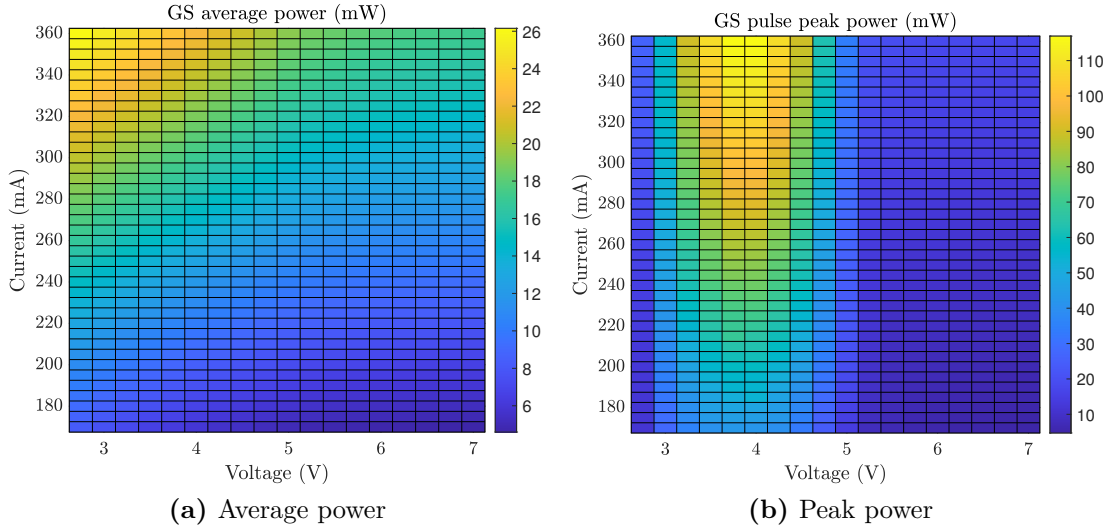


Figure 4.17: Average and peak power values in the considered bias range for the 2-section device.

10-section

The number of sections of which the device is composed is now increased to 10, hence reaching a total ring cavity length determined as

$$L = 5(L_{\text{gain}} + L_{\text{abs}}) = 5475 \mu\text{m}. \quad (4.13)$$

The fundamental repetition rate for this laser diode is $f_R = 15$ GHz, and the fifth harmonic has to be considered in order to obey the frequency requirement.

Differently from the previous cases, in which the cavity length has been decreased, a longer device would require higher injection current values to work properly. This can be clearly seen from Figure 4.18: the minimum current value for which the 10-section device reaches ML condition is approximately 240 mA. A rather wide bias range still allows to achieve a repetition rate at the fifth harmonic of the fundamental, as required.

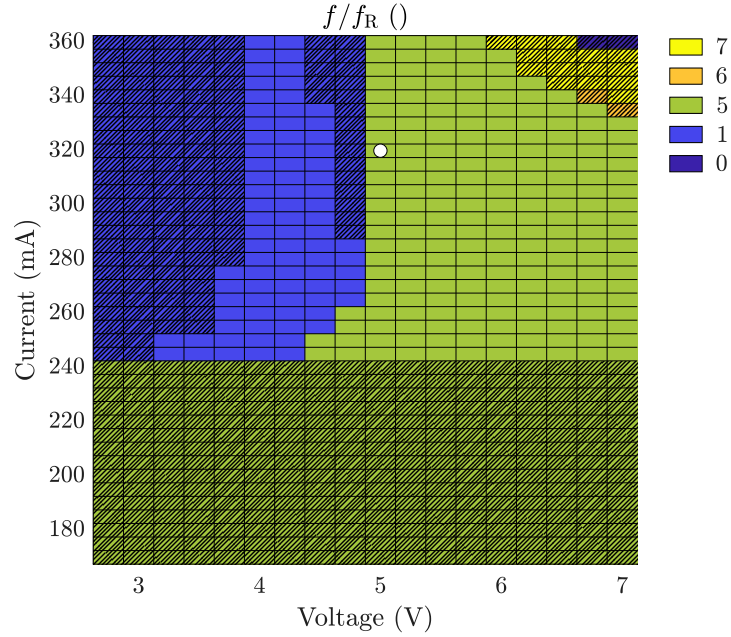


Figure 4.18: Repetition rate and stability, 10-section device. The marker highlights the chosen point for the following analysis.

The number of pulses in a single round trip period is correct, equal to 5 as expected from the RF spectrum peak (Figure 4.19a), and their differences in terms of peak value are due to the asymmetries in the simulated structure (Figure 4.19b) for the chosen bias values $I = 320$ mA, $V = -5$ V. Nevertheless, the result can be considered acceptable since no evident instability is visible, and the pulse width is quite narrow (3.57 ps).

To complete the characterization, the average photocurrent extracted from the SA sections is equal to $\bar{I}_{\text{ph}} = 131.7$ mA for this bias value, while average and maximum power are equal to $P_{\text{avg}} = 1.31$ mW and $P_{\text{max}} = 7.68$ mW, respectively. The complete power map for this device is reported in Figure 4.20.

12-section

Finally, a 12-section device has been simulated, with length

$$L = 6(L_{\text{gain}} + L_{\text{abs}}) = 6570 \mu\text{m}. \quad (4.14)$$

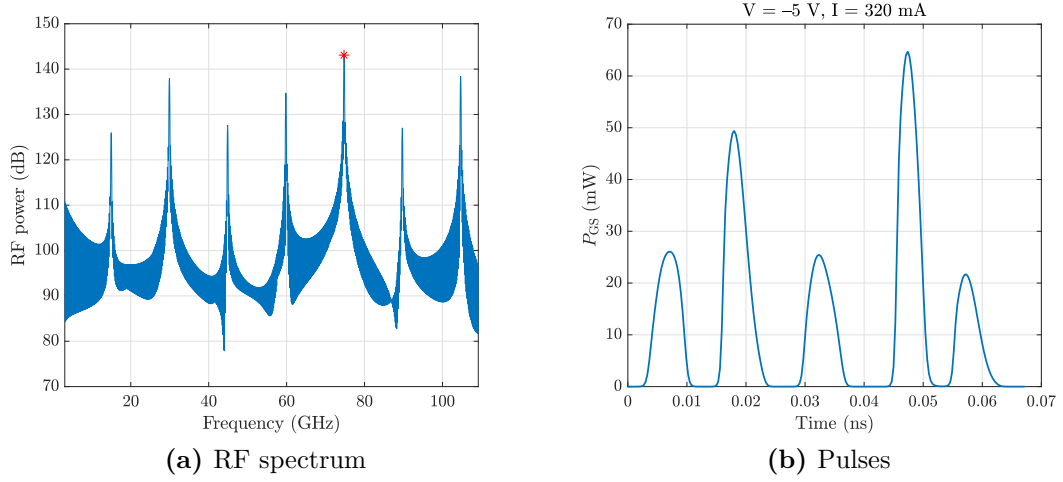


Figure 4.19: Frequency and time domain behavior for the chosen bias values.

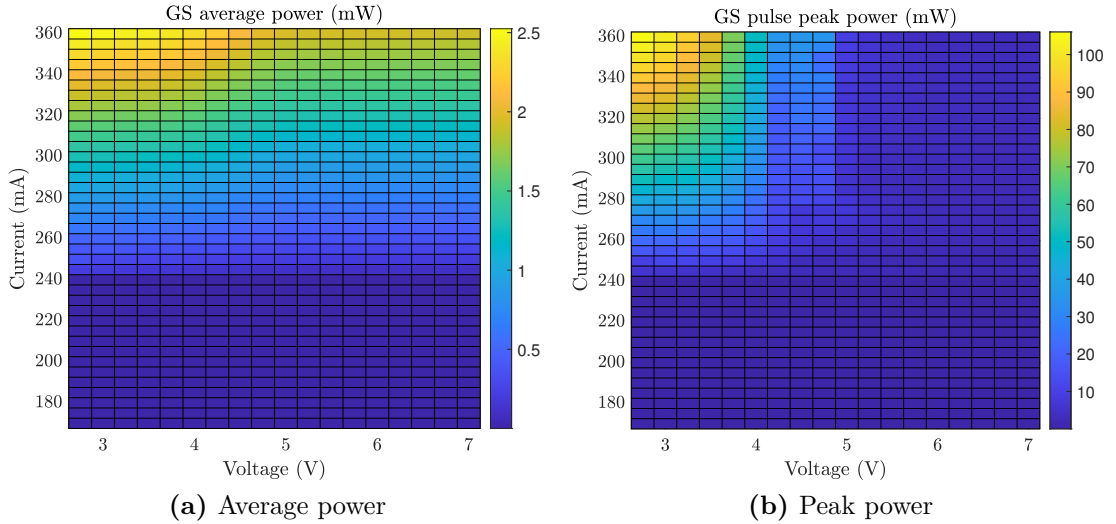


Figure 4.20: Average and peak power values in the considered bias range for the 10-section device.

This corresponds to a fundamental repetition rate $f_R = 12.5$ GHz, and the injection current required to achieve a harmonic mode locking at the sixth harmonic is rather large, as clearly visible in Figure 4.21.

A slightly higher bias voltage for the SA sections is required in order to obtain pulses narrow enough to be considered valid, whereas the current value is consistently larger than the previous cases. For these reasons, the pulses analysis has been performed in the case with $I = 350$ mA and $V = -5.25$ V. Six pulses are visible in Figure 4.22b, with width limited to 3.43 ps.

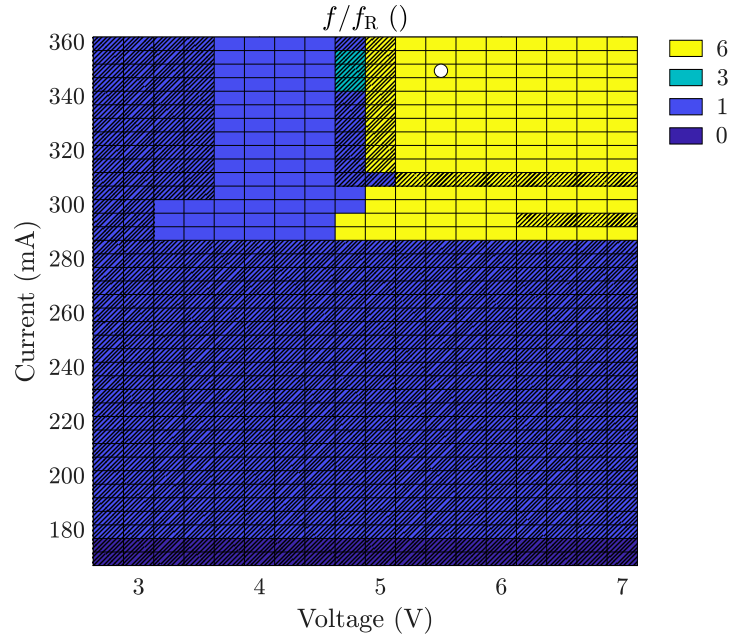


Figure 4.21: Repetition rate and stability, 12-section device. The marker highlights the chosen point for the following analysis.

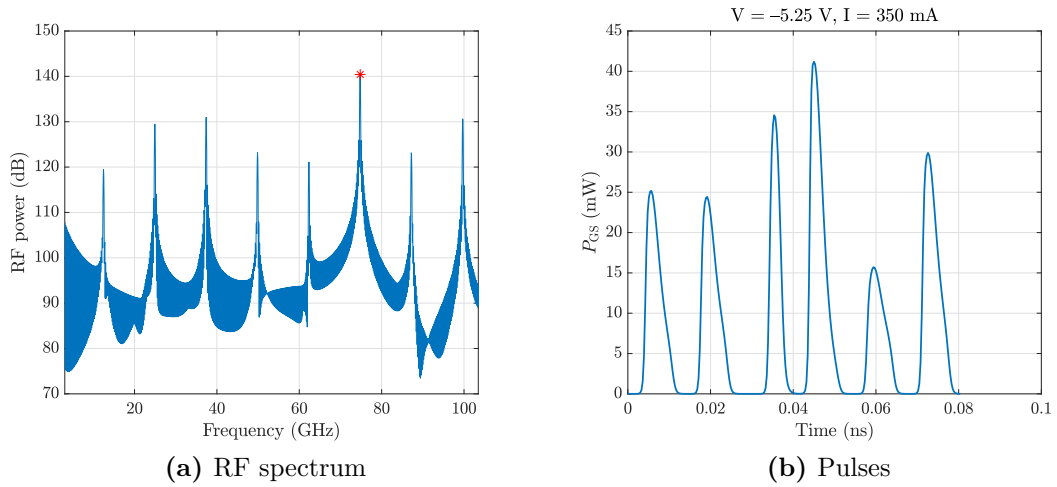


Figure 4.22: Frequency and time domain behavior for the chosen bias values.

The average photocurrent at the chosen bias point for the 12-section device is equal to $\bar{I}_{\text{ph}} = 124.0 \text{ mA}$. Concerning the power, both average ($P_{\text{avg}} = 0.94 \text{ mW}$) and maximum power ($P_{\text{max}} = 5.45 \text{ mW}$) are lower with respect to the previous cases (Figure 4.23).

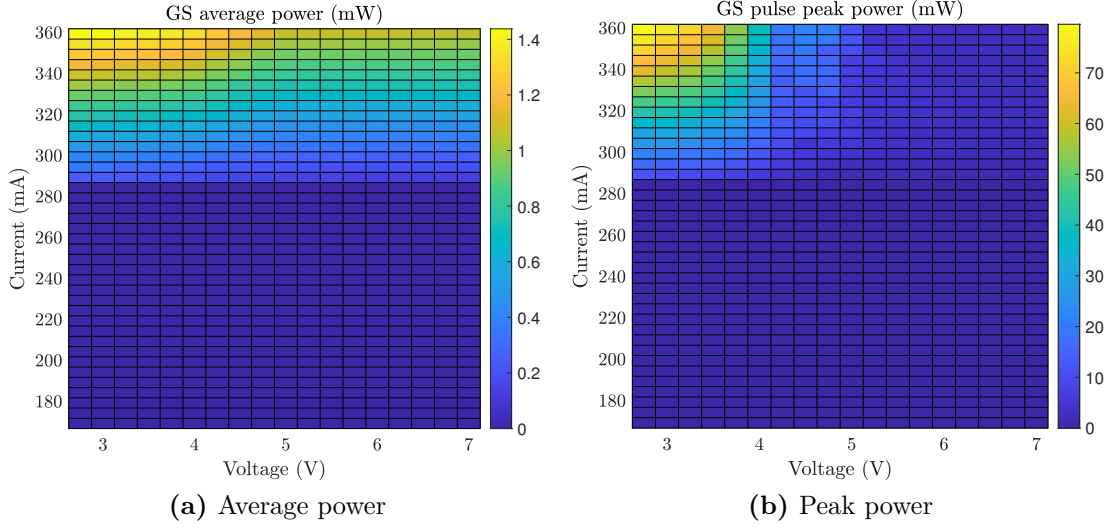


Figure 4.23: Average and peak power values in the considered bias range for the 12-section device.

4.1.4 8-section at higher repetition rate

If the number and length ratio of gain/SA couples is maintained as the original device, but the overall cavity length is reduced, a higher repetition rate can be achieved. In order to provide an example in this sense, a further structure has been simulated: it consists again of 8 sections, but their lengths are such that

$$L'_{\text{gain}} + L'_{\text{abs}} = \frac{L'}{4} = 730 \mu\text{m}, \quad (4.15)$$

again with a 23% $L_{\text{abs}} : L$ ratio. Since no other parameters have been modified, the expected repetition rate is

$$f = 4 \times f_{\text{R}} = 4 \times 28 \text{ GHz} = 112 \text{ GHz}. \quad (4.16)$$

The usual characterization has been carried out for this ring structure, with the main results in terms of frequency and ML stability reported in Figure 4.24. A rather wide tunability range can be identified at the desired output frequency, in particular at lower injection current levels with respect to the originally designed 8-section device due to the reduced length of the cavity in this case.

The reference point chosen for the pulses analysis is $I = 220 \text{ mA}$, $V = -5 \text{ V}$. From Figure 4.25 it can be noticed that 4 pulses are still present in the round trip period temporal window, but their width is clearly increasing (estimated to be around 4.28 ps) with respect to the original device. Such trend is actually typical

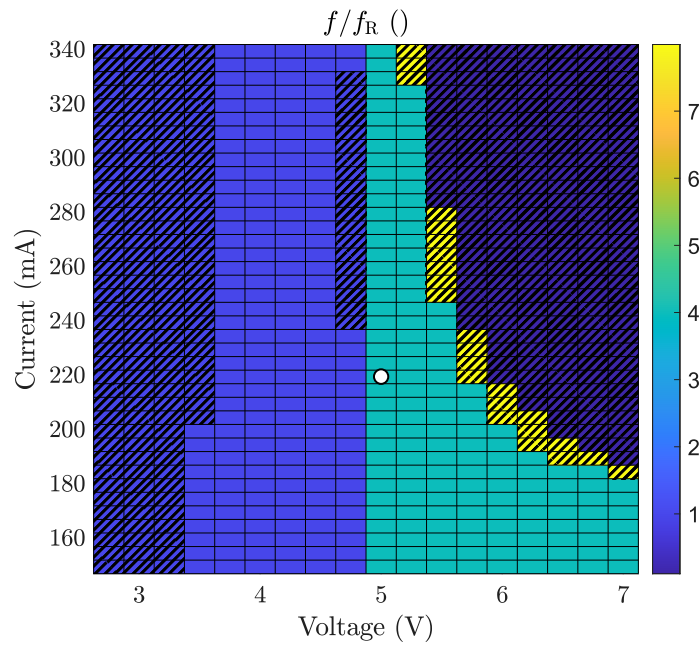


Figure 4.24: Repetition rate with respect to the fundamental one, with highlighted unstable regions.

when increasing the final repetition rate while keeping the same physical parameters as low-frequency samples: the recovery time is still sufficiently small to keep up the enhanced pulses frequency, but it should be further reduced in order to obtain similar results in terms of pulse width.

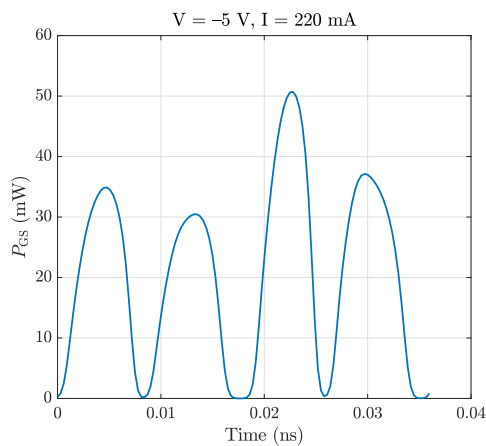


Figure 4.25: Pulses in the time domain within a round trip period.

In conclusion, the average photocurrent extracted is equal to $\bar{I}_{\text{ph}} = 121.5 \text{ mA}$, whereas average and peak power are $P_{\text{avg}} = 2.31 \text{ mW}$ and $P_{\text{max}} = 5.63 \text{ mW}$, respectively (Figure 4.26).

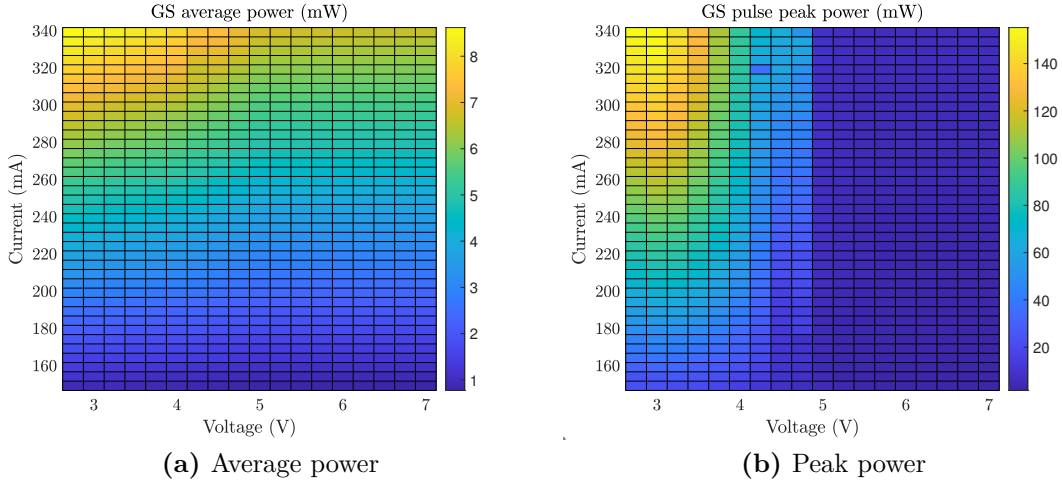


Figure 4.26: Average and peak power values in the considered bias range.

4.2 Fabry-Pérot lasers

As stated in Subsection 3.5.2, the MS-DDE model is thought for the simulation of unidirectional ring lasers. However, it is possible to exploit it for the analysis of Fabry-Pérot devices by simply considering an equivalent ring structure, obtained by taking into account the complete path that the light pulses follow along the cavity in a round trip period.

In the following, different types of edge-emitting devices are characterized in order to make a comparison with the previously introduced ring structures. Apart from a tapered 2-section laser, whose parameters have been taken from the literature in order to verify the applicability of this model to such devices, two examples of colliding pulse ML lasers are also presented. This can again represent the starting point for a design activity, involving FP lasers in ML condition to achieve high repetition rate pulse trains.

4.2.1 MS-DDE modeling of edge-emitting structures

An example of basic 2-section FP laser and its equivalent ring structure is reported in Figure 4.27. At the reference section $z = 0$, where the first edge of the device is located (and R_0 is its associated power reflectivity), the first slice can be found

identified by the number 1. Moving rightwards, the traveling pulses encounter active region slices marked with an increasing number until they reach the SA section. At the end of it, the light bounces back due to the presence of a second edge (power reflectivity R_L) located at section $z = L$: from now on, it propagates in the opposite direction returning to section $z = 0$ or, equivalently, it can be thought of going straight on along the second part of the ring cavity (with total length $2L$), symmetrical with respect to the previous one.

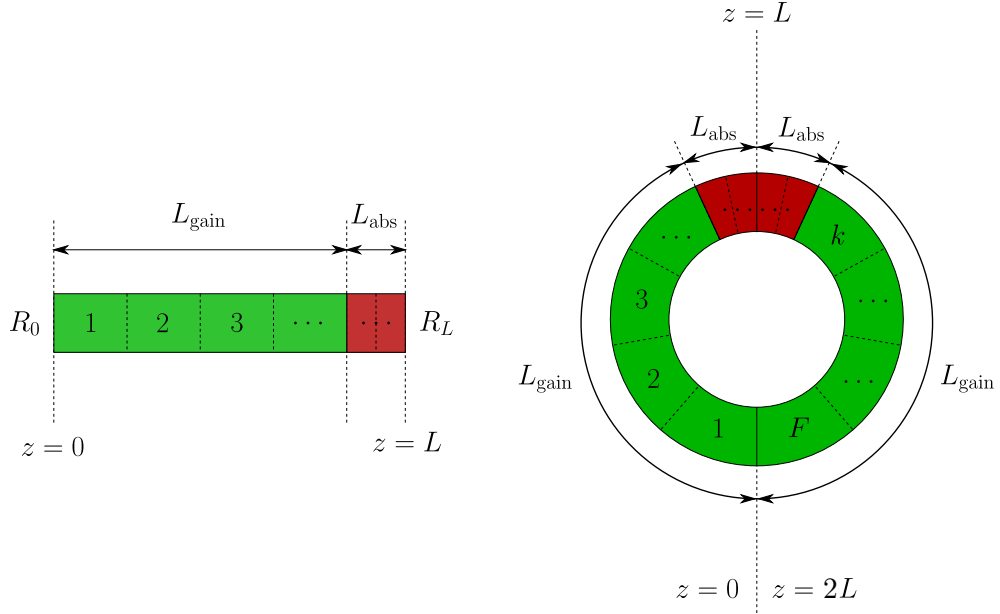


Figure 4.27: Basic FP and equivalent ring structures analyzed with the proposed MS-DDE model.

Notice that the overall non-saturable losses experienced by the field over a round trip must be the same in the two structures. In previous DDE models [109, 110], this was ensured by considering a lumped power attenuation factor K localized at the reference section $z = 0$, i.e.

$$K = R_0 R_L \exp(-\alpha_i L). \quad (4.17)$$

With this approach, the SA section would be forced to be located just before or after the section $z = 0$, where non-saturable losses are introduced.

In the MS-DDE model, though, the non-saturable losses can be distributed between any two adjacent cavity slices. This also allows to lift the limitations on the SA position, which can be placed at any section of the cavity (also enabling the colliding pulse regime to be modeled). The loss coefficients M_k introduced in

the round trip gain evaluation (Equation 3.60) then become

$$M_k = \begin{cases} \sqrt{R_0} \exp\left(-\frac{\alpha_i}{2} L_F\right) & k = F \\ \sqrt{R_L} \exp\left(-\frac{\alpha_i}{2} L_{F/2}\right) & k = F/2 \\ \exp\left(-\frac{\alpha_i}{2} L_k\right) & k \neq F/2, F \end{cases}, \quad (4.18)$$

where the number of slices F must be even.

4.2.2 20 GHz, tapered gain section

In order to verify the applicability of the MS-DDE model to describe tapered edge-emitting structures, an example of device has been taken from the literature [97]. In particular, the chosen device is the one presented in Figure 4.28, characterized by the following features.

- Total cavity length $L = 2048 \mu\text{m}$, corresponding to a fundamental repetition rate $f_R = 20 \text{ GHz}$.
- SA section length equal to 5% of the total cavity, i.e. $L_{\text{abs}} = 102.4 \mu\text{m}$.
- Ridge width of the device monotonically tapered from $3 \mu\text{m}$ to $6 \mu\text{m}$.
- Active region consisting of a five-layer chirped InAs/InGaAs dots-in-a-well.
- Intrinsic waveguide losses $\alpha_i = 6 \text{ cm}^{-1}$.
- Mirror losses $\alpha_m = 5.6 \text{ cm}^{-1}$.
- Material gain $g = 12.4 \text{ cm}^{-1}$.

Among the features presented in the aforementioned article, the average output power can be exploited to perform a direct comparison with the results obtained by using the MS-DDE model. A good agreement between the two maps can be seen in Figure 4.29.

The possibility to properly simulate tapered structures is rather interesting, since edge-emitting ML laser diodes with flared waveguides have shown promising results in terms of high output power and ultrashort pulse width [86]. In particular, the tapered section is able to deliver high power when increasing its width, without impairing the optical signal quality, and such optimization can be exploited also in harmonic ML devices [121].

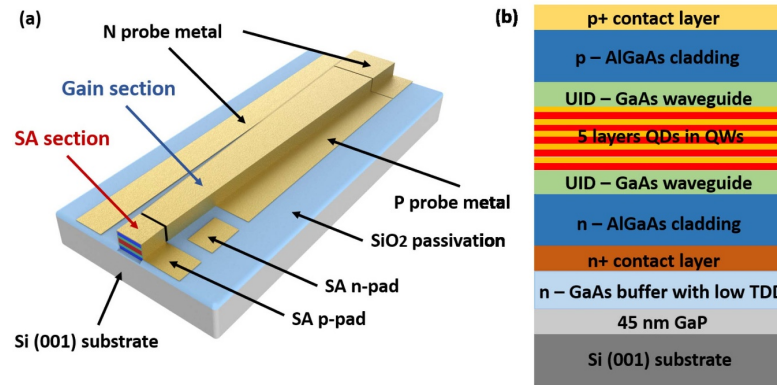
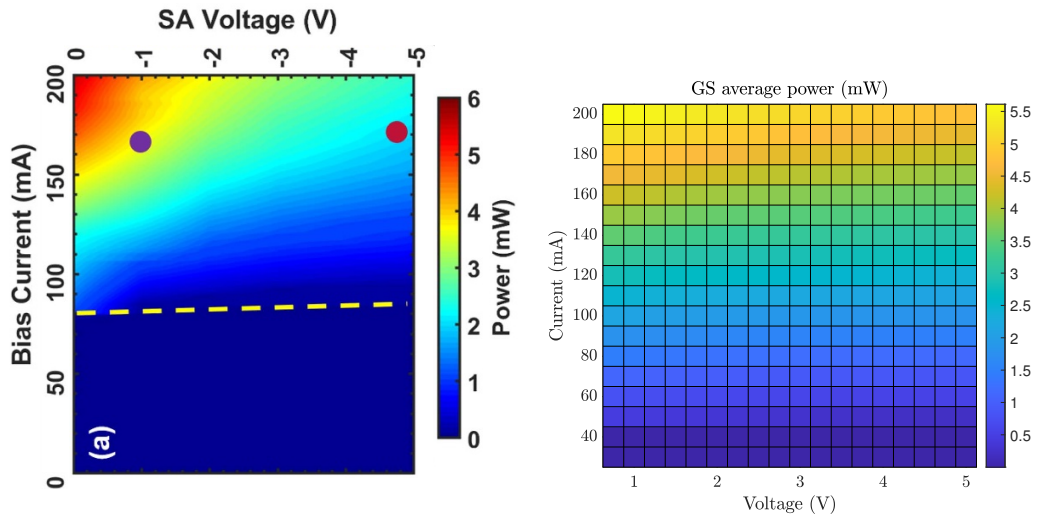


Figure 4.28: Reference structure for the tapered FP analysis [97].



(a) Original results [97]

(b) Results obtained with the MS-DDE model

Figure 4.29: Average output power of the tapered device.

4.2.3 Five-section devices

Similarly to the case of ring devices, an example of edge-emitting laser in harmonic ML condition has been designed to work at repetition rates in the order of tens of GHz. In this case, two different implementations are proposed, only changing the total cavity length (and therefore the achieved repetition rate). The remaining parameters, which are considered to be fixed, are reported in Table 4.2.

In FP lasers, harmonic mode locking is also referred to as colliding pulse ML, since the pulses actually collide in the SA sections of the device (differently from the ring laser case, in which unidirectionality has been assumed). Here, a 5-section FP device is simulated, with the external active region characterized by a length equal to $L_{\text{gain}}/2$. In this way, the equivalent ring will consist of 8 sections, as reported in

Symbol	Description	Value
d	Ridge waveguide width	$6 \mu\text{m}$
α_i	Intrinsic waveguide losses	1.5 cm^{-1}
Γ_y	Transversal confinement factor	75%
Γ_x	Vertical confinement factor	10%
n_r	Refractive index	3.66
η_i	Internal quantum efficiency	85%
h_{SCH}	SCH height	180 nm
h_{QW}	QW height	7 nm
h_{QD}	QD height	5 nm
N_l	QD layers	12
N_D	QD surface density	$2.85 \times 10^{10} \text{ cm}^{-2}$
R_{QD}	QD radius	15.5 nm
ΔE^{inh}	FWHM inhomogeneous broadening	34 meV
$E_{(e-h),\text{GS}}$	GS interband transition energy	0.9904 eV
$E_{(e-h),\text{ES1}}$	ES1 interband transition energy	1.0597 eV
$\tau_{c,\text{GS}}$	GS capture time	0.3 ps
$\tau_{c,\text{ES1}}$	ES1 capture time	0.3 ps
V_{bi}	Built-in potential	0.8 V

Table 4.2: Main physical parameters used in the simulation of the FP device [18].

Figure 4.30, hence the expected repetition rate is at 4 times the fundamental one.

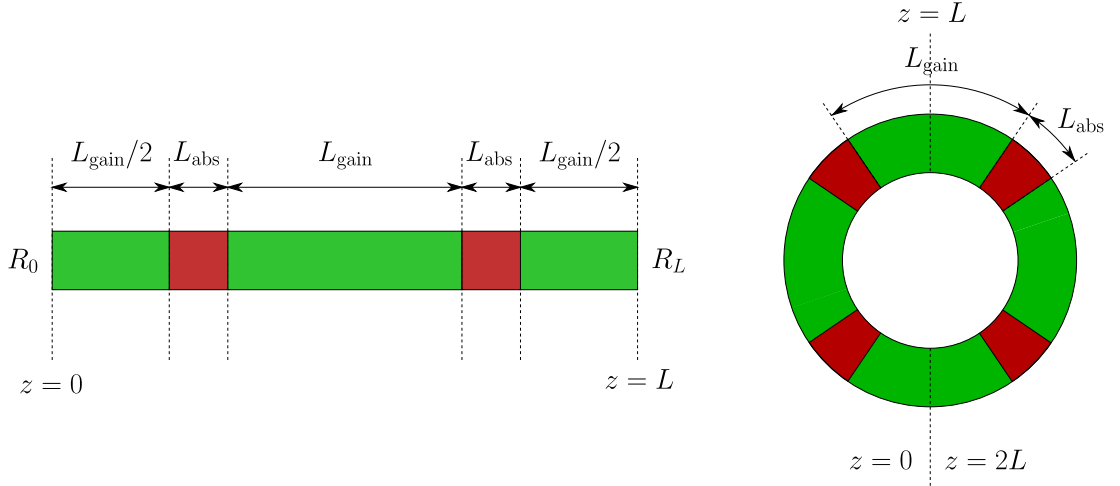


Figure 4.30: 5-section FP (left) and equivalent ring structure (right) analyzed with the proposed MS-DDE model.

64 GHz operation

Promising results have been obtained by choosing gain and SA sections lengths as follows (see Section A.2 for the corresponding MATLAB code):

$$\begin{cases} L_{\text{gain}} = 960 \mu\text{m} \\ L_{\text{abs}} = 320 \mu\text{m} \end{cases} \quad (4.19)$$

The total FP cavity length is therefore equal to $L = 2560 \mu\text{m}$, whereas the equivalent ring one is twice this value. The fundamental repetition rate of the cavity and the expected output one can then be derived as

$$f_{\text{R}} = \frac{v_{\text{g}}}{2L} = 16 \text{ GHz} \implies f = 4 \times f_{\text{R}} = 64 \text{ GHz}. \quad (4.20)$$

In Figure 4.31 the obtained repetition rate values, normalized to the fundamental one, can be seen as a function of the bias voltage and current. As for the ring devices, also in this case the regions characterized by instability according to Haus criterion [105] are identified with black oblique lines. The tunability range for this device appears to be rather wide, and the gain current and SA voltage values have to be chosen in such a way that stable ML operation is ensured.

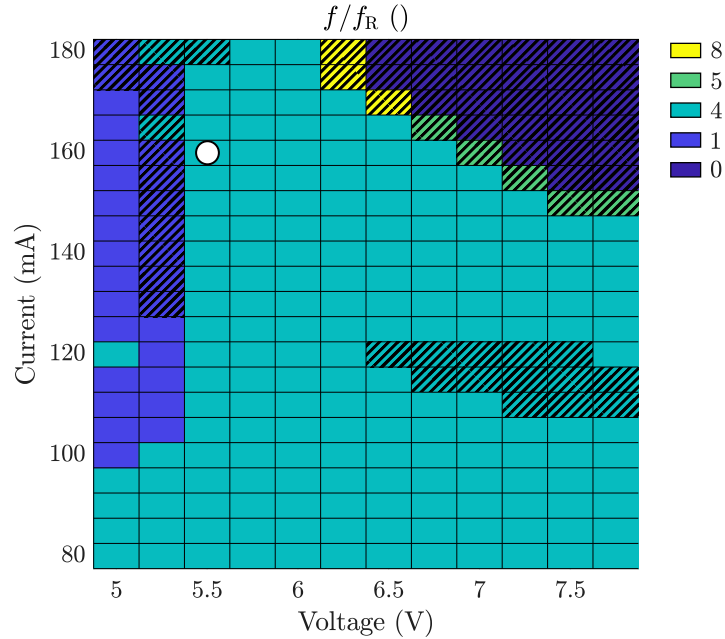


Figure 4.31: Repetition rate and stability.

The chosen bias point for the pulses analysis is characterized by injection current $I = 160 \text{ mA}$ and reverse SA voltage $V = -5.5 \text{ V}$. The corresponding peak value in

the RF spectrum is correctly located at the fourth harmonic of the fundamental cavity frequency (Figure 4.32a), with four stable pulses in a round trip period as shown in Figure 4.32b. The estimated autocorrelation pulse width is 3.92 ps.

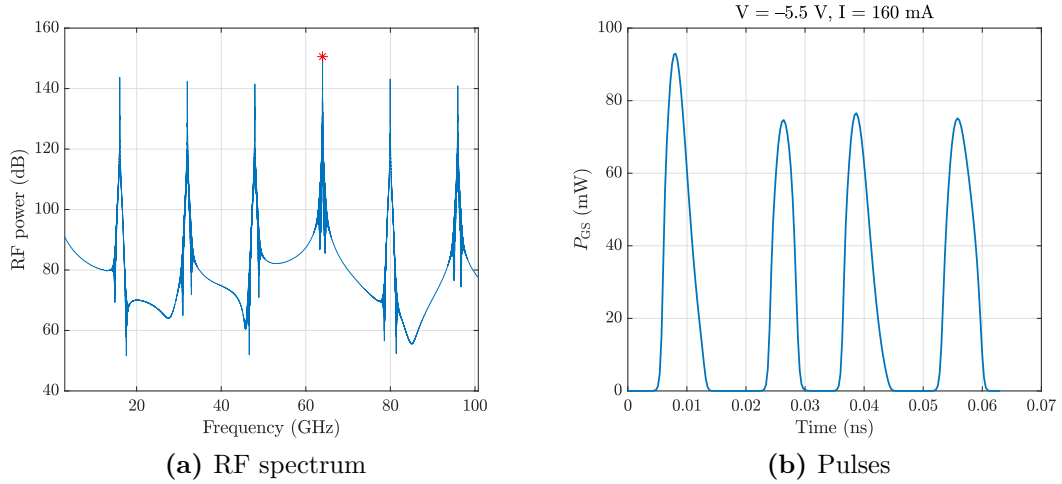


Figure 4.32: Frequency and time domain behavior for the chosen bias values.

Concerning the other figures of merit of the device, the average photocurrent extracted from the SA sections has been estimated to be $\bar{I}_{ph} = 286.0$ mA. This value is significantly higher with respect to the ones found in the case of ring devices, as it is the maximum power value ($P_{max} = 25.84$ mW), whereas the average power is almost unchanged ($P_{avg} = 2.52$ mW). The complete maps for average and peak power are shown in Figure 4.33.

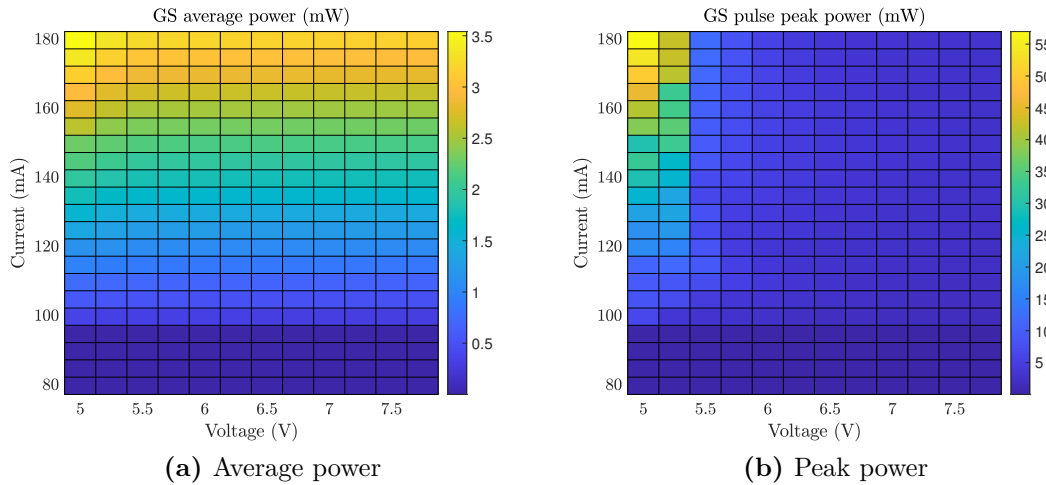


Figure 4.33: Average and peak power values in the considered bias range.

85 GHz operation

The total cavity length has then been reduced to $L = 1920 \mu\text{m}$ without changing the ratio between gain and SA sections lengths, which are therefore equal to

$$\begin{cases} L'_{\text{gain}} = 720 \mu\text{m} \\ L'_{\text{abs}} = 240 \mu\text{m} \end{cases} \quad (4.21)$$

With this choice, the fundamental repetition rate becomes $f'_R = 21.25 \text{ GHz}$, leading to a $f' = 4 \times f'_R = 85 \text{ GHz}$ output frequency.

The results obtained in terms of repetition rate and stability when simulating the shorter FP laser are shown in Figure 4.34. The bias window has not been changed with respect to the initial case, so the tunability range seems to be rather narrow, but one should recall that by reducing the total cavity length the required injection current is reduced, too: other working points at lower I values can therefore be found in addition to the ones already visible in the proposed map.

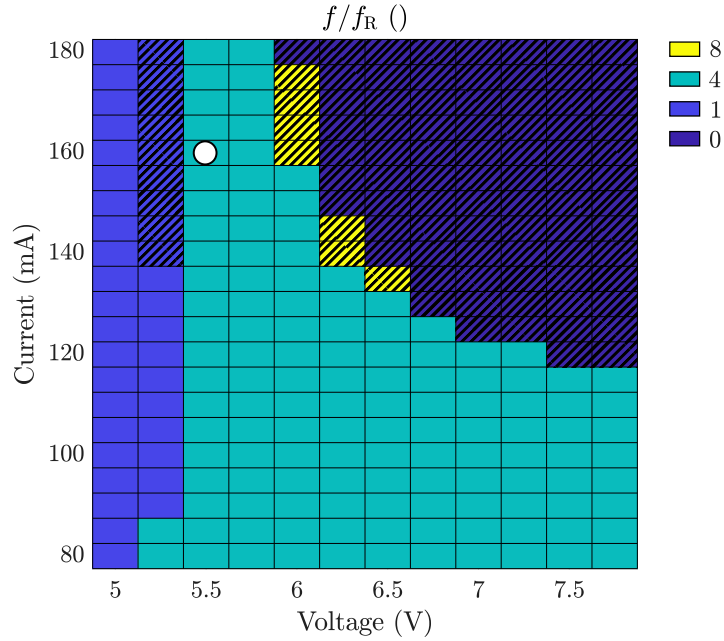


Figure 4.34: Repetition rate and stability.

The RF spectrum obtained for $I = 160 \text{ mA}$ and $V = -5.5 \text{ V}$ exhibits a peak at four times the fundamental repetition rate as expected (Figure 4.35a). Four peaks are visible in the time trace reported in Figure 4.35b, and they appear to be slightly wider with respect to the ones obtained at lower frequency. This is confirmed by evaluating the autocorrelation pulse width, equal in this case to 4.40 ps .

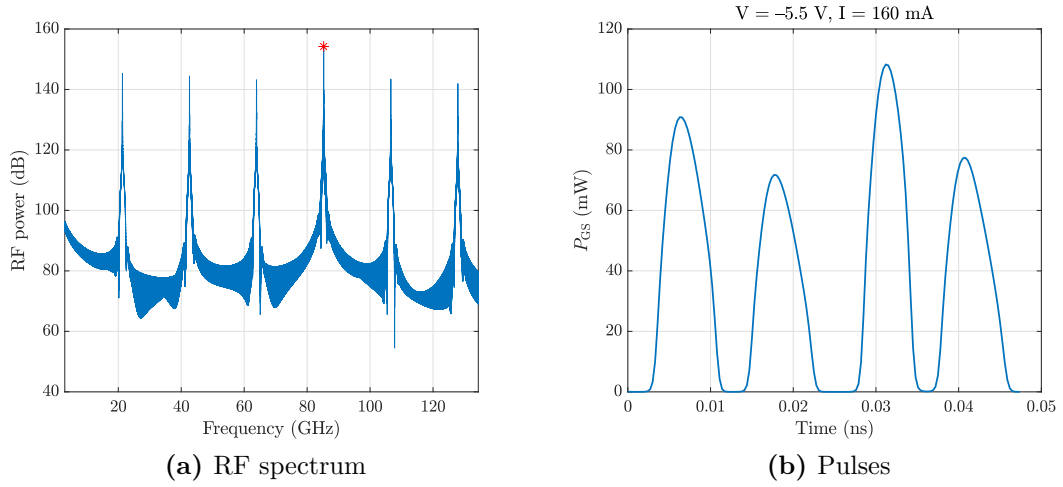


Figure 4.35: Frequency and time domain behavior for the chosen bias values.

Finally, the average photocurrent extracted from the SA sections has been estimated to be $\bar{I}_{ph} = 267.8$ mA, similarly to the results obtained with the longer FP cavity. Concerning the optical output power for the chosen bias point, the values $P_{avg} = 4.22$ mW and $P_{max} = 19.55$ mW have been obtained for the average and peak values, respectively. Figure 4.36 reports the complete bias map for these last two figures of merit.

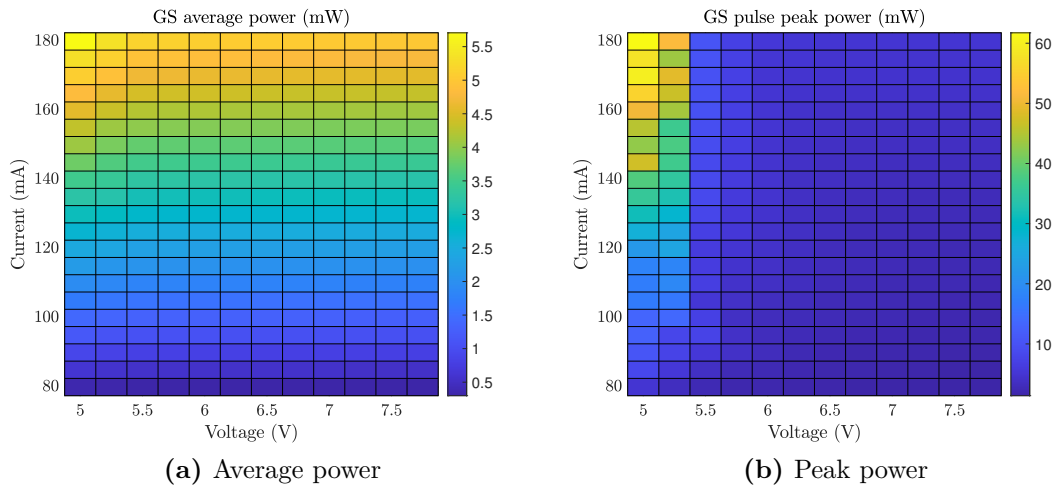


Figure 4.36: Average and peak power values in the considered bias range.

Chapter 5

Conclusions

5.1 Final considerations

At the end of this research activity, some concluding remarks are provided to outline what have been the most relevant outcomes of the Thesis, alongside possible future steps that can be followed along this path.

5.1.1 Main outcomes

Even though the topic of QD-based semiconductor lasers is widely investigated in the literature, finding a complete mathematical description that links the material behavior to the classical waveguide theory can turn out to be a hard task. The theoretical framework presented in Chapters 2 and 3 of this Thesis aims at providing a simplified but self-consistent explanation of the basic phenomena behind these devices' macroscopic behavior, fundamental for their description and subsequent numerical simulation. This analysis has represented the first step of the research activity, starting from the thorough analytical description provided by Mattia Rossetti in his PhD Thesis and expanding it by introducing some auxiliary considerations required to understand all the model's features.

A pre-existing version of the MATLAB program for MS-DDE modeling of passively mode-locked QD laser diodes has instead represented the starting point for the simulation activities. In this case, though, the code has been heavily rewritten in order to improve its computational efficiency while including additional features to be modeled. Concerning the first goal, the simulation times obtained with the new code turned out to be almost one order of magnitude lower when compared to the original ones, thus representing an interesting improvement from an application perspective. In addition to this, the current version of the program allows to model harmonic ML in multi-section devices too, and it has been tested on a wide variety of FP and ring lasers to assess its flexibility. Notice that

understanding the physical mechanisms mentioned previously has represented an essential step in order to perform these optimizations.

Much effort has then been aimed at the identification of a parameters set allowing to achieve a stable harmonic mode locking regime, both in the case of ring-shaped and edge-emitting structures. This has actually represented the major challenge of the whole work, given the absence of complete datasets in the literature that would have provided a starting point for the simulation activities, as well as the interdependence among key design parameters that has required massive parametric simulations as a function of external bias and/or structural features.

Concerning the final results of this analysis, some key performance indicators describing the device behavior have been extracted, from which a set of design rules for these innovative devices can be obtained. The MS-DDE model can therefore be seen as a practical tool for the feasibility assessment of QD based laser sources working in passive or harmonic mode locking regimes, with a possible practical usage in the early stages of a design process for these types of devices since providing accurate results with a reduced time overhead with respect to other approaches.

5.1.2 Next steps

Apart from the functionalities reported in this document, the MS-DDE program also includes additional features that have not been directly used yet, but they may represent valuable assets for subsequent research works. As an example, it is possible to verify the behavior of a device lifting the excitonic assumption: the portion of code able to perform these computations has been rewritten in the optimization phase of the Thesis, but this functionality has not been used in the presented work. Moreover, the possibility of introducing an external cavity (providing optical feedback) or moving the electrical signal extraction point along the cavity have also been included in the program, with no immediate usage in the analysis of the devices presented in this Thesis.

In the medium-long term, the current version of the program could be employed in the preliminary design phase for the optimization of RF devices with embedded QD lasers, working in both passive or harmonic ML conditions. Some joint activities focused on these topics have already started, involving other research groups.

Appendix A

MATLAB Codes

A.1 8-section ring laser (75 GHz)

```
%% Geometry
% 'Ring' -> ring laser
data.CavityType='Ring';
% Section lengths (um) Positive -> active section, negative -> ...
  absorption section
data.Lengths=[140,-85,280,-85,280,-85,280,-85,140]*3;
% Nuber of slices used to divide the sections
data.Slices=[4,2,8,2,8,2,8,2,8,2,4];
% Waveguide width (um) (function of z or scalar)
data.Func_d=6;

%% Confinement factors
% Confinement factor in the transversal direction (y) (function of z...
  or scalar)
data.Func_gamma_trasv=0.75;
% Confinement factor in the vertical direction (x) (function of z or...
  scalar)
data.Func_gamma_x=0.1;

%% Reflectivities - Ring structure
% In a Ring configuration, only K_Laser is present, indicating the ...
  amount of power that remains in the device
% 10% of the power is extracted, 90% remains in the cavity ()
data.K_Laser=0.9;

%% Losses
% Include field losses
data.IncludeLosses=true;
% Power intrinsic waveguide losses (cm^-1) (function of z or scalar)
data.Func_alfai=1.5;
```

```

%% Other parameters
% Self Phase Modulation effect scaling factor (0 -> not included)
data.IncludeSPM=0.2;
% Effective refractive index ()
data.nr=3.66;
% Internal quantum efficiency ()
data.etai=0.85;

%% Global parameters
% Temperature (K)
data.T=293;
% Number of dot layers ()
data.NumLayers=12;
% Dot surface radius (um)
data.Rdots=15.5e-3;
% Built-in voltage (V)
data.Vbi=-0.8;

%% Structural parameters
% Dot layer height (um)
data.H_QD=5e-3;
% Wetting Layer height (um)
data.H_WL=7e-3;
% Separate Confinement Heterostructure height (um)
data.H_SCH=180e-3;

%% Dot parameters
% Non-radiative recombination time in CB (ns)
data.tnr=[1;1;1e50;1e50;1e50];
% Capture time in CB (ns)
data.tc=[0.3;0.3;0.3;0.3]*1e-3;
% Auger recombination time at T=300K (ns)
data.tAu300K=[1e50;0.22*2.5;0.22*2.5;0.22]*3*0.75;
% Degeneracy in CB ()
data.Degeneracy=[6;4;2];
% QD density (um^-2)
data.Nd=2.85e2;
% Number of excited states considered in CB ()
data.NumES=2;
% Energy levels ES2, ES1, GS (eV)
data.E=[1.106;1.0597; 0.9986];
% WL energy gap (eV)
data.WLenergygap=1.1539;
% SCH energy gap (eV)
data.SCHenergygap=1.2797;
% Energy difference between CB levels (eV)
data.DeltaE=[(data.SCHenergygap-data.WLenergygap)*0.7; ...
             (data.WLenergygap-data.E(1))*0.77;-diff(data.E)];

```

A.2 8-section edge-emitting laser (64 GHz)

```

%% Geometry
% 'FP' -> edge-emitting laser
data.CavityType='FP';
% Section lengths (um) Positive -> active section, negative -> ...
%   absorption section
data.Lengths=[120 -80 240 -80 120]*4;
% Nuber of slices used to divide the sections
data.Slices=[8,4,16,4,8];
% Waveguide width (um) (function of z or scalar)
data.Func_d=6;

%% Confinement factors
% Confinement factor in the transversal direction (y) (function of z...
%   or scalar)
data.Func_gamma_trasv=0.75;
% Confinement factor in the vertical direction (x) (function of z or...
%   scalar)
data.Func_gamma_x=0.1;

%% Reflectivities - Edge-emitting structure
% In a FP laser, the two facets reflectivities must be provided, ...
%   while K_Laser is determined according to the chosen output facet
% Power reflectivity at the left facet ()
data.Rleft=0.99;
% Power reflectivity at the right facet ()
data.Rright=0.9;
% Output extraction facet
data.OutputFromRightFacet=true;

%% Losses
% Include field losses
data.IncludeLosses=true;
% Power intrinsic waveguide losses (cm^-1) (function of z or scalar)
data.Func_alfai=1.5;

%% Other parameters
% Self Phase Modulation effect scaling factor (0 -> not included)
data.IncludeSPM=0.2;
% Effective refractive index ()
data.nr=3.66;
% Internal quantum efficiency ()
data.etai=0.85;

%% Global parameters
% Temperature (K)
data.T=293;

```

```

% Number of dot layers ()
data.NumLayers=12;
% Dot surface radius (um)
data.Rdots=15.5e-3;
% Built-in voltage (V)
data.Vbi=-0.8;

%% Structural parameters
% Dot layer height (um)
data.H_QD=5e-3;
% Wetting Layer height (um)
data.H_WL=7e-3;
% Separate Confinement Heterostructure height (um)
data.H_SCH=180e-3;

%% Dot parameters
% Non-radiative recombination time in CB (ns)
data.tnr=[1;1e50;1e50;1e50];
% Capture time in CB (ns)
data.tc=[0.3;0.3;0.3;0.3]*1e-3;
% Auger recombination time at T=300K (ns)
data.tAu300K=[1e50;0.22*2.5;0.22*2.5;0.22]*3*0.75;
% Degeneracy in CB ()
data.Degeneracy=[6;4;2];
% QD density (um^-2)
data.Nd=2.85e2;
% Number of excited states considered in CB ()
data.NumES=2;
% Energy levels ES2, ES1, GS (eV)
data.E=[1.106;1.0597; 0.9986];
% WL energy gap (eV)
data.WLenergygap=1.1539;
% SCH energy gap (eV)
data.SCHenergygap=1.2797;
% Energy difference between CB levels (eV)
data.DeltaE=[(data.SCHenergygap-data.WLenergygap)*0.7; ...
(data.WLenergygap-data.E(1))*0.77;-diff(data.E)];

```

Acronyms

AM Amplitude Modulation
AML Active Mode Locking

BPF Band-Pass Filter
BW BandWidth

CB Conduction Band
CML Colliding pulse Mode Locking
CW Constant Wavelength

DBR Distributed Bragg Reflector
DDE Delayed Differential Equation
DHS Double HeteroStructure
DOS Density Of States
DWELL Dots-in-a-Well

ES Excited State
EOM Electro-Optic Modulator

FP Fabry-Pérot
FM Frequency Modulation
FROG Frequency Resolved Optical Gating
FSR Free Spectral Range
FWHM Full Width at Half Maximum
FWM Four-Wave Mixing

GS Ground State

HML Hybrid Mode Locking

LASER Light Amplification by Stimulated Emission of Radiation

MBE Molecular Beam Epitaxy
ML Mode Locking

MOCVD Metal Organic Chemical Vapor Deposition

OFC Optical Frequency Comb

OTDM Optical Time Division Multiplexing

PML Passive Mode Locking

QCSE Quantum-Confined Stark Effect

QD Quantum Dot

QW Quantum Well

RF Radio Frequency

SA Saturable Absorber

SCH Separate Confinement Heterostructure

SCP Self-Consistent Pulse

SiP Silicon Photonics

SML Self Mode Locking

SPM Self-Phase Modulation

TBP Time-Bandwidth Product

TDTW Time-Domain Traveling-Wave

TE Transverse Electric

TM Transverse Magnetic

VB Valence Band

WDM Wavelength Division Multiplexing

WL Wetting Layer

Bibliography

- [1] R. G. Gould et al. «The LASER, light amplification by stimulated emission of radiation». In: *The Ann Arbor conference on optical pumping, the University of Michigan*. Vol. 15. 128. 1959, p. 92 (cit. on p. 1).
- [2] M. Grundmann. *Nano-optoelectronics: concepts, physics and devices*. Springer Science & Business Media, 2002 (cit. on p. 1).
- [3] Z. I. Alferov. «Nobel Lecture: The double heterostructure concept and its applications in physics, electronics, and technology». In: *Reviews of modern physics* 73.3 (2001), p. 767 (cit. on p. 2).
- [4] H.-J. Song et al. «Present and future of terahertz communications». In: *IEEE transactions on terahertz science and technology* 1.1 (2011), pp. 256–263 (cit. on p. 5).
- [5] M. Fujishima. «Key technologies for THz wireless link by silicon CMOS integrated circuits». In: *Photonics*. Vol. 5. 4. Multidisciplinary Digital Publishing Institute. 2018, p. 50 (cit. on pp. 5, 6).
- [6] J. Federici et al. «Review of terahertz and subterahertz wireless communications». In: *Journal of Applied Physics* 107.11 (2010), p. 6 (cit. on p. 5).
- [7] R. Piesiewicz et al. «Scattering analysis for the modeling of THz communication systems». In: *IEEE Transactions on Antennas and Propagation* 55.11 (2007), pp. 3002–3009 (cit. on p. 5).
- [8] H.-H. Chen. *The next generation CDMA technologies*. John Wiley & Sons, 2007 (cit. on p. 5).
- [9] R. Piesiewicz et al. «THz channel characterization for future wireless gigabit indoor communication systems». In: *Terahertz and Gigahertz Electronics and Photonics IV*. Vol. 5727. International Society for Optics and Photonics. 2005, pp. 166–176 (cit. on p. 5).
- [10] D. Saeedkia et al. «Terahertz photonics: Optoelectronic techniques for generation and detection of terahertz waves». In: *Journal of Lightwave Technology* 26.15 (2008), pp. 2409–2423 (cit. on p. 6).

-
- [11] C. T. Brown et al. «Compact laser-diode-based femtosecond sources». In: *New Journal of Physics* 6.1 (2004), p. 175 (cit. on p. 6).
- [12] C. J. Panagamuwa et al. «Frequency and beam reconfigurable antenna using photoconducting switches». In: *IEEE Transactions on Antennas and Propagation* 54.2 (2006), pp. 449–454 (cit. on p. 6).
- [13] E. Pliński. «Terahertz photomixer». In: *Bulletin of the Polish Academy of Sciences: Technical Sciences* (2010), pp. 463–470 (cit. on p. 6).
- [14] U. Keller. «Recent developments in compact ultrafast lasers». In: *nature* 424.6950 (2003), pp. 831–838 (cit. on p. 6).
- [15] F. Wang et al. «Ultrafast response of harmonic modelocked THz lasers». In: *Light: Science & Applications* 9.1 (2020), pp. 1–8 (cit. on p. 6).
- [16] B. Ryvkin et al. «Asymmetric-waveguide laser diode for high-power optical pulse generation by gain switching». In: *Journal of Lightwave Technology* 27.12 (2009), pp. 2125–2131 (cit. on p. 6).
- [17] S. Koenig et al. «Wireless sub-THz communication system with high data rate». In: *Nature photonics* 7.12 (2013), pp. 977–981 (cit. on p. 7).
- [18] M. Rossetti et al. «Time-domain travelling-wave model for quantum dot passively mode-locked lasers». In: *IEEE Journal of Quantum Electronics* 47.2 (2011), pp. 139–150 (cit. on pp. 7, 47, 76, 91, 113).
- [19] M. Rossetti et al. «Modeling passive mode-locking in quantum dot lasers: A comparison between a finite-difference traveling-wave model and a delayed differential equation approach». In: *IEEE Journal of Quantum Electronics* 47.5 (2011), pp. 569–576 (cit. on pp. 8, 77).
- [20] I. N. Stranski. «Beitrag zur Theorie der orientierten Ausscheidung von Ionenkristallen aufeinander und zur Frage der Bildung von Grimmschen Mischkristallen». In: *Zeitschrift für Physikalische Chemie* 1931A.Supplement (1931), pp. 230–238. DOI: doi : 10 . 1515 / zpch - 1931 - s124. URL: <https://doi.org/10.1515/zpch-1931-s124> (cit. on p. 10).
- [21] A. Baskaran et al. «Mechanisms of Stranski-Krastanov growth». In: *Journal of Applied Physics* 111.4 (2012), p. 044321 (cit. on p. 10).
- [22] R. K. Willardson et al. *Self-Assembled InGaAs/GaAs Quantum Dots*. Academic Press, 1999 (cit. on pp. 10, 24).
- [23] J. Chen et al. «Tuning InAs/GaAs quantum dot properties under Stranski-Krastanov growth mode for 1.3 μm applications». In: *Journal of applied physics* 91.10 (2002), pp. 6710–6716 (cit. on p. 10).
- [24] M. Krakowski et al. «High power, broad spectral width, 1300nm quantum-dot superluminescent diodes». In: *2008 IEEE 21st International Semiconductor Laser Conference*. IEEE. 2008, pp. 23–24 (cit. on p. 11).

- [25] M. Burt. «The justification for applying the effective-mass approximation to microstructures». In: *Journal of Physics: Condensed Matter* 4.32 (1992), p. 6651 (cit. on p. 13).
- [26] A. Wojs et al. «Electronic structure and magneto-optics of self-assembled quantum dots». In: *Physical Review B* 54.8 (1996), p. 5604 (cit. on p. 14).
- [27] E. U. Rafailov et al. *Ultrafast lasers based on quantum dot structures: physics and devices*. John Wiley & Sons, 2011 (cit. on pp. 18, 31, 50, 52).
- [28] H. Haug et al. *Quantum theory of the optical and electronic properties of semiconductors*. World Scientific Publishing Company, 2009 (cit. on pp. 19, 21, 24, 26, 83).
- [29] Wikipedia. *Bra–ket notation* — *Wikipedia, The Free Encyclopedia*. <http://en.wikipedia.org/w/index.php?title=Bra%E2%80%93ket%20notation&oldid=1101070655>. [Online; accessed 12-August-2022]. 2022 (cit. on p. 20).
- [30] S. Cortez et al. «Polarization of the interband optical dipole in InAs/GaAs self-organized quantum dots». In: *Physical Review B* 63.23 (2001), p. 233306 (cit. on pp. 23, 68).
- [31] K. L. Silverman et al. «Direct measurement of polarization resolved transition dipole moment in InGaAs/GaAs quantum dots». In: *Applied Physics Letters* 82.25 (2003), pp. 4552–4554 (cit. on pp. 23, 68).
- [32] P. Blood et al. «Localized Auger recombination in quantum-dot lasers». In: *IEEE journal of quantum electronics* 43.12 (2007), pp. 1140–1146 (cit. on p. 27).
- [33] T. W. Berg et al. «Ultrafast gain recovery and modulation limitations in self-assembled quantum-dot devices». In: *IEEE Photonics Technology Letters* 13.6 (2001), pp. 541–543 (cit. on p. 29).
- [34] W. W. Chow et al. «Theory of semiconductor quantum-dot laser dynamics». In: *IEEE journal of quantum electronics* 41.4 (2005), pp. 495–505 (cit. on p. 29).
- [35] C. Tong et al. «Rate Equations for 1.3-um Dots-Under-a-Well and Dots-in-a-Well Self-Assembled InAs–GaAs Quantum-Dot Lasers». In: *IEEE journal of quantum electronics* 42.11 (2006), pp. 1175–1183 (cit. on p. 31).
- [36] M. Sugawara et al. «Theory of optical signal amplification and processing by quantum-dot semiconductor optical amplifiers». In: *Physical Review B* 69.23 (2004), p. 235332 (cit. on p. 34).
- [37] J.-H. Ser et al. «Direct observation of strong quantum-confined stark effect in vertically-stacked quantum dots at room temperature». In: *Japanese Journal of Applied Physics* 39.6A (2000), p. L518 (cit. on p. 35).

- [38] W. Sheng et al. «Anomalous quantum-confined stark effects in stacked InAs/GaAs self-assembled quantum dots». In: *Physical review letters* 88.16 (2002), p. 167401 (cit. on p. 35).
- [39] P. Fry et al. «Inverted electron-hole alignment in InAs-GaAs self-assembled quantum dots». In: *Physical review letters* 84.4 (2000), p. 733 (cit. on p. 36).
- [40] D. Malins et al. «Ultrafast electroabsorption dynamics in an InAs quantum dot saturable absorber at 1.3 μ m». In: *Applied Physics Letters* 89.17 (2006), p. 171111 (cit. on pp. 36, 44).
- [41] A. Stiff-Roberts et al. «Contribution of field-assisted tunneling emission to dark current in InAs-GaAs quantum dot infrared photodetectors». In: *IEEE photonics technology letters* 16.3 (2004), pp. 867–869 (cit. on p. 36).
- [42] S. Franchi et al. «Quantum dot nanostructures and molecular beam epitaxy». In: *Progress in Crystal Growth and Characterization of Materials* 47.2-3 (2003), pp. 166–195 (cit. on p. 38).
- [43] T. Brabec et al. «Kerr lens mode locking». In: *Optics Letters* 17.18 (1992), pp. 1292–1294 (cit. on p. 39).
- [44] L. A. Coldren et al. *Diode lasers and photonic integrated circuits*. John Wiley & Sons, 2012 (cit. on pp. 39, 75).
- [45] J. Renaudier et al. «Phase correlation and linewidth reduction of 40 GHz self-pulsation in distributed Bragg reflector semiconductor lasers». In: *IEEE Journal of Quantum Electronics* 43.2 (2007), pp. 147–156 (cit. on pp. 41, 42).
- [46] W. Seitz et al. «All-optical active mode locking with a nonlinear semiconductor modulator». In: *Optics Letters* 27.24 (2002), pp. 2209–2211 (cit. on p. 43).
- [47] D. Kuizenga et al. «FM and AM mode locking of the homogeneous laser-Part I: Theory». In: *IEEE Journal of Quantum Electronics* 6.11 (1970), pp. 694–708 (cit. on p. 43).
- [48] U. Keller et al. *Ultrafast Laser Physics*. <https://ulp.ethz.ch/education/lectures/ultrafast-laser-physics/lecture-notes.html>. [Online; accessed 17 May 2022] (cit. on pp. 43, 44).
- [49] J. Kim et al. «All-fiber acousto-optic modulator based on a cladding-etched optical fiber for active mode-locking». In: *Photonics Research* 5.5 (2017), pp. 391–395 (cit. on p. 43).
- [50] M. Stock et al. «Synchronous mode locking using pump-induced phase modulation». In: *Optics Letters* 18.18 (1993), pp. 1529–1531 (cit. on p. 44).

-
- [51] R. Paschotta et al. «Passive mode locking with slow saturable absorbers». In: *Applied Physics B* 73.7 (2001), pp. 653–662 (cit. on p. 44).
- [52] E. Avrutin et al. «Monolithic and multi-gigahertz mode-locked semiconductor lasers: constructions, experiments, models and applications». In: *IEEE Proceedings-Optoelectronics* 147.4 (2000), pp. 251–278 (cit. on pp. 45, 46).
- [53] J. Hohimer et al. «Passive mode locking of monolithic semiconductor ring lasers at 86 GHz». In: *Applied physics letters* 63.12 (1993), pp. 1598–1600 (cit. on p. 45).
- [54] R. Arkhipov et al. «Hybrid mode locking in semiconductor lasers: simulations, analysis, and experiments». In: *IEEE Journal of Selected Topics in Quantum Electronics* 19.4 (2012), pp. 1100208–1100208 (cit. on p. 45).
- [55] R. Kaiser et al. «Monolithic 40-GHz mode-locked MQW DBR lasers for high-speed optical communication systems». In: *IEEE Journal of Selected Topics in Quantum Electronics* 13.1 (2007), pp. 125–135 (cit. on p. 45).
- [56] D. Bimberg et al. «High speed nanophotonic devices based on quantum dots». In: *physica status solidi (a)* 203.14 (2006), pp. 3523–3532 (cit. on pp. 45, 57, 58, 65).
- [57] F. Krausz et al. «Self-starting passive mode locking». In: *Optics Letters* 16.4 (1991), pp. 235–237 (cit. on p. 45).
- [58] P. Bardella et al. «Self-generation of optical frequency comb in single section quantum dot Fabry-Perot lasers: a theoretical study». In: *Optics Express* 25.21 (2017), pp. 26234–26252 (cit. on p. 45).
- [59] K. Brown et al. «Control over spectral content via differential pumping of a monolithic passively mode-locked quantum dot laser». In: *Enabling Photonics Technologies for Defense, Security, and Aerospace Applications III*. Vol. 6572. SPIE. 2007, pp. 71–79 (cit. on p. 45).
- [60] Y.-C. Xin et al. «Reconfigurable quantum dot monolithic multi-section passive mode-locked lasers». In: *Optics Express* 15.12 (2007), pp. 7623–7633 (cit. on p. 45).
- [61] J. Van der Ziel. «Active mode locking of double heterostructure lasers in an external cavity». In: *Journal of Applied Physics* 52.7 (1981), pp. 4435–4446 (cit. on p. 46).
- [62] Y. Silberberg et al. «Passive mode locking of a semiconductor diode laser». In: *Optics Letters* 9.11 (1984), pp. 507–509 (cit. on p. 46).
- [63] D. J. Derickson et al. «Short pulse generation using multisegment mode-locked semiconductor lasers». In: *IEEE Journal of Quantum Electronics* 28.10 (1992), pp. 2186–2202 (cit. on p. 46).

- [64] P. Vasil'Ev et al. «Generation of bandwidth-limited 2 ps pulses with 100 GHz repetition rate from multisegmented injection laser». In: *Electronics Letters* 25 (1989), p. 1049 (cit. on p. 46).
- [65] C. Henry. «Theory of the linewidth of semiconductor lasers». In: *IEEE Journal of Quantum Electronics* 18.2 (1982), pp. 259–264 (cit. on p. 50).
- [66] E. U. Rafailov et al. «Mode-locked quantum-dot lasers». In: *Nature photonics* 1.7 (2007), pp. 395–401 (cit. on p. 51).
- [67] E. A. Viktorov et al. «Recovery time scales in a reversed-biased quantum dot absorber». In: *Applied Physics Letters* 94.26 (2009), p. 263502 (cit. on p. 52).
- [68] M. A. Cataluna et al. «Dual-wavelength mode-locked quantum-dot laser, via ground and excited state transitions: experimental and theoretical investigation». In: *Optics Express* 18.12 (2010), pp. 12832–12838 (cit. on p. 52).
- [69] S. Breuer et al. «Reverse-emission-state-transition mode locking of a two-section InAs/InGaAs quantum dot laser». In: *Applied Physics Letters* 97.7 (2010), p. 071118 (cit. on p. 52).
- [70] P. Borri et al. «Spectral hole-burning and carrier-heating dynamics in InGaAs quantum-dot amplifiers». In: *IEEE Journal of selected topics in Quantum electronics* 6.3 (2000), pp. 544–551 (cit. on p. 52).
- [71] P. Borri et al. «Ultrafast carrier dynamics in InGaAs quantum dot materials and devices». In: *Journal of Optics A: Pure and Applied Optics* 8.4 (2006), S33 (cit. on p. 52).
- [72] T. R. Nielsen et al. «Many-body theory of carrier capture and relaxation in semiconductor quantum-dot lasers». In: *Physical Review B* 69.23 (2004), p. 235314 (cit. on p. 53).
- [73] M. Thompson et al. «Subpicosecond high-power mode locking using flared waveguide monolithic quantum-dot lasers». In: *Applied Physics Letters* 88.13 (2006), p. 133119 (cit. on p. 53).
- [74] X. Huang et al. «Passive mode-locking in 1.3 μm two-section InAs quantum dot lasers». In: *Applied Physics Letters* 78.19 (2001), pp. 2825–2827 (cit. on pp. 53, 54, 65).
- [75] M. Thompson et al. «10 GHz hybrid modelocking of monolithic InGaAs quantum dot lasers». In: *Electronics Letters* 39.15 (2003), p. 1 (cit. on pp. 54, 55, 65).
- [76] M. Thompson et al. «Transform-limited optical pulses from 18 GHz monolithic modelocked quantum dot lasers operating at $\sim 1.3 \mu\text{m}$ ». In: *Electronics Letters* 40.5 (2004), p. 1 (cit. on pp. 55, 56, 65).

- [77] E. U. Rafailov et al. «High-power picosecond and femtosecond pulse generation from a two-section mode-locked quantum-dot laser». In: *Applied Physics Letters* 87.8 (2005), p. 081107 (cit. on pp. 56, 57, 65).
- [78] L. Zhang et al. «InAs Quantum dot DFB lasers on GaAs for uncooled 1310nm fiber communication». In: *Optical Fiber Communication Conference*. Optica Publishing Group. 2003, FG2 (cit. on pp. 56, 57).
- [79] L. Zhang et al. «Low timing jitter, 5 GHz optical pulses from monolithic two-section passively mode-locked 1250/1310 nm Quantum Dot lasers for high speed optical interconnects». In: *Optical Fiber Communication Conference*. Optica Publishing Group. 2005, OWM4 (cit. on pp. 56, 57, 65).
- [80] A. Gubenko et al. «High-power monolithic passively modelocked quantum-dot laser». In: *Electronics Letters* 41.20 (2005), p. 1 (cit. on pp. 56, 57, 65).
- [81] M. Thompson et al. «Colliding-pulse modelocked quantum dot lasers». In: *Electronics Letters* 41.5 (2005), p. 1 (cit. on pp. 58, 65).
- [82] M. Kuntz et al. «High-speed mode-locked quantum-dot lasers and optical amplifiers». In: *Proceedings of the IEEE* 95.9 (2007), pp. 1767–1778 (cit. on pp. 59, 65).
- [83] J. Liu et al. «Dual-wavelength 92.5 GHz self-mode-locked InP-based quantum dot laser». In: *Optics Letters* 33.15 (2008), pp. 1702–1704 (cit. on pp. 59, 60, 65).
- [84] Z. Lu et al. «312-fs pulse generation from a passive C-band InAs/InP quantum dot mode-locked laser». In: *Optics Express* 16.14 (2008), pp. 10835–10840 (cit. on pp. 60, 65).
- [85] Z. Lu et al. «An L-band monolithic InAs/InP quantum dot mode-locked laser with femtosecond pulses». In: *Optics Express* 17.16 (2009), pp. 13609–13614 (cit. on pp. 60, 65).
- [86] M. G. Thompson et al. «InGaAs quantum-dot mode-locked laser diodes». In: *IEEE Journal of Selected Topics in Quantum Electronics* 15.3 (2009), pp. 661–672 (cit. on pp. 60, 61, 65, 111).
- [87] C.-Y. Lin et al. «Compact optical generation of microwave signals using a monolithic quantum dot passively mode-locked laser». In: *IEEE Photonics Journal* 1.4 (2009), pp. 236–244 (cit. on pp. 60, 62, 65, 96).
- [88] E. A. Avrutin et al. «Dynamics and spectra of monolithic mode-locked laser diodes under external optical feedback». In: *IEEE journal of quantum electronics* 45.11 (2009), pp. 1456–1464 (cit. on p. 62).

- [89] C.-Y. Lin et al. «RF linewidth reduction in a quantum dot passively mode-locked laser subject to external optical feedback». In: *Applied Physics Letters* 96.5 (2010), p. 051118 (cit. on pp. 62, 65).
- [90] Z. Lu et al. «High performance InAs/InP quantum dot 34.462-GHz C-band coherent comb laser module». In: *Optics express* 26.2 (2018), pp. 2160–2167 (cit. on pp. 63, 65).
- [91] Z. Lu et al. «Ultra-narrow linewidth quantum dot coherent comb lasers with self-injection feedback locking». In: *Optics express* 26.9 (2018), pp. 11909–11914 (cit. on p. 63).
- [92] S. Liu et al. «490 fs pulse generation from passively mode-locked single section quantum dot laser directly grown on on-axis GaP/Si». In: *Electronics Letters* 54.7 (2018), pp. 432–433 (cit. on pp. 63–65).
- [93] S. Liu et al. «Monolithic 9 GHz passively mode locked quantum dot lasers directly grown on on-axis (001) Si». In: *Applied Physics Letters* 113.4 (2018), p. 041108 (cit. on pp. 64, 65).
- [94] S. Liu et al. «High-channel-count 20 GHz passively mode-locked quantum dot laser directly grown on Si with 4.1 Tbit/s transmission capacity». In: *Optica* 6.2 (2019), pp. 128–134 (cit. on pp. 64, 65).
- [95] Z.-H. Wang et al. «InAs/GaAs quantum dot single-section mode-locked lasers on Si (001) with optical self-injection feedback». In: *Optics Express* 29.2 (2021), pp. 674–683 (cit. on pp. 64, 65).
- [96] S. Pan et al. «Quantum dot mode-locked frequency comb with ultra-stable 25.5 GHz spacing between 20° C and 120° C». In: *Photonics Research* 8.12 (2020), pp. 1937–1942 (cit. on pp. 64, 65).
- [97] B. Dong et al. «1.3- μ m passively mode-locked quantum dot lasers epitaxially grown on silicon: gain properties and optical feedback stabilization». In: *Journal of Physics: Photonics* 2.4 (2020), p. 045006 (cit. on pp. 64, 65, 111, 112).
- [98] M. Dumont et al. «High-efficiency quantum dot lasers as comb sources for DWDM applications». In: *Applied Sciences* 12.4 (2022), p. 1836 (cit. on pp. 64, 65).
- [99] M. Heydari et al. «Fully Integrated, 80 GHz Bandwidth, 1.3 μ m InAs/InGaAs CW-PW Quantum Dot Passively Colliding-Pulse Mode-Locked (CPM) Lasers for IR Sensing Application». In: *IEEE Sensors Journal* 22.7 (2022), pp. 6528–6535 (cit. on pp. 64, 65).
- [100] K. Akahane et al. «High-frequency short-pulse generation with a highly stacked InAs quantum dot mode-locked laser diode». In: *Japanese Journal of Applied Physics* 60.SB (2021), SBBH02 (cit. on pp. 64, 65).

- [101] N. Marcuvitz. *Waveguide handbook*. 21. Iet, 1951 (cit. on p. 67).
- [102] J. Piprek et al. *Optoelectronic devices*. Springer, 2005 (cit. on p. 73).
- [103] M. Gioannini et al. «Numerical analysis of the frequency chirp in quantum-dot semiconductor lasers». In: *IEEE Journal of Quantum Electronics* 43.10 (2007), pp. 941–949 (cit. on p. 74).
- [104] G. New. «Pulse evolution in mode-locked quasi-continuous lasers». In: *IEEE Journal of Quantum Electronics* 10.2 (1974), pp. 115–124 (cit. on pp. 76, 77).
- [105] H. Haus. «Theory of mode locking with a slow saturable absorber». In: *IEEE Journal of Quantum Electronics* 11.9 (1975), pp. 736–746 (cit. on pp. 76, 77, 93, 114).
- [106] J. Leegwater. «Theory of mode-locked semiconductor lasers». In: *IEEE journal of quantum electronics* 32.10 (1996), pp. 1782–1790 (cit. on p. 76).
- [107] J. Dubbeldam et al. «Theory of mode-locked semiconductor lasers with finite absorber relaxation times». In: *Applied physics letters* 70.15 (1997), pp. 1938–1940 (cit. on p. 76).
- [108] E. A. Avrutin et al. «Dynamic modal analysis of monolithic mode-locked semiconductor lasers». In: *IEEE Journal of selected topics in quantum electronics* 9.3 (2003), pp. 844–856 (cit. on p. 76).
- [109] A. G. Vladimirov et al. «Model for passive mode locking in semiconductor lasers». In: *Physical Review A* 72.3 (2005), p. 033808 (cit. on pp. 77, 78, 82, 110).
- [110] E. A. Viktorov et al. «Model for mode locking in quantum dot lasers». In: *Applied physics letters* 88.20 (2006), p. 201102 (cit. on pp. 77, 78, 110).
- [111] M. A. Cataluna et al. «Temperature dependence of pulse duration in a mode-locked quantum-dot laser». In: *Applied Physics Letters* 90.10 (2007), p. 101102 (cit. on p. 77).
- [112] E. A. Viktorov et al. «Stability of the mode-locked regime in quantum dot lasers». In: *Applied physics letters* 91.23 (2007), p. 231116 (cit. on p. 77).
- [113] A. G. Vladimirov et al. «Dynamical regimes in a monolithic passively mode-locked quantum dot laser». In: *JOSA B* 27.10 (2010), pp. 2102–2109 (cit. on p. 77).
- [114] U. Bandelow et al. «40 GHz mode-locked semiconductor lasers: theory, simulations and experiment». In: *Optical and Quantum Electronics* 38.4 (2006), pp. 495–512 (cit. on p. 77).

- [115] Wikipedia. *Cauchy principal value* — *Wikipedia, The Free Encyclopedia*. https://en.wikipedia.org/wiki/Cauchy_principal_value. [Online; accessed 19-August-2022]. 2022 (cit. on p. 83).
- [116] J.-C. Diels et al. *Ultrashort laser pulse phenomena*. Elsevier, 2006 (cit. on p. 84).
- [117] H. Schmeckeber et al. «Complete pulse characterization of quantum-dot mode-locked lasers suitable for optical communication up to 160 Gbit/s». In: *Optics express* 18.4 (2010), pp. 3415–3425 (cit. on p. 84).
- [118] R. Phelan et al. «Mid-Infrared InP-Based Discrete Mode Laser Diodes». In: *Optical Fiber Applications* (2019), p. 15 (cit. on pp. 85, 86).
- [119] G. Giannuzzi et al. «Semiconductor racetrack resonator coupled to an S-bent waveguide: Influence of the coupling coefficients on the unidirectional operation». In: *IET Optoelectronics* 15.3 (2021), pp. 131–138 (cit. on pp. 86, 87).
- [120] D. Kazakov et al. «Defect-engineered ring laser harmonic frequency combs». In: *Optica* 8.10 (2021), pp. 1277–1280 (cit. on p. 87).
- [121] S. Meinecke et al. «Ultra-short pulse generation in a three section tapered passively mode-locked quantum-dot semiconductor laser». In: *Scientific Reports* 9.1 (2019), pp. 1–14 (cit. on p. 111).